André Beerlink

Black lipid membranes studied by x-ray phase contrast imaging

André Beerlink

Black lipid membranes studied by x-ray phase contrast imaging

André Beerlink

Black lipid membranes studied by x-ray phase contrast imaging

Bibliographische Information der Deutschen Nationalbibliothek

Die Deutsche Nationalbibliothek verzeichnet diese Publikation in der Deutschen Nationalbibliographie; detaillierte bibliographische Daten sind im Internet über <http://dnb.ddb.de> abrufbar.

Address of the Author
Dr. André Beerlink
www: http://petra3.desy.de/
Email: andre.beerlink@desy.de

Layout: André Beerlink
Cover: Jutta Pabst
Cover image: André Beerlink

Preface of the series editor

The Göttingen series in X-ray physics is intended as a collection of research monographs in x-ray science, carried out at the Institute for X-ray Physics at the Georg-August-Universität in Göttingen, and in the framework of its related research networks and collaborations.

It covers topics ranging from X-ray microscopy, nano-focusing, wave propagation, image reconstruction, tomography, short X-ray pulses to applications of nanoscale x-ray imaging and biomolecular structure analysis.

In most but not all cases, the contributions are based on Ph.D. dissertations. The individual monographs should be enhanced by putting them in the context of related work, often based on a common long term research strategy, and funded by the same research networks. We hope that the series will also help to enhance the visibility of the research carried out here and help others in the field to advance similar projects.

Prof. Dr. Tim Salditt, Editor
Göttingen February 2011

Meinen Eltern

"Beholding life in a soap bubble,
Self-assembly is the key.
To make a BLM invitro,
Shows the biomembrane's living complexity."
(from [TOL00])

"A soap bubble is the most beautiful thing,
and the most exquisite in nature...
I wonder how much it would take to buy a soap bubble,
if there was only one in the world?"
(Mark Twain, "The Innocents Abroad", 1869)

Contents

Introduction

"All life today is cellular, and cells are defined by membranes that separate the cytoplasm from the outside world. When life began, at some point it became compartmented in the form of cells. ..."
This citation from [Dea08] nicely points out the importance of cell membranes in nature and the role they played in the formation of the first living organisms .

Pro- and eucaryotic cells both have an important thing in common. A cell membrane separates them from the extracellular environment. Especially in eucaryotes a membrane also partitions each single organelle inside the cell from the cytosol [Pre88]. Thus, membranes fulfill a great variety of functional tasks, such as protection, regulation, compartmentalization, nutrition supply, ion transport, and signal transmission. Membranes ensure the cell's survival and hence ensure the survival of the whole organism [Sac95, Alb94].
One of the major building blocks of plasma membranes are lipids, e.g. phospholipids, sphingolipids, and glycolipids in various amounts. In addition membranes can be modified by molecules such as cholesterol, peptides, or proteins. These compounds can make up 50% of the membrane composition depending on the functionality of the membrane inside the organism [Str03].
In order to analyze such a complex system and to develop methods for the investigation of designated properties a simplified model has to be generated. As a consequence the variety of components will be reduced to build up a model membrane system mimicking the very basic native conditions, e.g. the pure lipid matrix. In this work, three different types of reconstituted membranes are used. Each of them shows both benefits and drawbacks and enables the investigation of different lipid membrane properties.
We have recently adapted the well known setup of Black Lipid Membranes (BLMs) from electrophysiological to *in vitro* structural x-ray studies [BWZ$^+$08]. These BLMs are single, freely suspended lipid bilayers, which are spanned in between two separate fluid compartments and are an established model system in membrane biophysics [MRTW62b, TOL00]. They allow for studies of functional transport across the bilayer at controlled conditions, such as protein concentration, ionic strength, pH, and electrical field strength, e.g. by recording single channel conductance with a patch clamp amplifier [Hil84, NS76]. Particular advantages of BLMs over model systems, like uni- or multi-lamellar solid supported membranes or giant unilamellar vesicles (GUVs), derive from the fact that the membranes are accessible from both sides. Furthermore they can be manipulated easily, and allow for the exposure to fluid compartments of asymmetric ionic strength and the application of electric fields. Using specific preparation techniques, the bilayer itself can be built up with asymmetric lipid

monolayers, similar to biological membranes, which are mostly asymmetric in composition.

The system of BLMs is until today a common model membrane system, which offers a native environment and at the same can be easily prepared and manipulated. The underlying core motivation for the use of BLMs in this thesis is to investigate the structure of biomimetic membranes in various environmental conditions. This study will allow us to close the gap between two approaches, which are performed to investigate membrane properties. On the one hand, x-ray reflectometry experiments offer sub-molecular resolution, but still have to be carried out under unphysiological conditions, i.e. in the presence of a solid support, which borders the membrane on one side. On the other hand, electrophysiological experiments give rise to electrochemical properties of membranes with high precision but poor resolution of structural changes, since they are mostly carried out by using visible light microscopy. A combination of these two techniques is of great importance, due to the fact that native membranes are always accompanied by electric fields, and it is known that these fields have a great influence on the structural and functional, as well as electrochemical properties of the membrane.

In the following thesis I will present the development of an experimental setup as well as a theoretical model, which allows us to simultaneous investigate electrophysiological and structural changes and their dependencies in model membrane systems. Recent results from studies during this work have been published [BWZ$^+$08, BMTS09].

In the *first chapter* a summary of the state of art of freestanding Black Lipid Membrane research will be presented. The chapter mainly deals with the discovery and development of BLMs as an experimental model system and the investigation of structural and electrophysiological properties. *Chapter two* is dedicated to the description of Black Lipid Membrane thinning, the driving forces of this process, and its interfacial properties. *Chapter three* will introduce the reader to the basics of BLM electrostatics and current techniques used to investigate the respective properties. The influence of electric fields on the membrane structure will be discussed, and studies on **s**olid **s**upported **m**embranes (SSMs) to investigate this effect are presented. In *chapter four* we will give a detailed description of the preparation of the three different membrane systems which are used in this work. A novel type of BLMs, the microfluidic BLMs (mfBLMs), and its benefits in x-ray imaging techniques will be discussed. In the *fifth chapter* we develop a simplified, but extendable, model for an experimental scheme, which can be considered a hybrid of propagation based phase contrast imaging and Fresnel diffraction. Related synchrotron studies, details of experimental setups and the raw image data processing are presented in *chapter six*. In *chapter seven*, we use this novel technique, which is described

in the previous two chapters, to quantitatively monitor the structure and thinning of BLMs and we discuss the current limits in view of resolution and contrast. Finally, we demonstrate how these limitations can be overcome by using a focused x-ray beam to visualize ultrathin Black Lipid Membranes of 5 nm thickness. Chapter eight summarizes the results, which are achieved in the frame of this thesis, and presents an outlook on future applications and experimental developments.

1 State of the art: structure of lipid membrane model systems

1.1 The lipid bilayer concept

Within the scope of this thesis the structural and dynamical properties of Black Lipid Membranes (BLMs) are investigated. In this section a short introduction to the development of this very special model membrane system will be given [TOL00, TOL03].

In the seventeenth century, Newton and Boys [New74, Boy59] investigated the structure and colors of black soap films (see figure 1.1(a)). Inspired by these studies, in the early 1960's, Müller, Rudin, Tien and Wescott presented a way to prepare freestanding lipid bilayers, which are bordered by two aqueous reservoirs [MRTW62b, MRTW62a] (see figure 1.1(a)). According to previous works in history they called their membranes "Black Lipid Membranes" (BLMs).
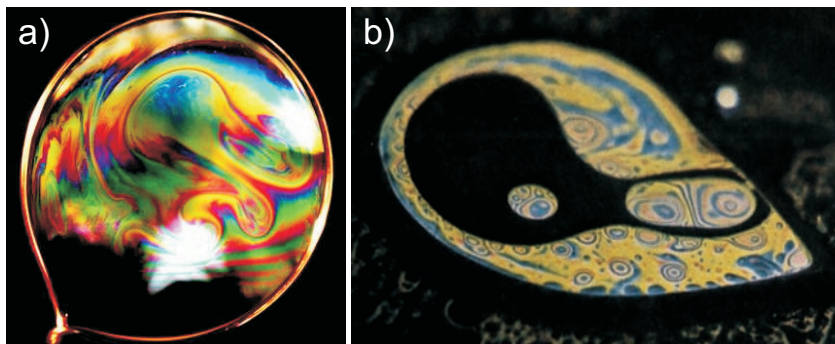
Figure 1.1: *a) First investigations of BLMs were inspired by soap film experiments, which are in perfect analogy to each other [Int10]. b) Image of a Black Lipid Membrane (BLM) showing Newton interference fringes in the course of illumination with white light. From these colors the membrane thickness can be determined. When the membrane spontaneously thins, i.e. it transforms from a bulk to a bimolecular film, black spots of destructive interference appear. They grow until only a bright, thick region of assembled lipid-solvent solution, namely the Plateau-Gibbs border (PGB), at the rim of the film is left [MRTW62b].*

In 1890, it was Pfeffer [Pfe90] who observed the enclosure of the cell by a plasma membrane. His results were refined by Gorter and Grendel in 1925 [GG25], who were the first to describe the cell membrane bilayer characteristics. Sub-

sequently, Danielli and Davson, in 1935 [DH35], postulated that the cell membrane consists of two lipid monolayers facing each other with the hydrocarbon tails, while the dipolar headgroups pointing towards the aqueous phase. At this time the model of the orthogonal structural arrangement of a lipid bilayer was fully developed.

The discussion about the lateral organization of lipid membranes was continued and the "lipid bilayer concept" [TOL00] rapidly developed. It ended up in today's view of the cell membrane as a "fluid mosaic model"; a model which was put forward by Singer and Nicholson [SN72] in 1972.

It was mentioned in the introduction that the presence of electric fields is of great importance for the functionality of transmembrane proteins and the interactions between them and the surrounding lipid matrix. The BLM was the first experimental model to enable the investigation of electrophysiological properties of ion channel proteins in a biological environment, i.e. the recording of ion fluxes across a bilayer in the absence of a supporting substrate. Therefore BLMs have been widely used as a powerful tool in biophysical research, i.e. especially electrophysiology. Despite this fact, the preparation, the final formation process and the sub-molecular structure of these membrane systems are still poorly understood and remain to be discussed and further explored extensively [Whi86].

1.2   Structural investigations of Black Lipid Membranes (BLMs)

In the past many methods were developed to investigate the thickness of freestanding bilayer membranes. Some of them originate from the studies on soap films in air (see figure 1.1(b)) and others have been recently introduced. In this section these methods will be briefly described and their limitations and applications will be discussed. Details of the equations for thickness determination and the experimental setups can be found in the numerous references.

1.2.1   Visible light studies

The first high resolution experiments to investigate the structure of bimolecular membranes made from surface active, amphiphilic molecules were carried out by reflecting monochromatic light onto the film surface. The reflectivity under specular conditions, i.e. at a position where the angle of refraction equals the angle of incidence, is defined as the ratio of impinging intensity I_0 and reflected intensity I_r light in the plane of incidence. The electric field vector is considered to be perpendicular to the plane of incidence. At an angle θ with respect to the perpendicular of the surface, under which the light is diffracted inside the

membrane, the dependence of the reflectivity on the film thickness d is given by [BW99, Tie74, Iva88]:

$$\frac{I_0}{I_r} = 4\,r\,\sin^2\left(\frac{2\,\pi\,n\,\cos(\theta)}{\lambda}\,d\right) \tag{1.1}$$

with the wavelength of the light λ and the reflection coefficient of the membrane-water interface r. The latter one is related to the refractive index n of the film. Before BLMs were introduced, different groups studied soap films in air [Ove60, MSF59, MJ66, Vri64] by using this technique. The results could experimentally confirm the thinning dynamics and forces in bimolecular films based on the Derjaguin, Landau, Verwey, and Overbeek (DLVO) theory (see section 2.2). First experiments on thickness determination of BLMs were performed by Tien [TCD66, TD66, Tie66, Tie67a], Huang [HWT64, HT65, TH66b], Cherry [CC67, CC69b, CC69a] and others [Sim70, SC71, DFH82, MK88]. The resolution of this technique is limited by the underlying layer model, which is used to calculate the reflectivity of the film (see figure 1.2).
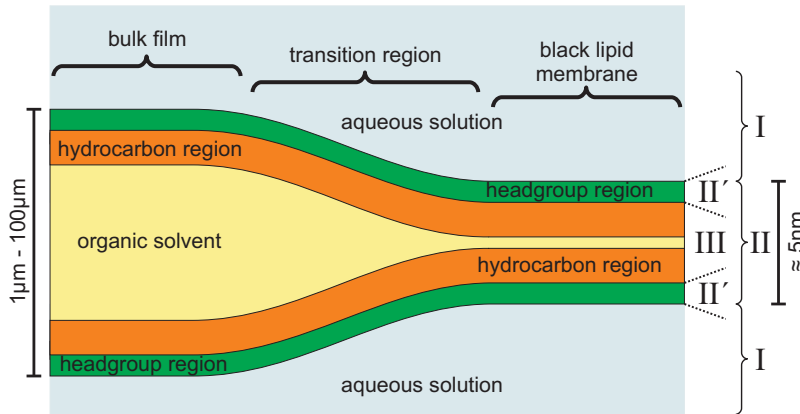
Figure 1.2: *Schematic representation of the layer structures in a bulk film, consisting of two monolayers separated by a layer of organic solvent, and the BLM, which is considered as a single bilayer. Two types of layer models of the BLM, which is bordered by an aqueous medium* **I**, *are depicted. One is composed of a single layer* **II**, *while the other one consists of three layers and considers phospholipid headgroups* **II'** *and hydrocarbon tails* **III** *as separated layers.*

The first theories were based on a single layer model (II) in an aqueous medium (I) [TD66]. Finally a three layer model (I|II'|III|II'|I) [Tie67b, SC71, MK88] (see

figure 1.2), which considers phospholipid headgroups and hydrocarbon tails as separated layers, turned out to agree best with the experimental observations. The reflected light technique relies on the exact determination of the refractive index n by a Brewster angle measurement [TD66, HT65], which is performed at a bulk film with $d >100$ nm and $n(d) =$ constant [Tie67b]. This already implies that the determination of essential structure parameters is based on contradictory assumptions, because a three layer model is used to calculate the reflectivity but a single layer model is used to determine the refractive index. Hence, the thickness calculations will always depend on the underlying theoretical model [Tie67b]. This strongly effects the thickness values obtained in the previous literature, ranging from 4.8 nm up to 9 nm, including errors of about 10% to 20% for the same species of surfactant molecules.

In a second approach, the thickness was deduced from the interference fringes of the thinning film (see figure 1.1) when it is illuminated with white light. The resolution of this method is limited to thicknesses where $d >20$ nm-30 nm and, therefore, the information about molecular structures of the bimolecular BLM, which are supposed to be only 5 nm in size, remains inaccessible [Tie74, FFI03].

1.2.2   Electrostatic investigations

Another method for the investigation of the thickness d is based on a simultaneous measurement of the capacitance C_m and the area A of the thinned, bimolecular region of the membrane. A lipid bilayer can be seen as a capacitor. Hence, the static, voltage independent capacitance C_m of the membrane can be defined as [ALS03]:

$$C_m = \varepsilon_0 \varepsilon_m \frac{A}{d} \tag{1.2}$$

with dielectric constant ε_0. The specific dielectric constant $\varepsilon_m \approx 2$ only describes the hydrocarbon core of the bilayer. In chapter 3.2 different methods to measure C_m will be presented. By combining these methods with conventional transmitted light microscopy, the bilayer area A can be precisely determined and d obtained [HHT64, HHT65, vdB65, HT68, AMH70, Whi70, WT73, FFI03]. The regions, where a thin bimolecular membrane has already formed dominate the contributions to C_m, since here the film is about three orders of magnitude thinner compared to domains of trapped solvent [WT73]. A drawback is that the differentiation between the final bilayer regions and very thin areas, where a bilayer has not formed yet, is very inaccurate. Furthermore, there is always an unknown contribution to the capacitance by the lipid-solvent reservoir, called Plateau-Gibbs border (PGB) (see figure 1.1), which surrounds the BLM and is of complex structure [Whi72, Whi86]. Consequently, large errors of about 20% in calculations of d are obtained [WT73] and this technique shows

no benefits with respect to the above described experiments analyzing the ratio of reflected light. A further restriction of this method is that a measurement of the BLM capacitance can only sense the thickness of the hydrocarbon region [HHT65, DFH82]. Due to the dipolar characteristics of the phospholipid headgroups their dielectric constant ε_{HG} is similar to that of water ($\varepsilon_{HG} \approx \varepsilon_{H_2O} \approx 80$). This inhibits the distinction between the two layers.

To account for this limitation, the authors in reference [DFH82] propose a combined study of capacitance and reflectivity measurements. The first technique will allow for the thickness determination of the hydrocarbon layer and the second will gain access to the total BLM thickness. From these two parameters the headgroup layer thickness can be derived in a more accurate fashion.

1.2.3 Electron microscopy

Müller and colleagues [MRTW62b] have performed electron microscopy measurements to study the thickness of their Black Lipid Membranes. They could not reveal the proposed trilaminar structure (headgroup | hydrocarbon | headgroup), but found a thickness of 9 nm for the lipid bilayer [DPR64]. Since they initially used staining agents, such as Osmium, these might have penetrated the hydrocarbon core and made it indistinguishable from the headgroup region. This drawback was solved by avoiding further staining, which finally allowed for the visualization of sub-molecular structures [HDGT67, VE71]. The thickness values in these studies range from 3.7 nm to 11.6 nm, with errors up to 25%. The inaccuracy might originate from the fact that a thinned bilayer was compared to regions of remaining solvent, such as lenses [AH68]. Furthermore this technique is very sensitive to the observation angle, i.e. the orientation of the film with respect to the incident electron beam. A misalignment results in the smearing of the layer features [VE71].

Due to the fact that the fixation of a lipid membrane in a resin with potential addition of heavy-atom staining agents represents a very unnatural environment, there might be a significant influence on the structure of the membrane. Consequently electron microscopy has not become a common technique for investigating lipid membrane properties in native conditions.

1.2.4 X-ray and neutron reflectivity

The last technique, which is presented here, is based on the use of x-rays or neutrons, which are reflected at thin freestanding films. Retrospectively, the order of magnitude of the thickness values which were obtained from visible light reflectivity studies (see previous section) was already in good agreement with the results from x-ray reflectometry. The first x-ray experiments could confirm

the results from DLVO theory and lead to a much more accurate determination of the film thickness [CGOT63, CCG66, PGW90, PGWC93]. Benattar and colleagues have performed extensive studies on the structure, formation and hydration states of freely suspended membranes made from lipid molecules in air [BDOB91, CPN+00, CMP+00, PBN02, TBL+02, SMB+04].

Smith and coworkers were the first to use x-rays to study freestanding, multi-lamellar membrane systems in a humid environment, and could follow phase behavior of the lipids dependent on temperature and relative humidity [SSSC88, SSS+90]. As a consequence of the aforementioned studies a higher precision for the layer-model of the membranes could be derived. In contrast to experiments with visible light, x-ray photons and neutrons offer the opportunity to resolve molecular and sub-molecular structures, since the photons and neutrons have wavelengths which are a factor 10 to 50 times smaller than the thickness of the film. Due to the fact that the x-ray and neutron scattering properties (the electron and nuclear scattering length density contrast between film and surrounding air) are very weak, the reflectivity decreases rapidly for higher angles of incidence. In water these effects are much more pronounced and x-ray and neutron studies were restricted to the studies of thin films freestanding in air. Thus, the resolution of this method, defined by the maximum achievable scattering angle or q_z value, is strongly limited to length scales of 1.8 nm ($\equiv 0.35\,\text{Å}^{-1}$). This is especially the case for neutrons [HHT+84, ET03] where the particle flux is very low and the resolution limit becomes 4 nm ($\equiv 0.16\,\text{Å}^{-1}$). Here the signal-to-noise ratio is even worse compared to experiments using x-ray laboratory sources.

Since the early 1980's there has been a huge number of x-ray and neutron reflectivity studies investigating the structure of lipid mono-, bi- and multilayers at air-oil/-water and solid-liquid interfaces [Dai09, DG09, SRS+86, WSN89, SS90, VMFS00, SLSM02, Sal03, COVS05, MMGK05, NGS06, SBW+09, ARW+09]. These studies take advantage of the fact that the reflectivity is amplified at an interface of two media of different electron or atomic densities. The reflected intensity, which can be easily detected, is modulated by the structure and form factor of the lipid layer, which is assembled at the interface. Subsequently, the electron density profile can be reconstructed with sub-molecular resolution by fitting the recorded signals on the basis of theoretical model assumptions. The benefit of using a (solid) supported membrane system [TM85, TOL00, TBGO98, Sac96] is the high stability [Röm04], the homogeneous structure [Sac96] and the planar geometry, amenable to various surface sensitive techniques, such as described for x-rays and other probes [Joh05, MT06, Oli05, BS06]. However, the main intrinsic drawback is the perturbation the membrane systems by the interaction potential between the membrane and the supporting interface. Furthermore, it has steric effects on membrane collective motions or embedded proteins,

which are often found to denature in the presence of the solid surfaces. Most importantly, the presence of the substrate restricts the range of potential physiological functionalities with respect to transport properties, flux through the bilayer, and asymmetric solutions, i.e. ion concentration gradients across the bilayer. For example, the thin water film between membrane and solid support of about 0.2 nm to 1 nm [CS00] does not provide the sufficiently large ion reservoir with controlled electrophysiological properties, that would be desirable in many experiments. Even for an advanced, supported membrane system, where one of two bilayers "freely" floats above the other one, the presence of the second bilayer and the substrate always influences the observed interactions [CBAFG99, DBAB$^+$05, LFC06, CLF08].

However, despite individual experimental shortcomings, without all these experiments our understanding of lipid bilayer systems would not be where it is today.

1.3   Conclusion

In summary there is a lack of techniques with sufficient resolution that enable the determination of sub-molecular structures in bimolecular, thin films facing their physiologically relevant, aqueous environment. Every technique shows its limitations either from the model, technical or physical point of view. Two years ago we presented a first step towards a major improvement [BWZ$^+$08] when we published the first x-ray reflectivity experiments on black lipid membranes immersed in water. This novel type of investigation is potentially sensitive to the sub-molecular structure and much more independent of model assumptions than techniques based on visible light. However, technical limitations, related to achievable beam sizes, alignment, planarity of the film and photon flux ($> 10^{11} \frac{\text{photons}}{\mu\text{m}^2\,\text{s}}$), as well as an intrinsically weak scattering signal, which is due to the low electron density contrast between membrane and bulk water, remain a great challenge and need to be faced. The recorded reflectivity signal was not sufficient to draw definite conclusions about the electron density distribution inside the BLM. It is hoped that future improvements in synchrotron performance and novel x-ray optics will enable the investigations of reconstituted, freestanding lipid membranes in native conditions by high resolution x-ray reflectivity.

In this thesis we present an alternative technique, which already takes advantage of the aforementioned improvements of x-ray science, but is up to now rather unexplored. This technique uses direct imaging methods - a novel technique based on the interference of partially coherent x-ray photons generated at third generation synchrotron sources. It is called propagation based phase

contrast imaging using hard x-rays and is the essential scope of this work. We show for the first time the application of this imaging technique to freestanding Black Lipid Membranes and demonstrate how this powerful method enables the visualization of such ultrathin films and determination of structural information.

2 Forces and interfacial phenomena in BLMs

Before discussing the main topic of this section, namely the forces acting in black lipid membranes, this chapter introduces essential equations, which will help the reader to understand the description of the transformational processes in bimolecular systems [Tie74, Wil89, Ise92, WH99].

2.1 Interfacial tension and free energy change in BLM formation

By definition the *interfacial tension* γ describes the force f acting on a line of length l in a plane separating two phases, e.g. gas/fluid, fluid/fluid, gas/solid and so forth. Since a bilayer lipid membrane is bordered by a fluid compartment on each side, it has two interfaces and is called a "biface" [Tie74] in the following.
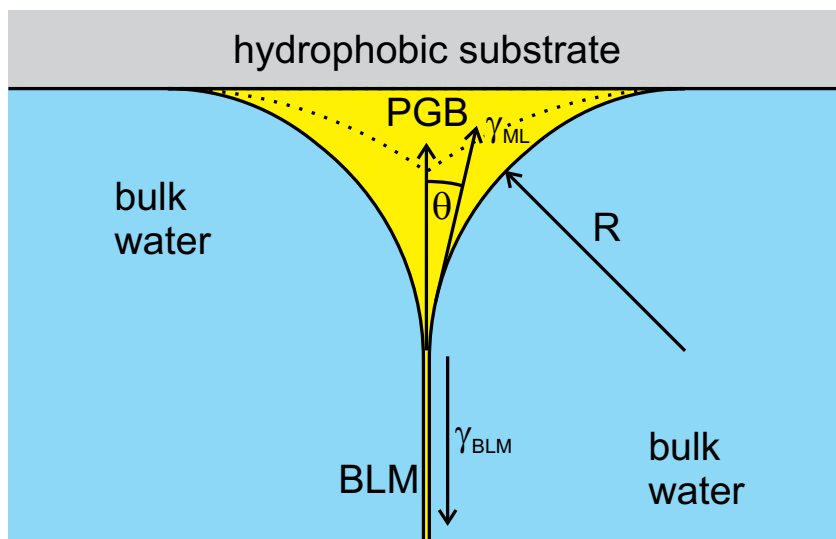
Figure 2.1: *Schematic representation of the Plateau-Gibbs border and the relationship between the interfacial tensions γ_{ML} and bifacial tension γ_{BLM}. The PGB acts as the transition region between the bulk film bordered by two monolayers and the BLM. For the case of a bimolecular BLM $\gamma_{BLM} \neq 2\gamma_{ML}$ (see equation 2.9).*

Each of these interfaces is composed of a lipid monolayer facing an aqueous environment so that they can be described by an interfacial tension γ_{ML} (see figure 2.1). In the case of a bulk membrane, where the monolayers are widely separated by a layer of organic solvent (see figure 1.2), the *bifacial tension* γ_{BLM} is twice the interfacial tension γ_{ML} of the monolayers:

$$\frac{f}{l} = \gamma_{BLM} = 2\gamma_{ML}. \tag{2.1}$$

This assumption does not hold if the monolayers come into contact to form a bimolecular membrane as it is shown in equation 2.8. If the area $A = l \cdot x$ of this film is increased by $\partial A = l \cdot \partial x$ on expansion in one direction we can write the free energy change ΔF of this film as $\Delta F = f \cdot \partial x = (l \cdot \gamma_{BLM}) \cdot \partial x = \gamma_{BLM}\partial A$:

$$\Rightarrow \Delta F = \int_0^A \gamma_{BLM}\partial A. \tag{2.2}$$

If γ_{BLM} remains constant, i.e independent of the area A, we get $\Delta F = \gamma_{BLM}A$. As a consequence of equation 2.2, γ_{BLM} can be understood as the free energy change per unit area. This is the case for films with a high surfactant concentration, e.g. BLMs. Due to the presence the Plateau-Gibbs border, there is always a surplus of lipids and the membrane can expand by a flow of lipid molecules into the bilayer. At the same time this does not imply that the interfacial tension of the BLM vanishes.

The **law of Laplace and Young** describes the topological behavior of an interface in the presence of a pressure gradient Δp acting across it [Wil89, Ise92].

$$\Delta p = \gamma_i \left(\frac{1}{R_1} + \frac{1}{R_2} \right) = \gamma_i \left(c_1 + c_2 \right) \tag{2.3}$$

$c_{1,2} = \frac{1}{R_{1,2}}$ denote the two principal curvatures, which are defined by the radii $R_{1,2}$ of the surface, and γ_i is the tension of the considered interface, i.e. monolayer or BLM. Equation 2.3 shows that interfaces of high curvature, i.e. small R, always separate reservoirs of high and low pressure. The pressure p inside the Plateau-Gibbs border is negative (see figure 2.1) due to the adhesive forces between the trapped organic solvent and the hydrophobic surrounding substrate, which is spanned by the membrane [Whi86]. Consequently it is enclosed by two convex interfaces with negative principle curvatures $c_{1,2} < 0$.

When considering an expanded spherical object with radius R, the total interfacial free energy of its surface is $F_A = \gamma 4\pi R^2$. For a membrane, which we consider as a biface, this becomes

$$F_A = 2(\gamma_{BLM} 4\pi R^2) \Rightarrow dF_A = \gamma_{BLM} 16\pi R\, dR. \tag{2.4}$$

In equilibrium this must balance the work of volume change

$$dF_V = p\,dV = p\,4\pi R^2\,dR \tag{2.5}$$

and we obtain

$$dF_A = \gamma_{BLM}\,16\pi R\,dR = p\,4\pi R^2\,dR = dF_V \tag{2.6}$$

Thus for a BLM it holds [Tie67a, Tie68b, Wil89]:

$$p = \frac{4\gamma_{BLM}}{R} \tag{2.7}$$

Equation 2.7 can be directly derived by inserting $R = R_1 = R_2$ (in case of a sphere) into equation 2.3.

Two different methods have been described to determine the interfacial tension γ_{BLM} of BLMs, which might also be applicable in our experimental setup. The first method, called the maximum bubble/pressure method, is based on bulging the planar BLMs to one side of the substrate by applying a defined hydrostatic pressure p across the film. When illuminated with transmitted light the membrane contour becomes visible and the radius R of the curved interface can be measured. The interfacial tension γ_{BLM} of the film can now be calculated according to equation 2.7. The second way to determine γ_{BLM} is to measure the half contact angle θ of the lipid monolayers adsorbed at the PGB-water interface (see figure 2.1) [Tie74]. Alternatively, the contact angles of lenses trapped in the BLM can be measured [HT68, Whi86]. Then the relationship between γ_{BLM} and θ becomes [Tie74, Whi86, Iva88]:

$$\gamma_{BLM}(\theta) = 2\gamma_{ML}\cos(\theta) \tag{2.8}$$

γ_{ML} is the interfacial tension of the PGB-water interface in the presence of a lipid monolayer, and can be measured from Langmuir-trough experiments, or by using the maximum pressure method.

The free energy change ΔF of the transition from the bulk to the thinned state can be described as the difference between interfacial tension of the BLM γ_{BLM} and the two monolayers at the PGB $2\gamma_{ML}$ [HT68]:

$$\Delta F = \gamma_{BLM} - 2\gamma_{ML} = 2\Delta\gamma \tag{2.9}$$

By inserting equation 2.8 into 2.9 we get [Whi86, Iva88]:

$$\Delta F = 2\gamma_{ML}(\cos(\theta) - 1) \tag{2.10}$$

From experimental observations we know that $\theta < 90°$ and it follows that the change of free energy ΔF is always negative (see figure 2.4). Consequently, the

formation of a BLM from two monolayers at the bulk film represents a thermodynamically driven, exothermic process. The BLM tension results from differences in interfacial tensions, $\gamma_{BLM} < 2\gamma_{ML}$, in the bulk region and the BLM region. These transformations are driven by several forces, which will be discussed in further detail in the next section. The increase of the contact angle θ during the formation of the BLM area is depicted in a qualitative analysis for the microfluidic BLM experiments in chapter 7.2.2.

The interfacial or bifacial tension of reconstituted membranes is of certain importance for the theoretical and experimental assumptions underlying the x-ray phase contrast imaging experiments, which will be described in chapters 5 to 7. If the film tension is low the bilayer topology will be dominated and defined by thermal fluctuations as it was for example reported for giant unilamellar vesicles (GUVs) by Dimova [DAB+06, GBK+10]. They have determined the effective interfacial membrane tension by micropipette experiments and found values for GUVs of dioleoylphosphatidylcholine DOPC / cholesterol (9/1), ranging from $-5\cdot10^{-6}$ mN/m to $2\cdot10^{-4}$ mN/m. This is much less than it is reported in literature for Black Lipid Membranes. For example Tien has found values for γ_{BLM} of about 1 mN/m up to approximately 10 mN/m [Tie67a, Tie68b]. In recent studies by Mey and Janshoff the authors have used atomic force microscopy to determine γ_{BLM} for solvent containing, pore-spanning nanoBLMs. They report values of 0.15 mN/m$< \gamma_{BLM} <$31 mN/m [MSS+09], which are dependent on the surface properties of the support, i.e. γ_{BLM} increases for surfaces of higher hydrophobicity. This effect can be described by the increasing adhesion forces between substrate and organic solvent in the Plateau-Gibbs border, also called border suction. The values of γ_{BLM} confirm the results of Hirn and Sackmann, who have used dynamic light scattering to determine the interfacial tension and investigate the dynamics of large BLMs, which have diameters of several millimeters. Consequently they are nicely comparable to the BLMs, which are used in this thesis. They have shown that the influence of the bending modulus can be neglected in the description of undulation behavior of membranes with diameters larger than 200 nm [HBRS98]. This is due to the fact that the curvature of the membrane is very small and thus the molecular properties of the surfactants, which determine the bending modulus, become negligible. Hirn and colleagues [HBRS98] found an effective undulating amplitude of only 0.09 Å on a length scale of about 60 µm for a BLM with a diameter of 3.5 mm and a surface tension of 1 mN/m. Summation over all oscillations, on scales reaching from the membrane thickness (5 nm) to the membrane diameter (3.5 mm), gives a maximum undulation amplitude of 1 nm. Both values are (much) smaller than the membrane thickness $d \approx 5$ nm and will consequently have a negligible effect on the visualization of the BLM and the resolution of d, respectively.

2.2   Intermolecular forces in BLMs - DLVO theory

Plateau studied the nature of capillary forces and surface tensions in soap films [Pla73]. Gibbs was the first who explained the appearance of "black holes" in soap films linked to the thinning of the interface [Gib48, Gib61]. Based on these experiments other research groups started theoretical and experimental investigations of forces in soap films in air [MSF59, Ove60, Mys64, Mys68]. The reconstitution of Black Lipid Membranes enabled the adaptation of these theoretical concepts from soap film experiments to bimolecular films in aqueous solution [HT68, Whi70, AMH70, NP70]. Both systems and the theoretical descriptions of the forces, which drive them, are in perfect analogy to each other (see figure 1.1).

When a solution of solvent/oil and amphiphilic surfactant molecules is "painted" across an aperture in a hydrophobic aperture, which is immersed in an aqueous solution, the surfactant molecules immediately assemble at the water-oil interface [Tie68b, Tie74, Whi86] to form a monolayer (see figure 2.2). Such films, which will be referred to as bulk films, usually range from 1 μm to 100 μm in thickness [TD66, VST$^+$66, Whi70]. Due to the adhesion forces between the organic solvent and the hydrophobic substrate, e.g. the Teflon foil, a spontaneous formation of the PGB is induced at the rim of the aperture (see figure 2.2). Consequently, this adhesive force will suck the organic solvent from the bulk film. It was shown in section 2.1, in the law of Laplace and Young (see equation 2.3), that the PGB acts as a region of low pressure. The bulk film will start to thin down to about 100 nm thickness [Tie68a, Whi70], where the van der Waals forces are still negligibly small (see figure 1.2). At layer spacings below this critical value of about 100 nm, local, stochastic instabilities, such as thermal motions, mechanical vibrations, impurities or local variations of the interfacial tension can induce a spontaneous thinning of the swollen film to form a bimolecular membrane [TD66, Wil89]. At this point the membrane will become black in reflected light, meaning it reaches thicknesses much smaller than the wavelength of the visible light used[1]. These regions are called secondary or Newton black films [TOL00, TD66]. The black spots grow at a fairly constant rate, which can be viewed as a "zipper-like" effect [FFI03, TD66]. This second step of thinning proceeds from interlayer distances of about 60 nm down to the final membrane thickness d of approximately 4 nm to 5 nm, which is nearly twice the molecular length s of the surfactant molecules [Whi70, VGIB95]. This last step of the film transformation can be described in the context of van der Waals interactions [Lon30, Isr92].

---

[1]Physical explanations of the development of interference colors and the final black spots were discussed in [Bee06, New74, Hoo57, Boy59].
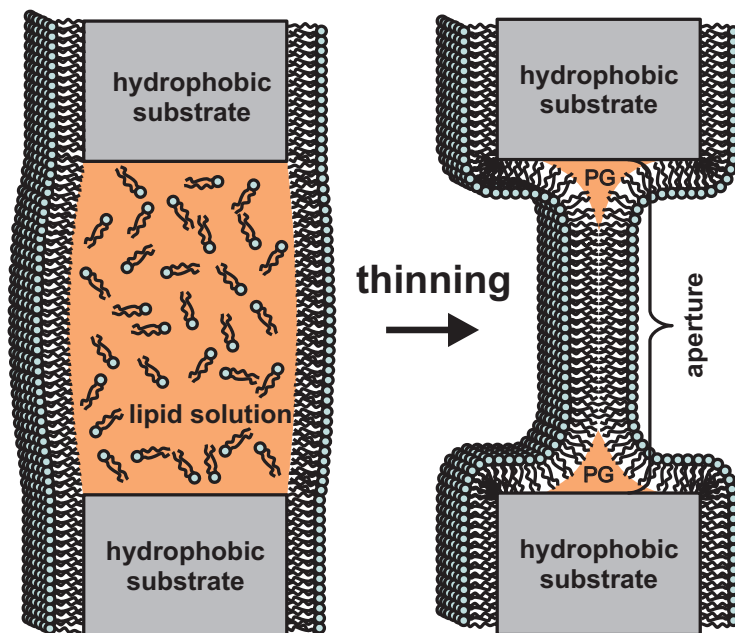
Figure 2.2: *Schematic representation of the thinning of a bulk film, which is prepared from a lipid-solvent solution across an aperture in a hydrophobic substrate. At the beginning of the process the amphiphilic lipid molecules form a monolayer at the solvent-water interface. Adhesion forces drive the organic solvent to assemble at the hydrophobic substrate where they form the Plateau-Gibbs border (PGB). Consequently the film starts to thin. At thicknesses below 100 nm the van der Waals interaction starts dominating the formation of the bimolecular Black Lipid Membrane.*

The following considerations are based on the Derjaguin, Landau, Verwey, and Overbeek (DLVO) double-layer theory [DL41, VO48, Ove60, VST$^+$66], playing a key role in the understanding of the BLM formation process [Isr92, MJ66, VGIB95]. Two different principle forces drive the thinning of a BLM and need to be discussed.

At first the process is dominated by the *attractive van der Waals dispersion potential U_{vdw}*. This potential is always attractive in the case of symmetric bulk layers, e.g. soap and emulsion films [MN05]. It describes the interaction between both the two bulk water reservoirs and the two monolayers across the organic solvent, which separates them [Isr92, HT68, Whi70, AMH70, Req75, Whi86, MN05].

For derivation of the potential energy $U(d')$ of two surfaces interacting across another medium at distance d' we follow the theoretical approach, which is formulated in reference [Isr92]. Note, that in this section d' always denotes the interlayer distance, i.e. the thickness of the solvent layer, which separates them. The total membrane thickness d is consequently composed of d' and twice the length of the lipid molecules s, so that $d = 2 \cdot s + d'$.
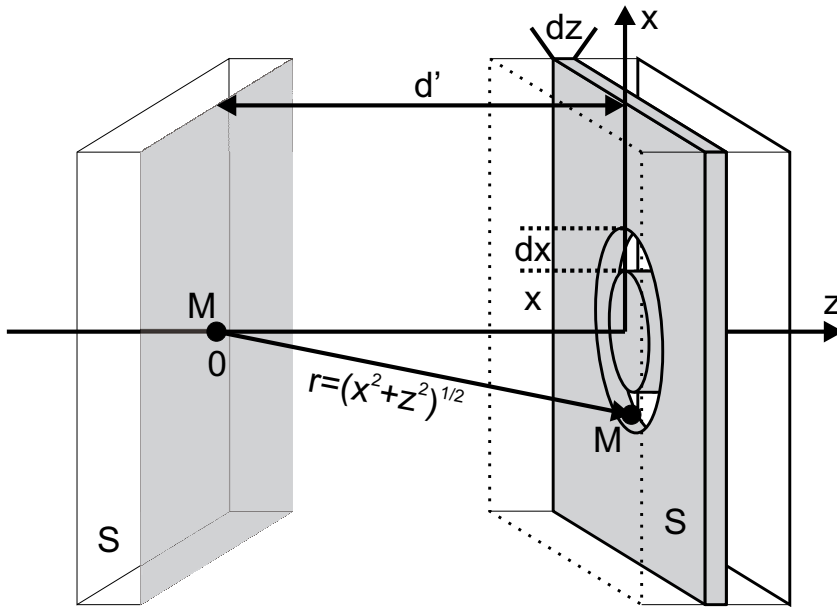
Figure 2.3: *Schematic representation used for the derivation of the interaction potentials between two surfaces at a distance d'.*

In the case of van der Waals interactions the potential $u(r)$, which accounts solely for the pair correlations between two molecules M at distance r (see figure 2.3), can be written as

$$u(r) = -\frac{C}{r^6} \tag{2.11}$$

where C is an element specific constant. For an extended body the overall interaction $U(r)$ is the interaction of one molecule with all other molecules $N = \rho V$ of density ρ in volume V

$$U(r) = \int_V u(r)\,\rho\,dV \tag{2.12}$$

In the case of a single molecule M facing an infinite flat surface of molecules, the volume of a ring with radius x inside this surface at distance d' (along the z-axis) is $V = 2\pi\,x\,dx\,dz$. The number N of molecules inside this ring is then given by $N = 2\pi\rho\,x\,dx\,dz$. Including N and the radius $r = \sqrt{x^2 + z^2}$ into equation 2.12 the total interaction potential becomes:

$$U(d') \;=\; -2\pi C\rho \int\limits_{z=d'}^{z=\infty} dz \int\limits_{x=0}^{x=\infty} \frac{x\,dx}{\sqrt{x^2 + z^2}^6} \tag{2.13}$$

$$=\; -\frac{\pi C\rho}{2} \int\limits_{z=d'}^{z=\infty} \frac{dz}{z^4} \tag{2.14}$$

$$=\; -\frac{\pi C\rho}{6\,d'^3} \tag{2.15}$$

When replacing the single molecule by an additional opposing surface of unit area and infinitesimal thickness dz, we also have to take into account the number of molecules in this second surface. Consequently, the number of molecules becomes $N = \rho\,dz$ and we obtain, according to equation 2.15, an interaction energy of $-(\rho\,dz)\frac{\pi C\rho}{6\,d'^3}$. From this we can now calculate the total potential energy $U(d')$ per unit area:

$$U_{vdw}(d') \;=\; -\frac{\pi C\rho^2}{6} \int\limits_{z=d'}^{z=\infty} \frac{dz}{z^3} \tag{2.16}$$

$$=\; -\frac{\pi C\rho^2}{12\,d'^2} \tag{2.17}$$

$$=\; -\frac{H}{12\,d'^2} \tag{2.18}$$

$$\tag{2.19}$$

with the pressure $P_{vdw}(d')$ respectively:

$$P_{vdw}(d') = \frac{H}{6\pi\,d'^3} \tag{2.20}$$

H is called the Hamaker constant[2] for two media I interacting across a second medium II (see figure 1.2). The van der Waals potential, which is defined by equation 2.18, is plotted in figure 2.4 against the film thickness d, according to results obtained in references [Whi70, HW80, WHLH95, Isr92]. Another

---

[2]The calculation of Hamaker constants H based on the Lifshitz theory is extensively described in [HW80, Isr92]. An experimental way to determine H is shown in [HT68]

approach used in literature to describe the van der Waals potential is the Lifshitz theory, which is based on a continuum treatment of the media using their macroscopic dielectric properties [NP70, BLRH75, RBH77, Isr92].
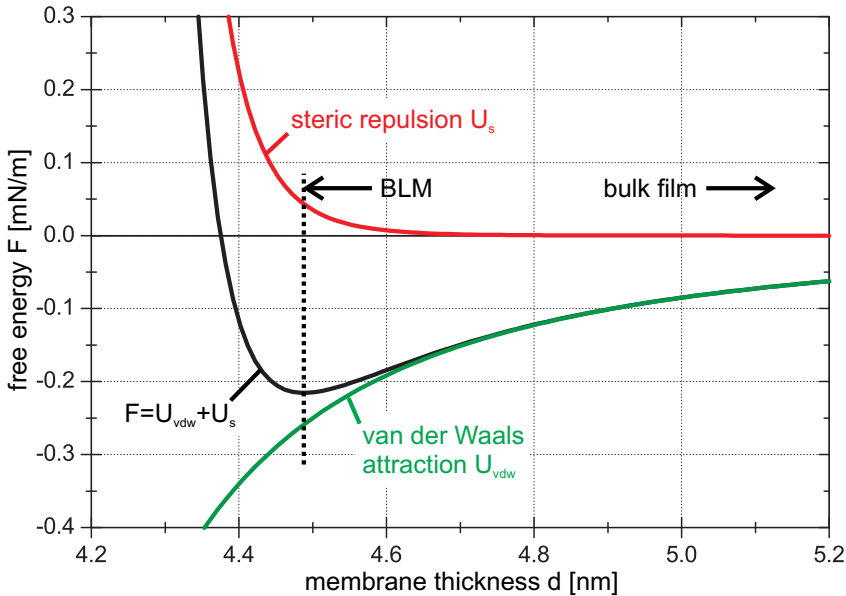
Figure 2.4: *The graph shows a hypothetical relationship between free energy F per unit area (equation 2.22) and the film thickness d for the attractive van der Waals potential U_{vdw} (equation 2.18) and repulsive steric potential U_s (equation 2.21) of two lipid monolayers (DPhyPC) adsorbed at the interfaces of a film of n-decane film in water. (Parameters: $H = 4.62 \cdot 10^{-21}$ J [HW80], $n_m = 1.32 \cdot 10^{14}$ cm^{-2} [WHLH95], $2 \cdot s = 3.8$ nm [WHLH95], $\epsilon = 5.5 \cdot 10^{-21}$ J (benzene) [Whi70], $\sigma_{CH_3} = 0.4$ nm [Isr92].)*

In addition to the van der Waals potential we need to consider the *steric repulsion potential U_s*, which originates from the molecular structure of the surfactant molecules. The steric repulsion occurs over a short range but is of relevant strength [Whi70, Tie74, RBH75, Isr92]. One option is to model this as a hard-wall/-sphere barrier, that allows no overlap of the lipid´s hydrocarbon chains [Isr92]. Alternatively, it can be considered as just the repulsive part of the Lenard-Jones potential [Whi70], which is

$$U_s(d') = 4\,n_m\epsilon\left(\frac{\sigma}{d'}\right)^{12},\tag{2.21}$$

with number density n_m of molecules per area with the repulsive energy ϵ and radius $r = \sigma/2$ of the terminal group of the molecule.

Finally, the total free energy per area F in dependence of the membrane thickness $d = 2 \cdot s + d'$ is defined as the sum of the previously described potentials

$$F(d) = U_{vdw} + U_s = -\frac{H}{12\pi d^2} + 4\,n_m\epsilon\left(\frac{\sigma}{d}\right)^{12}. \tag{2.22}$$

Figure 2.4 presents a hypothetical plot of the free energy F, given by equation 2.22, against the membrane thickness d for the case of a Black lipid Membrane made from DPhyPC molecules. Furthermore, the graph in figure 2.4 shows the individual contribution of the van der Waals attraction U_{vdw} (equation 2.18) and the steric repulsion U_s (equation 2.21) to F. The parameters used to plot the previous equations in figure 2.4 are denoted in the figure caption and describe the properties of a membrane reconstituted of DPhyPC molecules. It can be obtained from the graph that the free energy F, which is set free during the transition from a bulk film to a thinned BLM, is approximately $\Delta F = -0.22\,\text{mN/m}^2$. This is in the order of magnitude of the values obtained from contact angle changes of mfBLMs shown in figure 7.16 of chapter 7.2.2.

If an *electric field* V_m/d is applied across a membrane with capacitance C_m an additional compressive potential $U_v < 0$, will act on the monolayers, which are separated at distance d by a layer of organic solvent. The authors of references [AMH70, WT73, Cro73, Whi86] defined this contribution to the free energy F as the potential energy $E = -\frac{C_m V_m^2}{2}$ stored in a capacitor. By insertion of the specific capacitance c_m into the potential energy E one obtains the free energy per unit area

$$U_v = -\frac{c_m V_m^2}{2} = -\frac{\varepsilon_0\,\varepsilon_m\,V_m^2}{2d} \tag{2.23}$$

This attractive potential will shift the whole potential to more negative values and, thus, the minimum in $F(d)$ will be located at smaller membrane thicknesses. As a consequence a solvent-containing lipid bilayer in an externally applied electric field will thin. Note, that no further thinning mechanisms, such as lipid tilting, are considered so far. We will get back to equation 2.23 with a discussion of this effect in chapter 3.4.

The *repulsive, electric double-layer potential* U_{edl} for charged surfaces [TH66a, HT68, RBH75] can be neglected here, since the membranes, which have been used in the presented experiments, are composed of uncharged lipids. The consideration of this potential is more relevant and contributes to the final free energy F more strongly in the case of soap films [MJ66] and interfaces exposed to electrolyte solutions of high ion concentrations [Isr92, MJ66, MN05]. Furthermore, this interaction plays a great role in the description of charged

bilayer-bilayer interactions, e.g. the initial steps of membrane fusion. The repulsive nature of U_{edl} can be understood as follows. The Gouy-Chapman surface potentials of both membranes will interact and repel each other due to electrostatic repulsion like for highly charged lipids, e.g. lipopolysaccharides. If those charged surfaces are exposed to electrolyte solutions they will always be accompanied by a counter ion layer. At smaller membrane-membrane distances these counter ion layers will overlap and the local ion concentration is increased. Consequently, an osmotic flow of solvent or water into the gap between the two surfaces is induced, which also leads to a repulsive force. These interactions can create a secondary minimum in the free energy [Isr92], which allows the monolayers to stay at metastable distances, also known from aggregation or flocculation of colloidal particles. The absence of this long-range repulsive potential can lead to instabilities and spontaneous rupture of thin surfactant films [VGIB95].
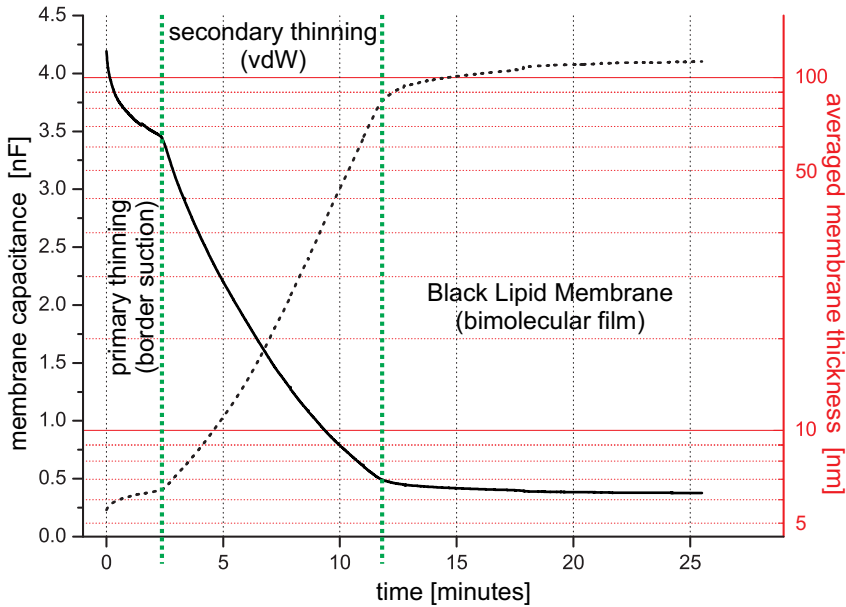
Figure 2.5: *The graph shows the experimental data, which are obtained by investigating the different thinning mechanisms during the transition from a bulk film to a BLM. The border suction can be clearly distinguished from the regime, which is driven by the van der Waals interactions. They membrane capacitance (dotted line) is monitored by using the Lock-In method (see chapter 3.2.3). The averaged thickness (solid line) of the film is derived according to equation 1.2. See text for experimental details.*

Finally *no retardation effects* are considered in equation 2.22, i.e. we assume the interaction ranges to be short enough that the electric field propagates much faster between two dipoles than the timescales, on which the dipolar reorientation takes places [AMH70, Whi70].

Each of the above two mechanisms of membrane thinning is dominated by two different driving force: first the adhesive force, namely the border suction of the PGB, and secondly the van der Waals forces, which starts to act when the bulk film thickness becomes less than about 60 nm to 100 nm. Figure 2.5 shows an experiment, where we have monitored these two different thinning regimes of a diphytanoylphosphatidylcholine (DPhyPC) membrane in an aqueous buffer solution. The membrane capacitance is measured by using the Lock-In method (see chapter 3.2.3). The resulting thickness is calculated according to equation 1.2 and is considered to be an average value over the whole film area $A = \pi R^2$.

The experimental values, which are used for the calculation of the thickness d, are: $\varepsilon_0 = 8.8542 \cdot 10^{-12} \frac{As}{Vm}$, $\varepsilon_m = 2$ and R=700 μm.

2.3   Marangoni effect in (bulged) BLMs

An interesting effect, called the "Marangoni effect" [SS59, SS60], is observed in the experiments and it has shown to play an important role in the expansion and thinning of bimolecular films.
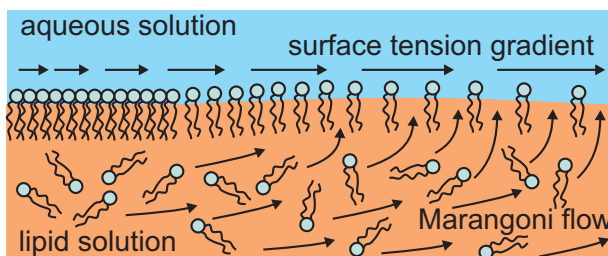
Figure 2.6: *Schematic representation of the Marangoni effect: A surface tension gradient in an interface, which is composed of surfactant molecules, induces a Marangoni flow of the molecules in the bulk phase towards the region of maximum surface tension. In bulged BLMs this leads to a local increase in membrane thickness.*

The Marangoni effect is described as follows: An interfacial tension gradient of a molecular layer, which is assembled at the interface between two phases, e.g. water and solvent (see figure 2.6), will induce further adsorption of surfactant molecules at the interface [Wil89, FFI03]. As a consequence a Marangoni flow of solvent towards the region of highest tension is generated to provide the supply of surfactant. When these molecules adsorb at the interface the local tension, which is higher in the absence of surface active molecules, is reduced again. If we consider a BLM, which is bulged by an applied hydrostatic pressure, the interfacial area is increased compared to the planar state. As long as no new material has migrated into the film [Tie67a, Wil89], the surface concentration of the surfactant molecules decreases and the interfacial tension increases. Based on the Marangoni effect a flow of organic solvent with dissolved lipid molecules rushes from the PGB into the BLM, the monolayers are separated, and the film thickness increases. After the bulging process is stopped and the tension gradient is compensated by the Marangoni effect, the van der Waals interactions will dominate to recreate a thinned state of the bimolecular membrane again. The Marangoni effect can be seen as a self stabilizing mechanism in the mem-

brane. It always responds to local curvatures, which occur during the thinning process at the transition region and induce an interfacial tension increase, by a thickening of the membrane. This resistance of a film to thinning is known as the Gibbs elasticity [Gib48, Mys64, HT68]. Due to permanent presence of local thickness instabilities, which are induced by thermodynamic fluctuations and local disturbances the Marangoni effect will always drive domains of residual organic solvent, to be kept in the membrane [AH68, AMH70, WT73]. A formation of such a phase separated alkane layer has been reported [Whi80] and can strongly effect the membranes structural properties and functionality in terms of transmembrane protein insertion.

2.4   Solvent-free lipid bilayers

To circumvent the potential effects of residual solvent inside reconstituted membranes, Montal and Müller [MM72, Mon74] developed an alternative preparation technique allowing for the reconstitution of asymmetric bilayers.
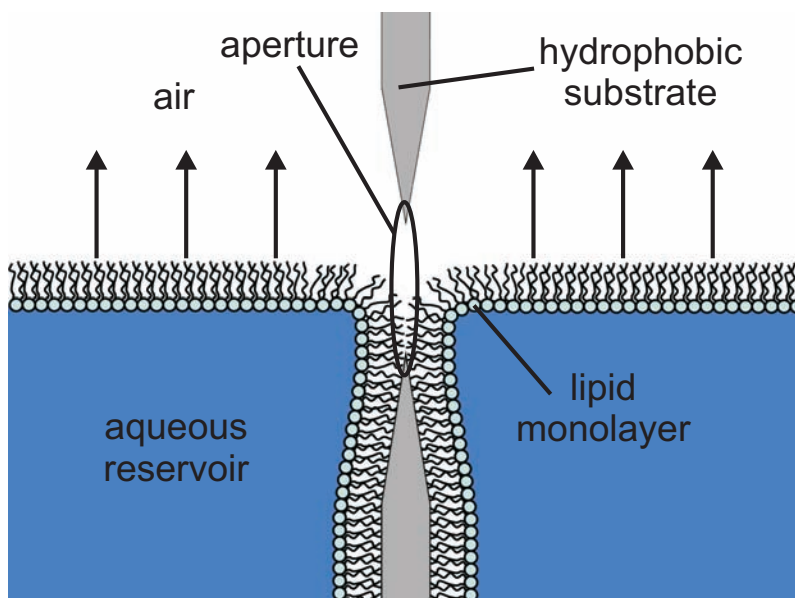
Figure 2.7: *Schematic representation showing the formation of a freestanding, solvent-free lipid bilayer from two monolayers composed of amphiphilic molecules.*

A droplet of surfactant molecules, e.g. lipids, dissolved in organic solvent is spread on each surface of two aqueous compartments separated by a hydrophobic substrate that includes an aperture placed right above the water level (see figure 2.7). On evaporation of the organic solvent a monolayer assembles at the air-water interface. Subsequently, the water levels are slowly raised above the aperture. The monolayers, which can each be made from a different combination of surfactant molecules, will fold across the supporting substrate and cover the aperture, where they come into contact to form a bilayer membrane. The asymmetry in the lipid leaflets makes these membranes a suitable experimental model system for the reconstitution of bacterial outer membranes, which are composed of a phospholipid and a lipopolysaccharide monolayer [HWSG04, Wie01].

Although they are called "solvent-free" lipid bilayers there is always a small amount of organic solvent required at the beginning of the preparation. It is used to functionalize the surface of the supporting substrate and stabilizes the BLM in the transition region at the aperture rim. This was also concluded from theoretical discussions of surface tension and geometrical assembly of the lipid layers [WaSSY76, Whi86]. Consequently, formation of these membranes without using any solvent is impossible, and the presence of the Plateau-Gibbs border is of essential importance to provide the membrane´s stability.

It was shown by electrophysiological measurements that the voltage dependence of the membrane capacitance is remarkably reduced for this type of model membrane [BOLM75, Whi78, VM82], when compared to those previously described membranes, which are "painted" from solutions of lipids and organic solvent. Considering equation 2.23, the experiments indicate that structural changes of BLMs in electric fields and related changes of capacitance are mainly caused by residual organic solvent in the film [BEL66, Ohk69, Whi70, Wob72, Whi80].

3 Membranes in electric fields

To understand the electrostatics of a membrane system we need to consider the single components. In particular, we need to consider their electrical and switching properties and how they can be measured. The structural effect arising from transmembrane, or externally applied potentials, is discussed in this chapter. Finally, x-ray reflectivity experiments, which have been performed to investigate the electric field effect, are presented.

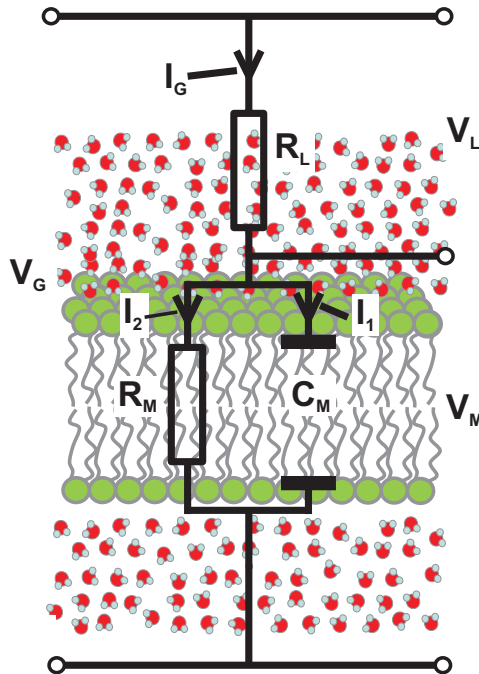## 3.1 Electrostatics and equivalent circuit of BLMs

Figure 3.1: *Schematic representation of the equivalent circuit of a freestanding lipid membrane in an aqueous environment.*

The equivalent circuit of a lipid membrane, which is immersed in a conductive aqueous buffer solution, is shown in figure 3.1. Such an interface can be described as an insulating capacitor with a capacitance C_m (see equation 1.2).

As a bilayer is always found to have defects, and thus is never a perfect insulator, we introduce a membrane resistance R_m. Consequently we can define a leakage current I_m of ions passing the interface, which is composed of a capacitive current I_1 and a resistive current I_2 with $I_2 \gg I_1$. The bilayer is usually prepared in a buffer solution and signals are measured by electrodes, which together have a resistance R_L. The potential $V_G = I_G \cdot (R_m + R_L) = I_G \cdot R_G$ drops across the whole system and can be divided into the electrode and solution potential V_L and the transmembrane potential V_m, which will be described in detail in section 3.3. In the following the specific capacitance will be denoted as c_m and the specific resistance as r_m. Characteristic values of the introduced parameters can be found in [Bee06, TOL00, TOL03].

3.2 Determination of membrane capacitance

In the subsequent section three different methods which are used to determine the Capacitance C_m of Black Lipid Membranes will be presented. It was already discussed in chapter 1.2 that the thickness of the Plateau-Gibbs border is several orders of magnitude larger than in the bilayer region [Whi72]. Consequently, its contribution to the capacitance, which is described by equation 1.2, will be neglected in the following determinations of C_m.

3.2.1 Membrane capacitance derived from charging current

One method for the investigation of the specific membrane capacitance c_m is to charge the bilayer by an applied voltage step ΔV_m. The response of a lipid bilayer in an aqueous environment to such an excitation will consist of a sudden increase of the current and a subsequent exponential decay of characteristic time τ_m [ALS03]:

$$V_G(t) = I_G R_G \left(1 - e^{-t/\tau_m}\right), \quad \tau_m = R_m C_m = r_m c_m, \quad V_\infty = I_G R_G. \tag{3.1}$$

V_∞ is the resting potential after excitation and is directly accessible in the experiment as well as τ_m, I_G, and R_L. Consequently R_G and finally $R_m = R_G - R_L$ are obtained. The membrane area A can be determined by microscopy, which leads to the membrane capacitance C_m. By using $c_m = \frac{C_m}{A}$ and $r_m = R_m A$ the specific bilayer parameters can be calculated.

3.2.2 Voltage jump method

The *voltage jump method* [AL78, GLSW99, Hag03, Bee06] enables a direct extraction of the capacitance C_m from the charging characteristics of the mem-

brane. Based on the previously described method it consists of a series of voltage steps V_m (figure 3.2(a)) being applied to the bilayer. The height of a charging current, which occurs upon excitation by a voltage pulse, is proportional to the capacitance C_m of a capacitor. As a consequence, a series of such pulses will result in a comb-like current signal (figure 3.2(b)). By application of a low pass filter to the signal (1 kHz) the capacitance C_m can be derived from the area under the rectangular current response of the system, which is equivalent to the charge Q of the capacitor:

$$Q = \int_0^T I \, dt \propto C_m \tag{3.2}$$

A drawback of the technique is that it only yields a maximum acquisition rate of about 1 Hz [GLSW99] and a calibration of the system with known capacitors is required.
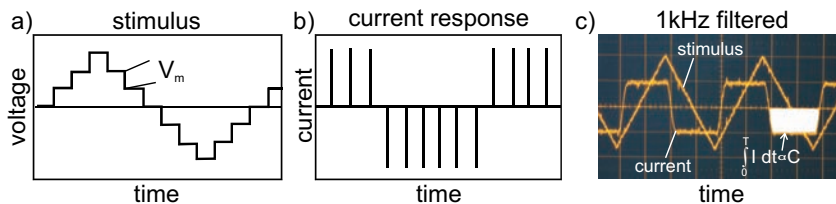
Figure 3.2: *(a) The membrane is excited by a triangular stimulus that increases and decreases in a stepwise manner. (b) The current response shows a comb-like structure. (c) After system calibration and signal filtering the membrane capacitance C_m can be derived from the (white) area under the rectangular current signal.*

3.2.3 Lock-In method

A more elegant way to measure the capacitance C_m of the BLM is to use a sinusoidal wave excitation $V_m(t)$ and measure the current response I_m of the system. The patch clamp amplifier HEKA EPC10 (HEKA; Germany) is already equipped with a script that creates such signals and simultaneously analyzes the feedback [Int09]. The membrane is excited by an oscillating voltage

$$V_m(t) = V_0 \cdot \sin(\omega t) \tag{3.3}$$

with an angular frequency ω. The response of a membrane system (see section 3.1) will consist of a resistive current $I_R = \frac{V_m(t)}{R_m}$, as well as a capacitive current $I_C = C_m \cdot \frac{dV_m(t)}{dt}$. At the peak of the sine wave, where $\frac{dV_m(t)}{dt} = 0$, only a resistive

current is obtained and R_m can be derived. The contributions to R_m from electrodes and buffer solution can be determined and separated out immediately. At the inflection points of the sine wave, where $V_m(t) = 0$, only I_C is measured and by using the derivative of equation 3.3 we obtain:

$$I_C = C_m \cdot \frac{dV_m(t)}{dt} = C_m \cdot \omega \cdot V_0 \cdot \cos(\omega\, t) \tag{3.4}$$

From knowledge of the experimental parameters, ω, I_C and V_0, the membrane capacitance C_m can be calculated.

3.3   Transmembrane potentials

The cell membrane is impermeable to all kinds of large, (partially) charged, hydrophilic molecules. Only some smaller, mainly uncharged molecules, and, to some extend, even water and hydrophobic ions are able to pass the hydrocarbon core of a lipid bilayer [HL82, Sac95, ALS03, Hei07]. All other particles are unable to cross the highly selective permeability barrier of phospholipids without using specific modifiers. Thus, the cell membrane can also be seen as a protective layer, shielding the organelles inside against menaces from the outside world, e.g. viruses and bacteria. To preserve the cellular functionality the plasma membrane is provided with proteins acting as ion channels or pore like transmembrane proteins (porins). Furthermore the direct creation of membrane pores [Dea08, MSK+08] enables an exchange between cell interior and its environment. These events, i.e. opening and closing of channels, can be controlled by different parameters depending on the function and location of the molecules.
The mechanism of voltage-sensitivity plays an important role in the functionality of transmembrane proteins. Many ion channels sense the electric potential across the membrane and can undergo voltage-dependent conformational changes [Hil84, Alb94]. In this section the transmembrane potential and how it is determined by the ionic strength in- and outside the cell will be briefly described according to [ALS03, Hei07].

3.3.1   Nernst equation

In 1889, Nernst derived an equation that relates the electric field across a semipermeable membrane to the ion concentrations in the extracellular fluid c_a and the cytosol c_i (see figure 3.3).
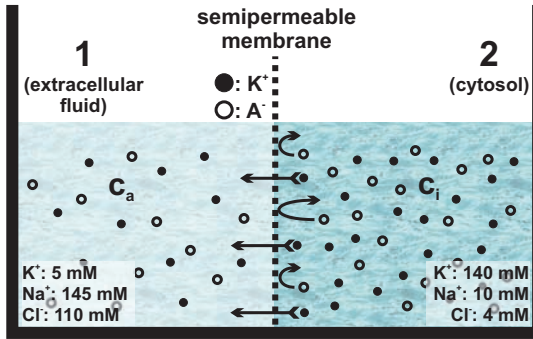
Figure 3.3: *The Nernst equation describes the electrical potential across a semi-permeable membrane which arises from differential ionic distribution between the extracellular fluid, c_a, and the cytosol c_i.*

Due to the fact that $c_i \neq c_a$, the K^+ ions, which are depicted in figure 3.3, will cross the membrane following the concentration gradient [ALS03]. The Gibb's free energy difference is given by

$$\triangle G_{conc} = +R_c T \cdot ln \frac{c_a(K)}{c_i(K)}. \tag{3.5}$$

As a consequence the electrochemical potential V_m between both compartments will increase and an additional free energy difference occurs. It will be of the opposite sign, since the diffusion potential and the electrochemical potential are counteracting:

$$\triangle G_{volt} = -zF_c V_m \tag{3.6}$$

with gas constant R_c, absolute temperature T, ion valency z, and Faraday constant F_c. The **Nernst equation** describes the equilibrium state where equation 3.5 and 3.6 compensate:

$$\triangle G_{ges} = \triangle G_{conc} + \triangle G_{volt} = R_c T \ln \frac{c_a}{c_i} - z F V_m = 0 \Rightarrow V_m = \frac{R_c T}{z F} \ln \frac{c_a}{c_i} \tag{3.7}$$

3.3.2 Goldmann-Hodgkin-Katz equation

To calculate the resting potential for a stationary system including different ion types we need to consider the ion fluxes across the membrane. Here we follow the derivation given in [ALS03]. The ion flux density will be composed of diffusive and electric field components

$$\Phi = \Phi_{diff} + \Phi_{el} \tag{3.8}$$

where Φ_{diff} is given by Fick's first law: $\Phi_{diff} = -D\frac{dc}{dx}$ including the diffusion coefficient D.

Ions of valency z in an electric field of strength E experience the force

$$K_x = z\,e_0\,E_x = -z\,e_0\,\frac{d\varphi}{dx} \tag{3.9}$$

with Stokes friction $-R_S = K_x = f\,v_x = 6\pi\eta\,rv_x$, elementary charge e_0, electric potential φ, particle radius r, and velocity v. From Einstein´s diffusion relation we obtain $f = \frac{k_B T}{D}$. With $e_0 = F_c/N_A$ and $k_B = R_c/N_A$ it follows that

$$\Rightarrow v_x = -D\frac{z\,F_c}{R_c\,T}\frac{d\varphi}{dx} \tag{3.10}$$

With $\Phi_{el} = c\,v_x = -c\,D\frac{z\,F_c}{R_c\,T}\frac{d\varphi}{dx}$ we obtain the **Nernst-Planck-Equation** describing the flux density of ions with valency z in the stationary state:

$$\Phi = \Phi_{diff} + \Phi_{el} = -D\left(\frac{dc}{dx} + c\,z\frac{F_c}{R_c\,T}\frac{d\varphi}{dx}\right) \tag{3.11}$$

If the membrane is considered to be a charge free region, the electric field inside will be constant and the potential φ depends linearly on the position x so that we obtain

$$\frac{d\varphi}{dx} \approx \frac{\varphi_a - \varphi_i}{d} = -\frac{V_m}{d}. \tag{3.12}$$

with the membrane thickness d and the transmembrane potential V_m. Following the assumption in equation 3.12 the integration of equation 3.11 can be performed (see [ALS03]) and it follows

$$\Phi = \frac{D}{d}\frac{z\,F_c\,V_m}{R_c\,T}\frac{c_i\,e^{\frac{z\,F_c\,V_m}{R_c\,T}} - c_a}{e^{\frac{z\,F_c\,V_m}{R_c\,T}} - 1}. \tag{3.13}$$

For a resting system, which is composed of K^+, Na^+, and Cl^- ions, the overall ion currents vanish, $j = F\sum_i z_i\Phi_i = 0$, so that follows:

$$\Phi_K + \Phi_{Na} - \Phi_{Cl} = 0 \tag{3.14}$$

From the insertion of equation 3.13 into equation 3.14 we finally get the **common Goldman-Equation** (for monovalent ions)

$$\Rightarrow V_m = \frac{R_c\,T}{F_c}\ln\frac{\sum P_{Kat}\,c_{Kat}^a + \sum P_{An}\,c_{An}^i}{\sum P_{Kat}\,c_{Kat}^i + \sum P_{An}\,c_{An}^a} \tag{3.15}$$

$P_{Kat,An}$ denotes the permeability of the membrane for cations and anions and $c^{a,i}$ the respective concentrations outside and inside the cell. For a mammalian

cell with the ion concentrations, depicted in figure 3.3, a resting potential $V_m \approx -70\,mV$ can be calculated [Hil84, Alb94, ALS03]. It has to be mentioned that so far no active transport across the membrane, e.g. by ion pumps or carriers, is considered here.

We can conclude that transmembrane potentials are predominantly determined by intrinsic parameters relative to the membrane, e.g. ion concentrations, which induce electric potentials (Nernst, see equation 3.7), or externally applied electric fields. But, additionally, in a membrane there are always intrinsic potentials [Ohk80, Cev90, PML$^+$02], which rise from the electrochemical characteristics of the membrane itself. These potentials, namely the Gouy-Chapman [McL89, Cev90, Hei07], the Born-image [NL69, FH86] and the dipole potential [LT69, FH86, GRZ$^+$92, ZV92, Bro94, Cla01] are summarized in a model by Schoch [SSS79]. The investigation of intrinsic membrane potentials reveals information about both interactions and reactions taking place at the membrane surface. Furthermore, processes inside the membrane can be studied, e.g. protein adhesion and incorporation, channel formation and ion transport, or even structural changes in the lipid layers [LT69, SSS79, SK80, GLSW99, PML$^+$02, HWSG04].

3.4 Electric field effect on membrane structure

We have already discussed that biological membranes are always accompanied by electric fields originating from different ion concentrations being present on both sides of the bilayer (see equation 3.15). In this work we investigate the question whether such electric potentials are strong enough to induce changes in the membrane structure and, if so, how this process can be described. If the membrane responds to a change of the electric potential by a conformational change, i.e. variation of its thickness according to equation 2.23, this could also have an important impact on membrane protein orientation and their functionality.

A bimolecular film can change its thickness in basically two ways. After "squeezing" the remaining solvent towards the Plateau-Gibbs border, it can undergo further thinning by overcoming the steric repulsion of the hydrocarbon core. This will at the end result in an interdigitation of the hydrocarbon chains. Due to the steep increase of the repulsive term U_s in the interaction potential (see equation 2.22), this is very unlikely [Whi70] and can only happen for strong applied potentials far above the electrophysiological conditions inside the cell [VST$^+$66, TH66a, AMH70]. Based on the results in literature we have discussed in chapter 2.4 that this effect of electrocompression is negligible in solvent-free membranes. There it was shown that the absence of interdigitation perfectly matches the experimental observations [BOLM75, Whi78, WC81, VM82]

in this type of model membrane. In these experiments the membrane showed no thickness changes on a variation of the applied potential on length scales of the achievable resolution. Alternatively to the effect of electrocompression, the cell membrane thickness can change due to modifications of the molecular orientation of the lipid molecules in the bilayer. A potential reason for this could be the strong dipolar characteristics of the lipid headgroups [Stu81]. For example the dipole moment of the amino-phosphate-complex in a phospholipid is about 24 Debye [Gup72, Haw06], which is ten times larger than that of a water molecule. Tilted by an angle of about 70° with respect to the plane of the membrane normal it leaves a component of 25% that points perpendicular to the membrane [WE04b]. Since a bilayer consists of two monolayers their dipolar moments would be diametrically opposed. Thus, if an electric potential is applied perpendicular to the membrane we can think of one layer that would orientate co-linearly with the field while the other one tries to compensate the external force by an increase of the tilt angle [Tei07]. A schematic representation of this hypothetical process is shown in figure 3.4.
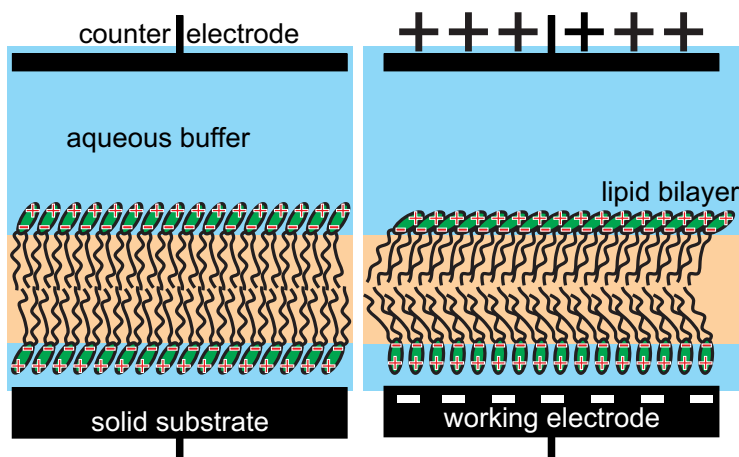
Figure 3.4: *Schematic representation of the supposed conformational change of the lipids in the bilayer membrane in an externally applied electric field [Tei07]. Due to the relatively large dipole moment in the lipid headgroup regions of 24 Debye, which is a magnitude larger than in a water molecule, the lipids might tilt so that the membrane thickness decreases.*

Consequently, the lipid hydrocarbon chains will tilt and the membrane thickness decreases. If the conformational change is more complicated due to the presence of steric hindering in one of the layers an asymmetric thickness change

might be expected. Such thickness change might be much smaller and consequently impossible to be detected by means of light reflectivity or electrostatic measurements (see chapter 1.2). Due to insufficient resolution the underlying membrane models of these techniques, e.g. considering a single hydrocarbon layer with a given dielectric constant, will not be able to describe asymmetric structural changes inside the membrane.

It was shown that a bimolecular film, which is exposed to strong electric fields above 10^8 V/m, usually undergoes electroporation [TO03]. This can lead to irreversible electrical breakdown [Cro73], i.e. rupture of the film. Charitat and colleagues have performed high resolution neutron studies of floating bilayers, which are exposed to electric potentials in aqueous environments. They have obtained no thickness changes even for strong, alternating electric fields (10^9 V/m, 10 Hz) [LFC06, CLF08]. These results were consistent with reference experiments using solely single bilayers, which were bound to the substrate. Besides an increase in membrane roughness and an increase in the membrane substrate distance no changes of the lipid bilayer structure were obtained. The results of membrane unbinding are in perfect agreement with the observations from former studies, which were performed by our group [COVS05]. There the effect of AC fields on multilayer membrane stacks was studied. Step by step the membranes were detaching from the lower membranes, which were bound to the substrate. This electric field destabilization has been described theoretically [SI02] and is well known as "electroswelling" or "electroformation", and is used in the reconstitution process of giant unilamellar vesicles. Burgess and coworkers [BLH+04, BLH+05] report on an increase of the water layer thickness between the membrane and the supporting electrode for electric DC potentials. At the same time the membrane thickness shows an increase of about 40% from +50 mV to -950 mV. This relatively large variation is interpreted to be related to swelling of the film by ingression of water molecules. For higher membrane potentials $V_m > 5 \cdot 10^8$ V/m they observed a fully reversible unbinding of the lipid layer from the gold surface, comparable to the previously obtained results in AC fields. The controversial results regarding the membrane thickness change, which are obtained by Burgess and Charitat, might originate from the fact that Burgess studied the effect in DC and Charitat in AC fields. As far as can be deduced from literature this is the only difference in the experiments since in both cases uncharged phosphatidylcholine membranes were prepared on gold coated substrates.

Complementary to the aforementioned experiments, we present results from x-ray reflectivity studies using also a single solid supported lipid bilayer. Our investigations are carried out on non-functionalized solid supports made of conductive silicon to avoid further disturbance of the surface electrochemistry by additional coatings. These might influence the surface potential of the solid-

liquid interface - a fact, which can be expected to be less pronounced in our studies. In comparison to neutron studies the use of x-rays is supposed to yield higher resolution and consequently might increase the visibility of internal membrane structures and related thickness changes. The use of a single bilayer instead of a whole stack is motivated by the fact that it shows a much more homogeneous coverage when prepared on a solid support. Since a stack of more than thousand membranes will always have defects, an electric potential, which is applied to this stack, will consequently be perturbed [COVS05]. Experiments taking advantage of these experimental improvements and the results are presented in the following section.

3.5 X-ray reflectivity studies of the electric field effect
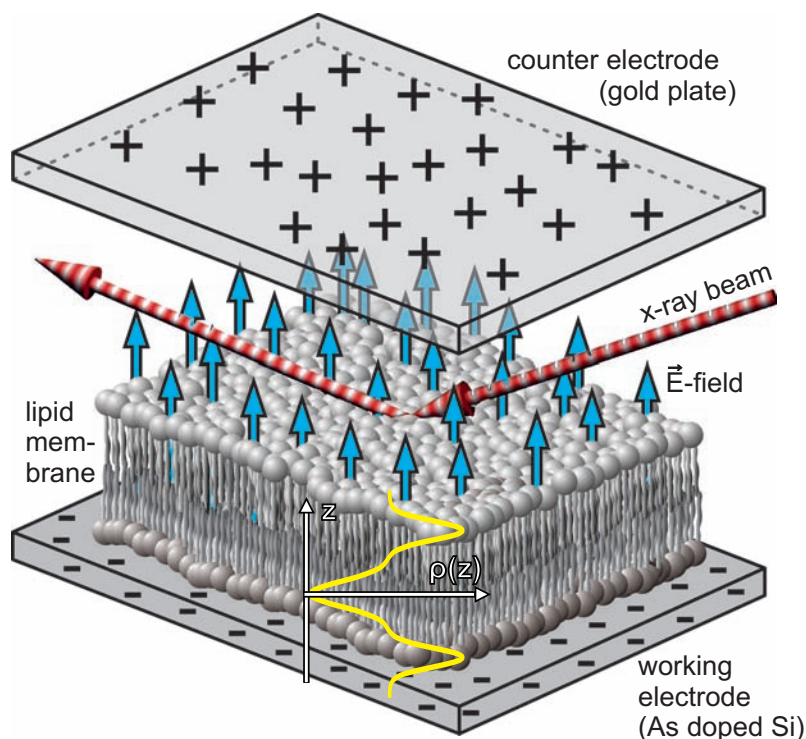
Figure 3.5: *Schematic representation of a solid supported membrane (SSM), which is used for the investigation of structural changes, i.e. the electron density profile $\rho(z)$, under the influence of an exciting external electric field. The membrane is supported by the working electrode, composed of an arsenic doped silicon substrate connected to a voltage generator. The counter electrode is placed in the lid of the chamber and faces the buffer solution. The reflectivity of the gracing incident x-ray beam is given by the electron density profile $\rho(z)$ perpendicular (z-direction) to the membrane.*

In this section we present results from x-ray reflectivity experiments performed on solid supported single bilayer membranes under the influence of externally applied electric fields. The nature of such effects has been discussed before (see chapter 3.4), so that the experimental part of the investigations will be the scope of this section. The technique of membrane reflectivity was introduced before

(see chapter 1.2) and its benefits and drawbacks were discussed. The combination of x-ray reflectivity and solid supported membranes is well established and offers the highest potential to resolve absolute thickness changes on the length scale of Angstroms [MMGK05, NGS06, GS07, Nov08, WMM+09, MCD10]. Furthermore, this type of model membrane system has shown to be well suited for the application of an electric field [BLH+04, BLH+05, LFC06, CLF08], while at the same time membrane structure is probed by a reflected neutron or x-ray beam. The solid support acts as the reference electrode and is countered by an electrode placed in the surrounding buffer solution. Figure 3.5 shows the principle of the measurements used to investigate the effect of external electric potentials on the structure of single lipid bilayers supported by a solid silicon substrate. For these studies the setup, which was used before in lipid multilayer experiments [COVS05], is slightly modified and will be described in chapter 4.3.

3.5.1 Layout of material science beamline (SLS)

Reflectivity experiments are performed at the surface diffraction station of the material science (MS) beamline at the Swiss Light Source (SLS, Paul-Scherrer-Institute; Villigen, Switzerland) (see figure 3.6). The photon energy is set to 19 keV by a double crystal Silicon-(111) monochromator (mono) with an energy resolution of $\frac{\Delta\lambda}{\lambda} = 1.4\cdot10^{-4}$. It is placed in the center of two focussing mirrors (not depicted), which are used in order reduce heatload of the wiggler generated beam and to reject the generated higher harmonics. After passing a set of primary slits (S1) the final beam size is defined by pairs of motorized secondary slits (S2) to 200 µm x 200 µm.
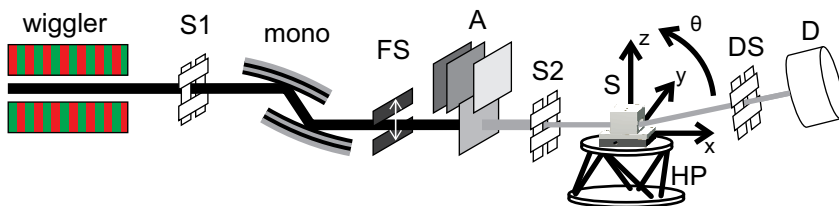
Figure 3.6: *Outline of the surface diffraction station at the Material Science beamline at the Swiss Light Source, as used for structure analysis experiments of SSMs in electric fields. See text for explanation of components.*

The sample (see section 4.3.1) is mounted in the horizontal plane on a hexapod (Physikinstrumente; Germany), which can be translated along and rotated around the x-y-z-axes. The parasitic photons, originating from air and water scattering, are blocked by a pair of detector slits (DS) mounted in front of the

detector (D). The reflected and scattered signal was recorded by a fast Pixel detector (Pilatus II 487 (v) x 195 (h) pixels (=95 kPixel)), with a pixel size of 172 μm in both directions. The dynamic range is 10^6 with a maximum count rate of 10^6 ph/s. The detector is located at a distance of 1140.80 mm behind the center of rotation (COR) of the sample goniometer. Automated absorbers (A) were used to extend the dynamic range in the measurements. A fast shutter system (FS) was used to reduce radiation damage by exposing the sample to the beam only during data accumulation and not during motor movements and waiting times.

3.5.2 Experimental setup for electric field application

The temperature circuit of the chamber (see chapter 4.3.1) is connected to a computer controlled heating bath (JULABO Labortechnik GmbH; Germany). The preparation of the SSMs is performed in the fluid phase of the lipid molecules (≥35°C). The electrodes inside the chamber are linked to a function generator (33120A, Agilent; CA, USA), which allows for the stepwise enhancement of potentials V_m inside the chamber ranging from -6 V to 6 V. In a membrane of 5 nm thickness these potentials correspond to electric field strengths of approximately $\pm 10^9$ V/m. The formation of the bilayer from the fusion of vesicles at the silicon surface was observed via a digital multimeter (ISO-tech IDM97; Southport, England) as an increase in the resistance and a decrease in the leakage current. The preparation procedure will be described in the materials and method chapter 4.3.2.

3.5.3 X-ray reflectivity measurements on supported membranes

At the beginning of the experiment the sample is aligned with respect to the impinging beam. The position of the sample is roughly determined by translating it through the beam in vertical direction. By a repeating series of tilt (θ) and translation (x-y-z) scans the membrane is positioned in the center of rotation of the goniometer (see figure 3.6), which coincides with the impinging x-ray beam. Due to the fact that a fast shutter system is used we can not work with automated attenuators. They rely on the determination of photon flux before the actual measurement is performed. As a consequence, each scan is split up into smaller intervals, of which each is carried out with a different attenuator. In the data processing these scans are merged again. By performing shorter scans with individual attenuator settings, we are able to reduce the radiation damage, which has shown to be essential in the degeneration process of the lipid bilayer and consequently for the reproducibility of the reflectivity scans. Biological tissue, e.g. lipid membranes, is known to generate free radicals on

the irradiation with x-rays. These radicals can induce conformational and chemical changes by breaking the molecular bonds and finally yield decomposition of the whole sample [CRC02, DRI$^+$07]. It is proposed that these damages can even continue after the x-ray irradiation is stopped. In comparison to free-standing lipid bilayers, where no effect of radiation damage was observed, the degeneration increases in the presence of a supporting solid substrate. To understand the underlying physics of such processes, experiments are planned to investigate the influences of x-ray irradiation on the surface potentials in dependence of the substrate´s electrochemical properties.

The count times and number of scan points inside the scanning intervals are carefully adjusted to an optimal compromise between signal-to-noise ratio and radiation damage. To further reduce the beam damage we shift the sample horizontally between two intervals. Seven to ten data points per interval are taken with count times ranging from 1 second up to 50 seconds. The scans are performed under specular condition, i.e. the impinging angle θ equals the angle, at which the reflected signal is detected. At each scan point an image, which covers an angular range of 4.198° in vertical and 1.681° in horizontal direction, is acquired. The detector is aligned in such way that the specular reflected beam is positioned at the central pixels. Subsequently the reflected and the respective offset scattering intensity at each angle needs to be extracted from the images.

3.5.4   Data treatment of reflectivity curves

The extraction of intensity values is performed in different steps using self-written MatLab scripts (version 2009b, Mathworks; MA, USA). The following functions can be found in the appendix A.2. At first the file *eval-config.m* needs to be modified by inserting the beamline specifications, data folders and the numbers of the interval scans, which need to be merged. Subsequently the function *main.m* is started and a selected image is used to define a region of interest (ROI) around the specular reflection. Next to this, two separate ROIs are defined. They are used to extract an averaged offset signal, which is subsequently used to correct the reflectivity signal. Finally, function *calc-refl-curve-merge.m* is executed to yield the one dimensional reflectivity curve $I(\theta)$. The angle θ is transformed into reciprocal dimensions of the momentum transfer q_z in units of Å^{-1} by using [AN01]

$$q_z = \frac{4\pi}{\lambda}\sin(\theta) \qquad (3.16)$$

For a detailed description of the scattering theory, which is used to calculate the reflectivity profiles of single bilayer membranes on a solid support, the reader is referred to [NGS06, GS07, Nov08]. The introduction of this theory would ex-

ceed the framework of this thesis and is not essential in the case of the under-lying results. The principle of x-ray reflectivity can be briefly and qualitatively described. An x-ray wave, which impinges on a flat silicon substrate in water, is reflected from the surface as long as the incident angle θ exceeds the spe-cific critical angle of the silicon-water interface. In the case of an additional film, which homogeneously covers the surface, parts of the incident wave will undergo internal reflections at the additional film-water and film-silicon inter-faces. Finally, the these parts exhibit a different phase shift according to the path they traveled between the two additional interfaces. Far away from the sample these waves will interact according to their accumulated phase shifts. Structures of constructive and destructive interference, i.e. increased and de-creased intensity, which are called Kiessig fringes, are consequently obtained at the detector. Geometrical considerations show that the thicker the film on the silicon surface becomes the more characteristic Kiessig fringes will show up in a fixed angular region. Thus the thickening of a film corresponds to a shift of the characteristic minima to smaller q_z values. In the following presenta-tion of experimental results we will restrict to the discussion of the positions of such characteristic minima in the reflectivity curves. Our discussion can con-sequently not distinguish between the thickness of the bilayer and the water layer, which is trapped between the bilayer and the silicon substrate. The given thickness values will always be a sum of both layers.

3.5.5   Results and Discussion

Figure 3.7 shows representative examples of reflectivity scans for two differ-ent lipid bilayers in externally applied electric fields on a conductive silicon support. In figure 3.7(a) the membrane is prepared from a lipid mixture com-posed of uncharged DOPC molecules and anionic DOPS molecules of molar ratio 4/1. Anionic lipids are added to see whether they might induce a pro-nounced change in the bilayer structure. The applied potentials are 0 V and -2 V. Note, that the sign of the applied voltages indicates the charge of the sup-porting electrode. The second graph in figure 3.7(b) shows the reflected in-tensity for a pure DOPC bilayer in an applied electric potential of -2 V and -4 V. In either (a) or (b) there is no significant, detectable shift in the minima of the Kiessig fringes, which is representative for all other observed reflectivi-ties. When fitting the first minima in (a) with a Gaussian function we obtain a value of q_z =0.22256(6) Å^{-1}, which corresponds to a real space layer thickness on top of the silicon of $d = \frac{2\pi}{q_z} = 28.231$ Å. For the potential V_m =-2 V we ob-tain q_z =0.22178(21) Å^{-1}, which gives a thickness of $d = 28.331$ Å. This is a film thickness change of 0.1 Å ($\equiv$0.35%) and thus is far below the values, which were observed to be about 40% by Burgess and colleagues [BLH+04, BLH+05].

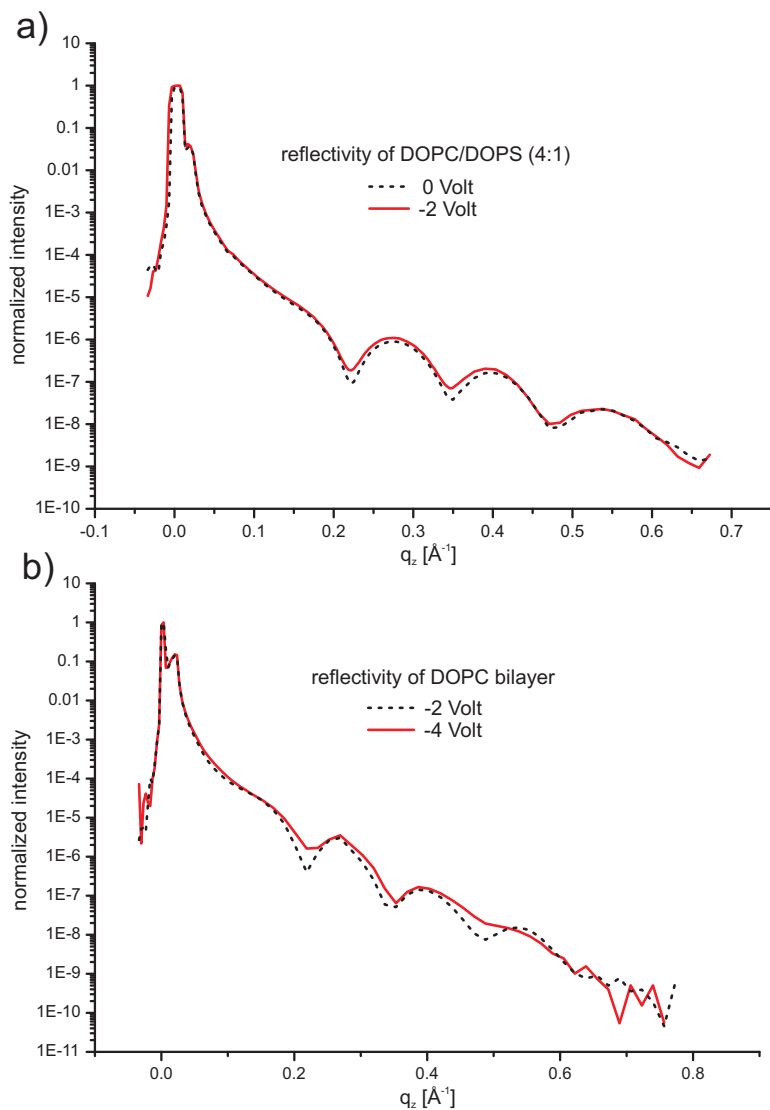**Figure 3.7:** *Reflectivity scans of two solid supported membranes, which are exposed to electric fields of variable strengths and composed of different types of lipids. No significant shift in the characteristic minima of the Kiessig fringes upon the application or change of the membrane potential is obtained. The shift in (b) occurs due to radiation damage and a slight unbinding of the film.*

Another influence on the obtained decrease of film thickness can originate from the translation of the sample between the two scans to reduce the effect of beam damage. We can not be sure that the sample has the same structure at every position across the substrate on the scale of such small thickness changes, which are below the absolute roughness of the silicon surface.

Figure 3.8 shows thickness values which are extracted from a reflectivity series at the position of the first minimum of a DPPC/DPPS (molar ratio 4/1) bilayer for a random variation of the transmembrane potential (see inset of figure 3.8). Randomness was chosen to avoid coincidence of shifts in the minima with shifts which are induced by beam damage. The latter always manifests in a continuous drift of the Kiessig fringes to higher q_z values and thus smaller layer thicknesses.
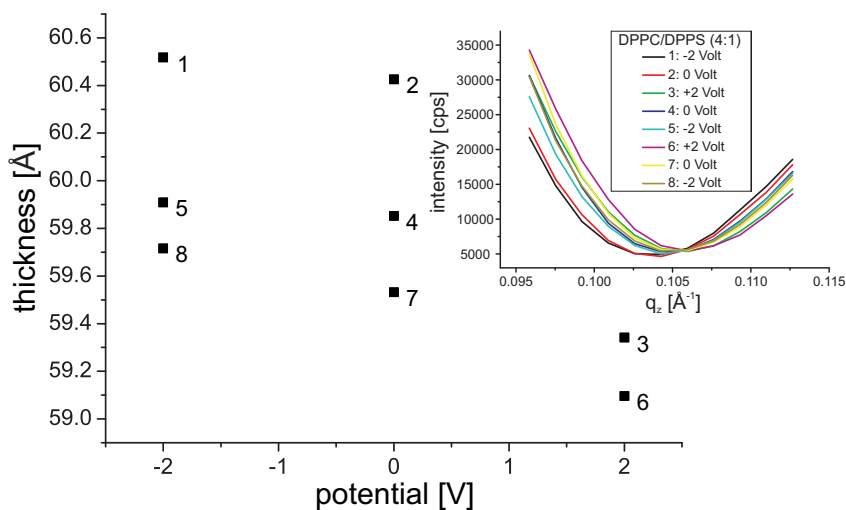
Figure 3.8: *Thickness values of a DPPC/DPPS (4/1) bilayer at varying transmembrane potentials. A slight decrease is obtained for more negative voltages but is much smaller to match the results observed by Burgess and colleagues [BLH+04, BLH+05]. The layer thicknesses show an overall tendency towards smaller values, which originates from the beam damage, i.e. degeneration of the sample.*

Note that the absolute thickness is remarkably increased in figure 3.8 compared to the experiments using DOPC or DOPC/DOPS lipids (see figure 3.7). This is due to the fact that DOPC is in the fluid phase at 35°C while DPPC and DPPS are in the gel phase, where their hydrocarbon chains are stretched. The graph

in figure 3.8 shows a representative slight increase of the membrane thickness for negative potentials and *vice versa* for higher potentials. The changes range from 0.5 Å to 1 Å (0.8% - 1.7%) and, thus, match the thickness behavior observed Burgess, but again on much smaller length scales. In contrast to the scans in figure 3.7 the scans in figure 3.8 are performed at a fixed position on the sample. Inhomogeneities in the layer thickness can thus be excluded to contribute to obtained variations. The position of the Gaussian fit to the scan minima in the inset of figure 3.8 can be determined with an error, which is a factor 10^4 smaller than the absolute q_z value of the Gaussian position. Note that errors of the reflectivity data are not yet included in the Gaussian fit. Theoretically a resolution below the maximum obtained q_z value can be achieved [WW91] by the precise determination of the position of characteristic features in the experimental data. Fitting higher order minima would be even more accurate in this case since the shift increases at higher q_z values. Another improvement might be achieved by determination of the membrane thickness in a full q_z-range fit but this requires data from larger scan ranges. In that case the effects of beam damage become relevant because at the same time the irradiation time is extended the degeneration of the sample increases and the Kiessig fringes will become less pronounced from scan to scan. This will increase the signal-to-noise ratio and consequently reduce the fit accuracy. The experiments show that two scans, which are performed at the same sample position and cover the whole scan range up to q_z =0.6 Å^{-1}, can not be compared as the state of chemical degradation is already to pronounced after the first measurement. The numbers next to the data points in figure 3.8 indicate the order, in which the reflectivity scans are performed. It can be seen that the beam damage shows up as a continuous decay of membrane thickness with increasing scan number. An explanation for the molecular processes cannot be given but it has to be pointed out that the thickness change, which is related to the electric field, dominates the effects of beam damage.

The process of electric field unbinding when reaching field strengths above $5 \cdot 10^8$ V/m was predicted in section 3.4. Figure 3.9 shows a representative behavior of bilayers made of DOPC lipids when the electric field is raised. When the layer on top of the silicon detaches the characteristic features in the graph disappear and the reflectivity of a pure silicon water interface is obtained. The stepwise detaching of the membrane from the surface can be seen in figure 3.9(a). Assuming a layer thickness, which is obtained from the scans in figure 3.7, the applied transmembrane potential corresponds to a field strength of about $6 \cdot 10^8$ V/m. The introduction of the field unbinding of the membrane at this value in perfect agreement to the values reported by Charitat and Burgess [BLH$^+$04, BLH$^+$05, LFC06, CLF08].

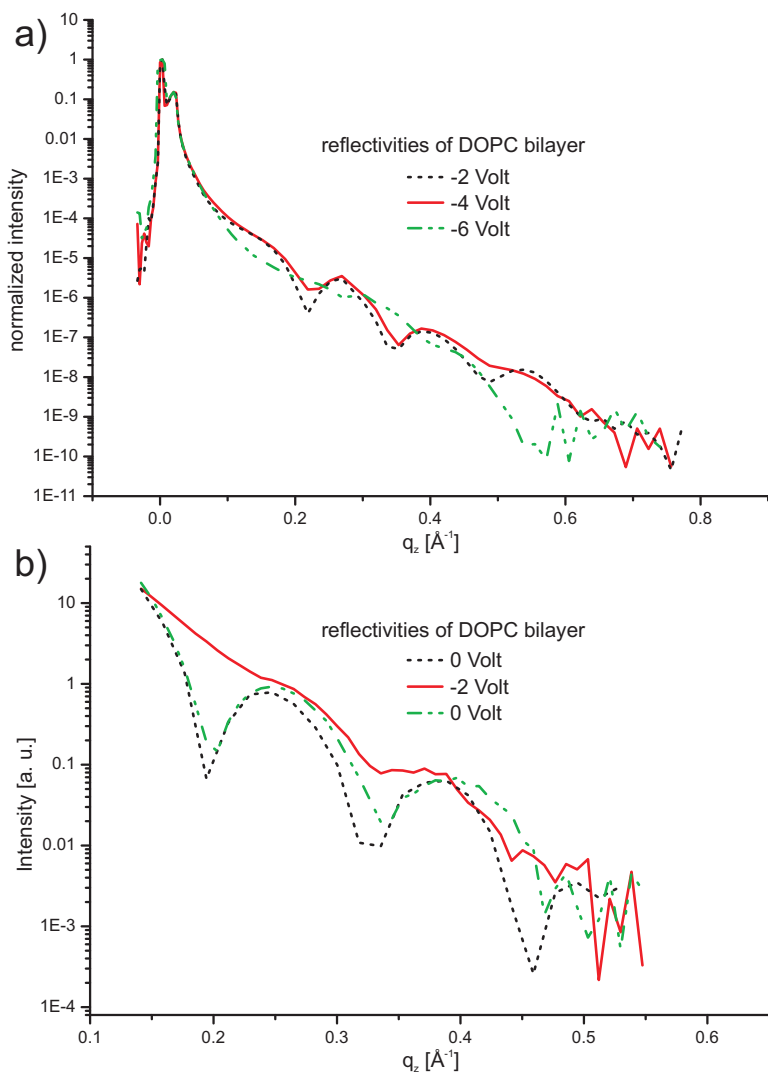***Figure 3.9:*** *The reflectivities in (a) and (b) show the unbinding of membranes when the electric fields reach values above* $6 \cdot 10^8$ *V/m. b) This effect shows to be reversible since the bilayer signal is detected again after the applied electric field is switched off.*

In figure 3.9(b) it is shown that the process of unbinding is reversible and the membrane attaches back to the substrate when the applied field is removed. Upon further increase of the electric field electrolytic processes at the substrate surface occur and irreversibly destroy the membrane. Summarizing the presented results a clear statement about changes in the layer thickness on the silicon under the influence of an external electric field can hardly be made. The observed effects are much smaller than predicted [BLH$^+$04, BLH$^+$05] and appear on length scales, which are comparable to the maximum achievable resolution. A potential explanation for the large differences between the results of Burgess and the ones we have obtained might be the presence of the gold coating on the supporting electrode they used. The substrates in our experiments have a specific resistance of $10^{-2}\,\Omega$cm. This is four orders of magnitude higher than for gold, which has a specific resistance of $2.2 \cdot 10^{-6}\,\Omega$cm and might lead to a completely different electrochemistry of the surfaces in the two experiments. Consequently, we can think of an enhancement of the field effect and thus an increase in the obtained structural changes in the presence of gold on the membrane supporting substrate as it was used by Burgess and colleagues. Due to these potential influences and the obtained results we can finally give two reasons why the investigations of structural changes of lipid membranes in electric fields should be carried out in the absence of solid substrates. The first and more general one is motivated by the omnipresent beam damage, which occurs in every measurement and is up to now rather unexplored. The lack of information about the molecular processes, which occur upon beam damage, might result in distinct uncertainties of the obtained membrane structure properties. The authors of reference [CRC02] have shown that small molecular residues, which result from the chemical breakdown of the lipid, can be determined in thin-layer chromatograms. In addition to this, a second reason is the lack of knowledge about the electrochemical transformations and generation of electric potentials in applied electric fields on the molecular dimensions at the substrate surface. These obviously influence the bilayer since they can drive its unbinding from the supporting substrate. In a freestanding membrane system this additional influence will not occur and intermediate states between the intact and the broken or degenerated membrane are very unlikely. Obviously the absence of a supporting substrate will simplify the investigation of potential structural or topological changes, since in high electric fields a freestanding membrane can only undergo electroporation, which finally might lead to the disruption of the film. The inconsistency of the results obtained from solid supported membranes in electric fields shows the necessity of an experimental method which allows for the investigation of structural changes in controlled electrochemical conditions.

4 Materials and preparation techniques

The following section will include a description of the micro-machining and structuring techniques of substrates which are used for the reconstitution of the presented model membrane systems. The techniques, which are used to prepare BLMs and Solid Supported Membranes (SSM) have been previously published by our group [BWZ⁺08, NGS06]. A more detailed description of the preparation of BLMs in microfluidic devices will be given, since this type of membrane system has been used for the first time in combination with synchrotron experiments.

4.1 Black Lipid Membranes (BLMs)

4.1.1 Substrate properties and micro-structuring

From the results of previous works [Bee06] we have seen that geometry of the aperture and the material of which the membrane supporting substrate is fabricated are essential. For use in x-ray experiments the membrane has to be very stable, because the experiments are carried out in a closed room with restricted access during the irradiation of the sample with x-rays. Furthermore, the experiments can last up to several hours, depending on the type of investigation. There are two factors which will mainly influence the stability of a BLM. The geometry of the aperture and microscopic topology of its rim. If the rim is smooth it favors the assembly of lipids at the edge of the aperture on a microscopic scale and long lifetimes can be obtained. The geometry is of importance for the studies using bulged BLMs in transmitted x-rays. Our theoretical model, which is used to describe the image formation, assumes rotational symmetry of the bulged membrane. Consequently, the imaging experiments have to be carried out on circular shaped apertures, which also have the advantage that the interfacial tension and related stresses in the membrane are minimized. The material of the supporting substrate has to be stable enough to not bend under its own weight, or in the presence of applied hydrostatic pressures. At the same time it needs to be "functionalizable" to finally promote the right orientation of the amphiphilic lipids at its surface. Depending on the membrane system which is used, we choose either silicon or Teflon as a support for the lipid bilayers. The following sections will mainly summarize the procedures used to fabricate substrates containing an aperture for the reconstitution of painted BLMs [MRTW62b]. The preparation of conductive supports for solid supported membranes is described in section 4.3.

4.1.2   Silicon etched apertures / PECVD coating

A detailed description of the structuring of silicon wafers by a wet etching technique can be found in [BWZ$^+$08, Bee06, Med94, Pan99]. For the studies of BLMs with hard x-rays, silicon substrates of thicknesses ranging from 200 μm to 650 μm (Crystec GmbH; Berlin, Germany) are used to avoid any bending of the supports during the preparation. In contrast to the previous silanization of the silicon to realize a hydrophobic surface, these wafers are coated by means of **P**lasma-**E**nhanced **C**hemical **V**apor **D**eposition (Oxford PlasmaLab). To avoid leakage currents across the silicon substrates they are first insulated by the deposition of a 100 nm thick layer of SiO on both surfaces[3]. Subsequently, the device is cooled down to room temperature and the deposition of a 100 nm layer of Teflon is performed[4]. The surface hydrophobicity is checked by a qualitative contact angle measurement of a water droplet on the coated silicon surface. The contact angle changes from 20°-30° on the pure silicon surface to more than 120° after the coating process. This large increase is an indicator for the strong hydrophobizing effect of the Teflon coating. Compared to the OTS (silane) used previously, the contact angle change is increased by about 20%.

4.1.3   Focused ion beam structured Teflon foils

As well as using silicon substrates, we also perform experiments using the classical preparation based on the painting of an organic solvent across an aperture in a thin Teflon foil (25 μm, Dalau; Germany). An improvement of the common techniques, which use either hot needles or spark erosion to create holes in Teflon foils [MRTW62b, MM72, HWSG04], is achieved by means of focused ion beam (FIB) milling [BWZ$^+$08]. Based on previous preparations in literature [WE04a, WAP$^+$06, QCR$^+$07] we have developed a technique to create apertures with a smoothness on the nanometer scale and membrane lifetimes up to 60 hours can be obtained. This technique also enables the fabrication of varying geometries with very high precision and diameters ranging from micrometers up to several millimeters [Bee06, BWZ$^+$08].

4.1.4   Preparation of Black Lipid Membranes

The preparation of planar free-standing, solvent-containing lipid membranes goes back to the work of Müller and Rudin [MRTW62b, MRTW62a]. The remaining organic solvent in this kind of reconstituted membranes might be con-

---

[3]Process parameters are: **gas flux**: 5%SiH$_4$ →170 sccm, N$_2$O→710 sccm, N$_2$ →162 sccm; **pressure**: 1 Torr; **HF power**: 20 W; **temperature**: 300 °C ⇒ Deposition rate: 1 $\frac{nm}{s}$.

[4]Corresponding parameters are: **gas flux**: C$_4$F$_8$ →250 sccm; **pressure**: 100 mTorr; **HF power**: 200 W; **temperature**: 20 °C ⇒ Deposition rate: 0.5 $\frac{nm}{s}$.

sidered problematic and was already discussed in chapter 2. However, the preparation is very fast and yields more stable bilayers compared to the preparation of Montal and Müller [MM72] (see chapter 2.4). Therefore, we have mainly used this approach in our initial study of BLMs in synchrotron beams. In detail, the membranes were prepared as described in [Hil04, BWZ$^+$08]. Teflon foils (section 4.1.3) and "functionalized" silicon substrates (section 4.1.2) are homogeneously pre-treated with Loctite Primer 770 (Henkel; Germany), which has an additional hydrophobizing effect on the surface. Afterwards the substrates are glued to a Teflon wall dividing two compartments inside the experimental chamber (see figure 4.1) using Loctite 406 (Henkel; Germany). A solution
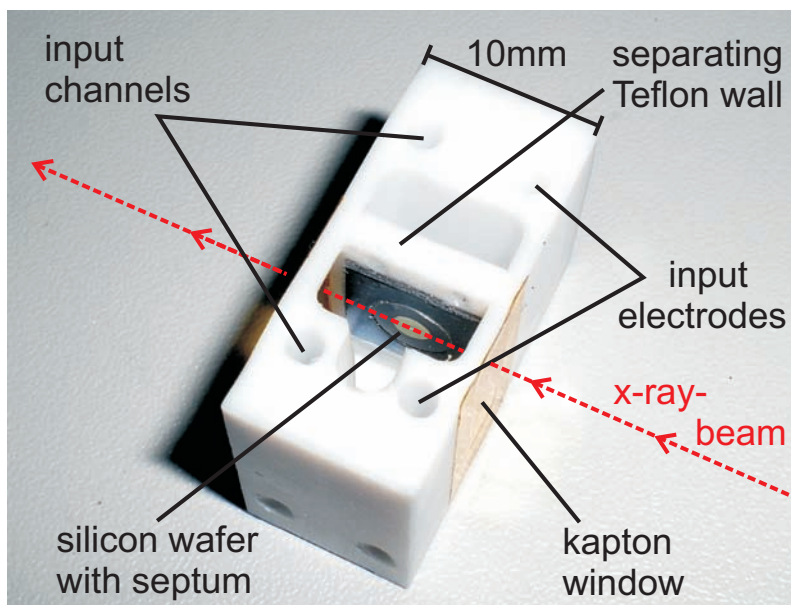

Figure 4.1: *Image of chamber for BLM imaging. The structured silicon substrate / Teflon foil is glued to the Teflon wall separating two aqueous compartments. Hydrostatic pressure and electric potentials across the membrane are controlled via two holes for tubings and electrodes connected to each compartment.*

of the phospholipid diphytanoylphosphatidylcholine (DPhyPC, Avanti Lipids; Alabaster, USA) dissolved in methanol (10 mg/mL) is painted across the substrate surface, using a thinned, natural hair paintbrush. This serves as an additional anchor layer for the final membrane; inhomogeneous lipid layers are

formed at the surface as the solvent evaporates. Subsequently the chamber is filled with buffer solution (100 mM KCl, 5 mM MgCl$_2$, 5 mM Hepes, pH 7.0 KOH). The membrane is "painted" with another paint brush from a lipid solution (DPhyPC/decane, 20 mg/mL). The membrane capacitance is recorded with a modified Port-a-Patch NPC-1 system (Nanion; Germany), equipped with an EPC-10 amplifier (HEKA; Germany), according to the methods introduced in chapter 3.2. The signal is transduced into both compartments of the measurement chamber by Ag/AgCl-electrodes (see figure 4.1). The membrane immediately starts to thin as described in chapter 2 and shown in figure 2.5. After approximately 15 minutes, depending on the amount of solvent initially present in the membrane, a pure lipid bilayer remains and shows a characteristic charging and discharging peak in the current response[5]. Subsequently, the specific capacitance c_m can be calculated, as was described in chapter 3.2. A BLM on a 200 μm hole gives a typical capacitance value of 150 pF corresponding to $c_m = 0.48 \frac{\mu F}{cm^2}$, which is in perfect agreement with [TOL00]. For the synchrotron experiments an additional shielding around the chamber was mounted to the sample stage to suppress electrical noise originating from various sources in the experimental hutch at the beamlines.

Besides x-ray structure analysis, which is our main objective, these very stable membranes have also been characterized by static / dynamic light scattering (DLS), conductance measurements, and fluorescence recovery after photobleaching (FRAP) [Bee06].

4.2 MicroFluidic Black Lipid Membranes (mfBLMs)

As an alternative to Black Lipid Membranes, we also used a recently developed system for reconstituted lipid bilayers. These are prepared in microfluidic devices and are called microfluidic Black Lipid Membranes (mfBLMs) [FST06, HNB07, OTST08]. Briefly, they are prepared in a crossed channel microfluidic device, where two monolayers of surfactant molecules, assembled at the interface of an oil and water reservoir, are brought into contact to form a bilayer membrane (see figure 4.2). The motivation to use mfBLMs originates from them having several advantages:

Geometry - As the phase contrast signal increases proportionally to the path length L of the x-rays in the sample, the mfBLMs offer an improved geometry for imaging experiments. L is in the range of a few micrometers in the case of a thin, bulged BLM. The diameter of a mfBLM can equal the depth of the channel when it spans it fully. Consequently, the penetration depth

---

[5]It was shown that the final BLM thickness is independent of the organic solvent, which is used to prepare the lipid solution [TH66a].

becomes a few hundred micrometers assuming a planar orientation, i.e. no curvature, of the film. Experimentally this can be achieved when the pressure difference across the membrane vanishes and the membrane has reached a stable position in the channel.

Preparation - mfBLMs enable a fully automated preparation, that enables performing the membrane formation via computer controlled, motorized pumps. Since in synchrotron experiments access to the experimental setup is restricted the beam does not have to be stopped for a new preparation every time, as in the case of common BLMs.

Reproducibility - The latter fact also gives the advantage of a high reproducibility. Whenever the membrane ruptures the chamber is flushed with new, fresh material (lipids, solvent, and buffer) and a new bilayer can immediately be formed, which takes less than a minute in time.

Electric excitation - Electrodes can be placed in the water channels (see figure 4.3), and electric potentials can be applied across the two monolayers sensing the distance and the bilayer formation dynamics (see chapter 2.2).
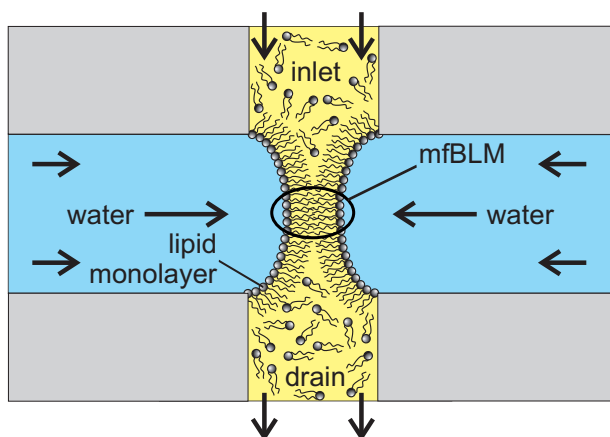

Figure 4.2: *Schematic representation of the microfluidic BLM (mfBLM) setup, which are prepared in a microfluidic device. Two water reservoirs (horizontal channel) are exposed to a lipid-solvent solution (vertical channel). The amphiphilic lipid molecules assemble at the water-solvent interface to form a monolayer. The application of motorized pumps enables the controlled approaching of the monolayers to form the mfBLM.*

Nevertheless, these reconstituted membranes also show the drawback that the Plateau Gibbs border (PGB), surrounding the membrane patch, will always be in the path of the x-rays. Due to the strong diffractive index contrast between the water and the PGB it is likely to give an additional contribution to the diffraction pattern (see chapter 7). This is not the case for the bulged interface of the normal BLMs.

4.2.1 Experimental setup for mfBLMs

The following section provides a detailed description of the single steps that were performed to prepare microfluidic devices according to the protocols in [OKS$^+$05, DEKP07] followed by the reconstitution process of mfBLMs [FST06, HNB07][6].
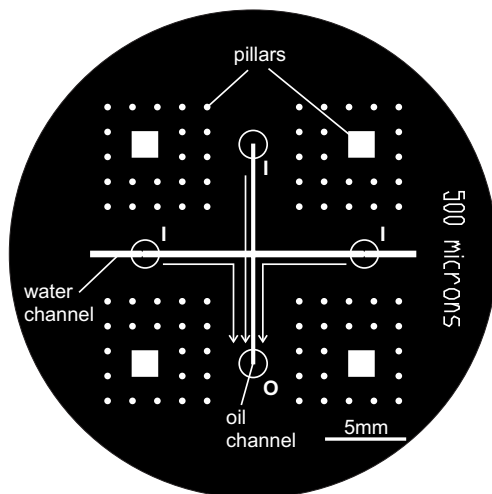
4.2.2 MF channel design

Figure 4.3: *Drawing of the illumination mask that was used for the fabrication of the microfluidic devices. In regions (white) where channels (oil and water) and pillars are located the photo resist will be exposed.*

---

[6]MF channel design and preparation was worked out in a cooperation together with Shashi Thutupalli, PhD student in the group of Prof. S. Herminghaus at the Max-Planck-Institute for Dynamics and Self Organization in Göttingen.

The masks (see figure 4.3) are designed with AutoCAD (Autodesk GmbH, Germany) and printed by JD Photo-Tools (Oldham, UK). The design is described as follows: The 3 inlets (I) are connected to the syringes and the remaining outlet (O) is used as a drain for all solutions. The water channel, which is mounted in a horizontal orientation, is prepared in different widths of 300 μm, 500 μm or 1 mm. The oil / lipid solution channel always has a width of 250 μm (500 μm for 1 mm water channels). The pillars (square and circular shaped) will provide a constant height at every position of the chip when a stamp is put on top in the final copying procedure. Furthermore, they will act as adhesion points for capillary flow between master and stamp. For a detailed explanation see the next section. The electrodes for electrophysiological measurements can be introduced into the thicker part, at the end of the water channels. Length of all channels is 20 mm. The lateral dimensions are adapted to the geometry of the experimental setup of the beamlines - ID22 at ESRF (see chapter 6.1.2).

4.2.3   MF channel fabrication

The following steps are carried out in a clean room (class 100) to avoid contamination of substrates and photolithographic resists with dust. As a substrate we used polished silicon 111 wafers provided by Crystec GmbH (Berlin, Germany) of 50 mm diameter and 200 μm thickness.

Cleaning - The polished side of the silicon wafers is cleaned with acetone and isopropanol and finally blow dried under nitrogen gas flow. To fully evaporate the solvents the substrates are put on a heating plate for 10 minutes at 200°C.

Photo resist coating - The silicon wafers are placed on a spin coater OptiSpin SB20 (Sister Semiconductor Equipment (SSE); Singen, Germany) and 3 mL of a highly viscous photo resist SU-8 100 (MicroChem; Newton, USA) are poured and spread on the surface. The different settings that have been worked out for the respective heights of the final channels are shown in the following table[7]:

---

[7]The height of the channels should be equal to their width to end up with a square shape that will promote the formation of rotationally symmetric bilayer patches.

thickness [μm]	acceleration [rpm/s]	acc. time [s]	RPM	spinning time [s]
100	300	3	1500	60
200	300	3	1200	30
300	200	5	1000	30
500	200	5	750	60
> 1000	100	10	750	30

For very large film thicknesses the silicon must be homogeneously covered with photo resist before the spin coating procedure starts. A scalpel is used to burst bubbles that are included in the resist.

Prebake - The coated wafer is placed on a hot plate at 65°C and baked for $\frac{\text{thickness}}{5}$ seconds. The resist gets more fluid, the film relaxes, and defects from the coating procedure vanish.

Softbake - This baking procedure is used to fully evaporate the solvent included in the photo resist. The temperature of the previous step is raised from 65°C to 95°C and is kept for $\frac{\text{thickness}}{100}$ hours on the hot plate. It has been shown that this strategy works best but one still has to take care that most of the Bernard-structures, originating from the convection of different components in the resist, have disappeared.

Exposure - After removing the samples from the hot plate they are cooled down and positioned inside a MJB4 Mask Aligner (Karl SÜSS Microtec AG; Garching, Germany). Subsequently, the mask is aligned concentrically with respect to the silicon wafer. Exposure is performed at 365 nm (Channel 2) with an intensity of 17 mW/cm^2 and a continuous lamp power of 230 W in vacuum contact. $\frac{\text{thickness}}{50}$ cycles of 15 s duration are run interspersed with 60 s breaks to avoid an increase of internal tension in the resist layer.

Postbake - Subsequently, the silicon wafer is heated for 1 minute at 65°C and directly moved to a hot plate of 95°C to be kept there for 20 minutes.

Develop - After cooling down the sample is placed in a beaker filled with photo resist developer mr-Dev 600 (Micro Resist Technology GmbH; Berlin, Germany). To provide sufficient solution exchange the beaker is mounted on a laboratory shaker. It takes about 20 minutes until the remaining, unexposed resist is fully dissolved.

Cleaning - The microfluidic chip (master) (see figure 4.4) is taken out and im-
mediately rinsed with acetone for approximately 1 minute, followed by
intensive washing with isopropanol and drying under a nitrogen stream.

Hardbake (optional) - There is the option to hardbake the chip afterwards for
approximately 1 hour at 200°C. This is supposed to crosslink the materi-
als, but was also found to simultaneously induce stress in the structures
making them more fragile. In some cases detachment from the silicon
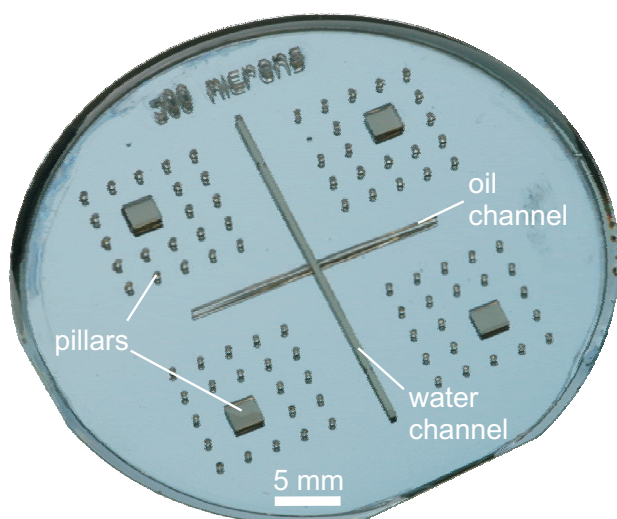surface may occur.

Figure 4.4: *Photograph of microfluidic master composed of SU8-100 chan-
nel structures on a 2 inch silicon wafer. It is used to produce copies of UV
glue and PDMS (poly(dimethylsiloxane)) for the microfluidic device. Chip
design according to figure 4.3.*

Subsequently, the SU8-coated silicon masters, which are considered as a posi-
tive of the channel structure, are used to produce positive and negative copies
made from PDMS (polydimethylsiloxane) and UV curable glue [KP10]. First,
the master is cleaned with Isopropanol and blow dried. Both steps used to cre-
ate either positive or negative copies are described separately in the following
sections. Due to the large height of the SU8 structures there is a risk of the chan-
nel breaking or detaching from the silicon wafer when a direct copy is made in a
single step. Therefore, a highly reproducible technique was developed consist-

ing of three steps that saves the SU8 masters, bearing in mind their laborious production:
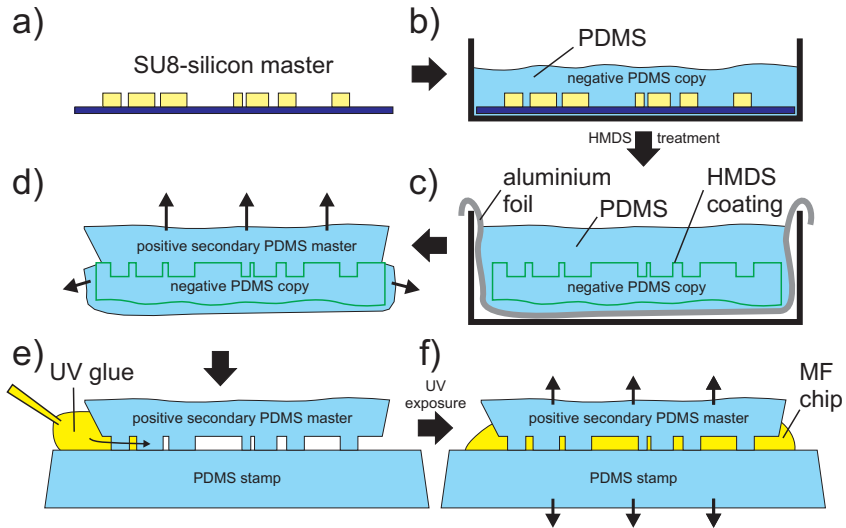

Figure 4.5: *To protect the SU8 masters (a) a three step copying technique is used for the microfluidic chip production. After preparing a negative PDMS copy of the channel structure (b) its surface is treated with HMDS and a secondary (positive) PDMS master is taken (c). This secondary master is separated from the surrounding PDMS (d) and placed on a flat PDMS stamp (e). The spaces in between are filled with UV curable glue and after 5 to 10 minutes of UV light exposure the microfluidic chip can be peeled off (f).*

Direct / single step copy (PDMS, UV glue):

This procedure is used to create a direct negative copy of the SU8 silicon master with either PDMS (Sylgard 184 Silicon Elastomer Kit (Sasco Holz GmbH; Dreieich, Germany)) or NOA81 (Norland Optical Adhesive No. 81, Edmund Optics; Karlsruhe, Germany), a fast curing UV glue, that finally acts as the microfluidic device. This glue is used due to its transparency, weak x-rays scattering properties and its stiffness after intense curing (compared to PDMS). In comparison to PDMS it cannot be "functionalized" in a plasma cleaner and covalently bound to other silicon containing materials, which is a disadvantage. Furthermore, it dewets on all hydrophilic surfaces so that it can hardly be spread homogeneously without tools such as a stamp.

$500\,\mu L$ (for every $300\,\mu m$ height of the channels) PDMS solution (10:1 (m:m)

ratio of PDMS and crosslinker[8]) is spread on the master and a razor blade is used to create a flat liquid film of homogeneous height and remove the surplus material. After heat-curing for 1 h or more at 85°C, the thin MF-chip can be removed carefully from the silicon surface.

When using the UV glue the same amount as above is poured onto the silicon master, but a stamp is used to spread the solution across the surface. The stamp is a flat PDMS piece that is pushed on the SU8 to prevent any glue from flowing above the channels so that they are open from both sides in the final chamber. Master, glue and stamp are then put under a UV lamp PolyluxPT (Dreve; Unna, Germany) and exposed with UVA (355 nm) light for about 5 to 10 minutes[9]. The chip is then carefully peeled of the silicon master by continuously adding Isopropanol to not destroy the SU8 structures.

Three step copies (UV glue):

In this procedure (see figure 4.5) a positive PDMS master is created that is used to prepare MF chips of UV glue in large amount. The silicon master (figure 4.5(a)) is placed in a Petri dish and the PDMS-crosslinker solution poured in (figure 4.5(b)). Degassing is performed in a vacuum chamber to get rid of the air that is trapped underneath the silicon wafer. Subsequently, the PDMS is cured at 85°C for 1 h or more and then a scalpel is used to cut out the negative copy. This part is put in a sealed glass beaker, together with a vial filled with **h**exa**m**ethyl**dis**ilazane (HMDS, Fluka; Germany), for approximately 15 minutes. The negative PDMS copy is placed in a Petri dish lined with aluminium foil and PDMS solution is poured onto it (figure 4.5(c)). After curing the PDMS, as described previously, everything is peeled of the aluminium foil and both PDMS parts are separated by cutting with a scalpel - leaving the negative copy and a positive secondary master of PDMS (figure 4.5(d)). The latter one is cut in a way that smooth edges are left and is subsequently laid on top of a very flat stamp of PDMS (figure 4.5(e)). At the position of the oil channels a drop of UV glue is applied that crawls towards the cross by capillary forces. Glue is added for as long as the whole space between PDMS master and stamp is filled and no air bubble is left. The UV glue is exposed, as described above, for 5 to 10 minutes and the final MF chip is carefully peeled of the PDMS by adding Isopropanol (figure 4.5(f))[10].

As an alternative to the aforementioned microfluidic devices, which are fabricated by means of photolithography, we use a stainless steel device of 300 µm

---

[8]Both parts are intensively mixed and subsequently degassed in a vacuum chamber to avoid leaving any bubbles in the mixture.

[9]depending on the required stiffness of the MF chip

[10]The advantage of this technique is the high amount of microfluidic devices that can be prepared without using the original masters anymore. If a secondary master breaks it can be easily reproduced from the negative copies again.

thickness. This only includes the oil and water channels and is machined according to the mask dimensions in figure 4.3. These devices have the advantage that they are inert, very robust and can be used several times. The steps of BLM preparation, which are described in the next section, are identical for every type of microfluidic device material.

4.2.4 Preparation of mfBLMs

The previously described microfluidic chips can now be used for mfBLM formation. Different window materials, e.g. Polypropylene, Polyimide (kapton), silicon nitride, Ultralene, etc., can be chosen. However, to simplify matters a self-adhesive kapton foil (Dr. D. Müller GmbH; Ahlhorn, Germany) of 25 μm thickness is used. The MF chip is placed on the window material, which is subsequently cut to fit the size of the chip. Nanoports N333 (10-32 for 1/16" tubing, BESTA-Technik GmbH; Wilhelmsfeld, Germany) are glued to the kapton at the end of the channels. Drying is at 120°C for 1 h with the application of weight pressure. The sealed hole is widely opened with a hot needle to avoid blockage of the channels. Now the second window is bound to the other side of the MF chip. PTFE tubing (Novodirect; Kehl, Germany) with inner and outer diameter of 0.5 mm and 1.6 mm runs in the fitting (F333) and the ferrule (F142) and is connected to the fixed Nanoport (see figure 4.6(c)).
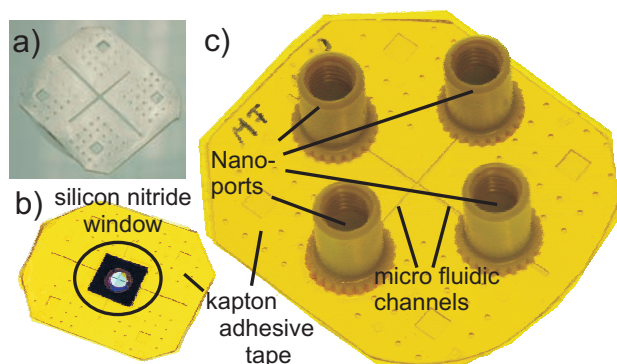

Figure 4.6: *The photograph shows (a) the UV glue microfluidic chip after it is cured. (b) The window material, here a 150 nm silicon nitride window, is placed at the channel cross and the device is sealed with self-adhesive kapton tape. (c) Nanoports are glued at the channel entrances for application of tubings and syringes. The microfluidic devices which were made from eroded metal plates are not depicted.*

At the other end of the tubings a Hamilton syringe (Schütt; Germany) is connected. Volumes of 0.5 mL or 1 mL for aqueous buffer and 0.25 mL or 0.5 mL for the lipid solutions are used. Deionized and distilled water (MilliQ (MQ), Millipore; Germany) or buffer solutions with 150 mM NaCl (pH=7) is used for the preparation. The oil solutions consist of either DPhyPC in n-decane (see BLM formation) or Monoolein (Avanti Lipids; Alabaster, USA) in Squalene (Merk; Germany), both at a concentration of 10 mg/mL. The syringes are mounted onto a self-made pump system that is controlled by a LabView GUI (National Instruments) allowing injection speeds to be precisely controlled, up to speeds of 500 μL/h.
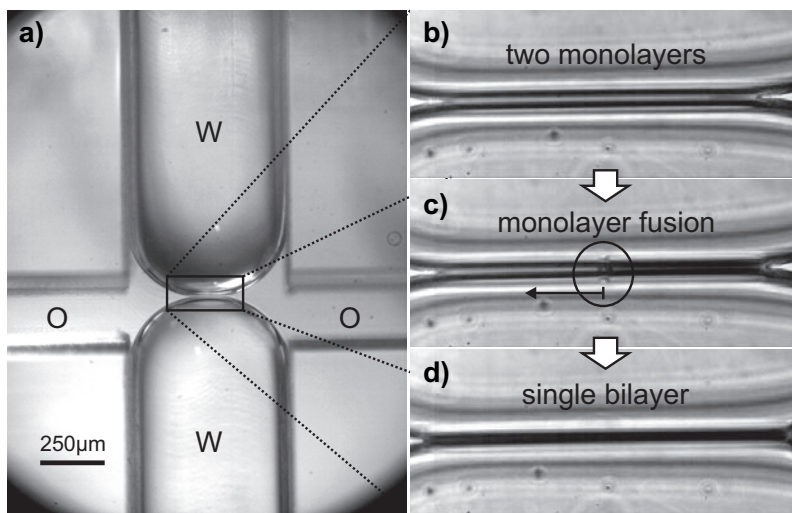

Figure 4.7: *Formation of a mfBLM in a microfluidic device. a) Bright field microscopy image of two "water fingers" (W). They are exposed to a oily squalene-Monoolein solution (O) and brought into contact at the channel crossing. Phase contrast light microscopy series: b) Zoom-in of the approaching monolayers. c) Local instabilities initiate the monolayer fusion until a bimolecular membrane (mfBLM) is left (d).*

The membranes are prepared by running the oil pump for approximately 10 minutes to flush the channels with the lipid solution. This procedure has an additional hydrophobizing effect helping to promote the formation of convex water interfaces (also called "water fingers" (see figure 4.7(a)). Subsequently, the oil flow is stopped and the water fingers are slowly brought into contact in

the channel cross region[11]. When the two monolayers are brought together, intense Fresnel fringes appear in the visible light microscope (figure 4.7(b)). Due to a stochastic instability the monolayers suddenly fuse, the surrounding oil is expelled to the Plateau-Gibbs border and the Black Lipid Membrane forms as described previously (figure 4.7(c)). The size of the bilayer patch can be controlled by variation of the pressure in the water channels. The presence of a single bilayer can be checked by capacitance measurements or by comparison of the fresnel fringes in the regions of the two monolayers and the single bilayer (see figure 4.7(c,d)).

4.3   Solid Supported Membranes (SSMs)

4.3.1   Substrates and electric field chamber

The conductive silicon (1 0 0) substrates that were used to prepare the bilayers are ordered from Crystec GmbH (Berlin, Germany). They are 1 mm thick and have a specific resistance of $0.01\,\Omega$cm - $0.015\,\Omega$cm, depending on the n-type doping of the crystals with Arsenic. In references [BLH$^+$04, BLH$^+$05, LFC06, CLF08] the authors have used gold coated supports as a working electrode. To avoid the influence of additional unknowns (such as thickness, roughness and electron density of such a layer) in the final electron density profile reconstruction we wanted to keep the system as simple as possible and avoid working with anything other than the bare semiconductor crystal. The substrates that are used for the preparation are cut into pieces of 10 mm x 15 mm to fit in the chamber. To make sure that no leakage currents flow somewhere rather than across the membrane, the back side of the silicon wafer is coated with 300 nm of SiO and protected with a mask, at the position where the substrate is connected to the voltage generator[12].

The chamber (see figure 4.8) consists of a base plate (BP) that includes a stainless steel pin (S) linking the voltage generator to the conductive silicon substrate. A gold plate (G) acting as counter electrode is located in the lid (L) of the chamber and can be contacted from the outside. The whole chamber is made of Polymethylmethacrylat (PMMA). Two windows are machined into the upper part and sealed with 25 μm kapton foil (K). Next to the hole for the counter electrode there is an in- and outlet for buffer exchange and rinsing of the chamber (I). The hole chamber is temperature controlled by a heating "jacket" and base plate (H).

---

[11]Depending on the surfactant it may be necessary to wait for some time and let the molecules assemble at the oil-water interface to form a dense monolayer that will subsequently allow for the formation of a stable bilayer.

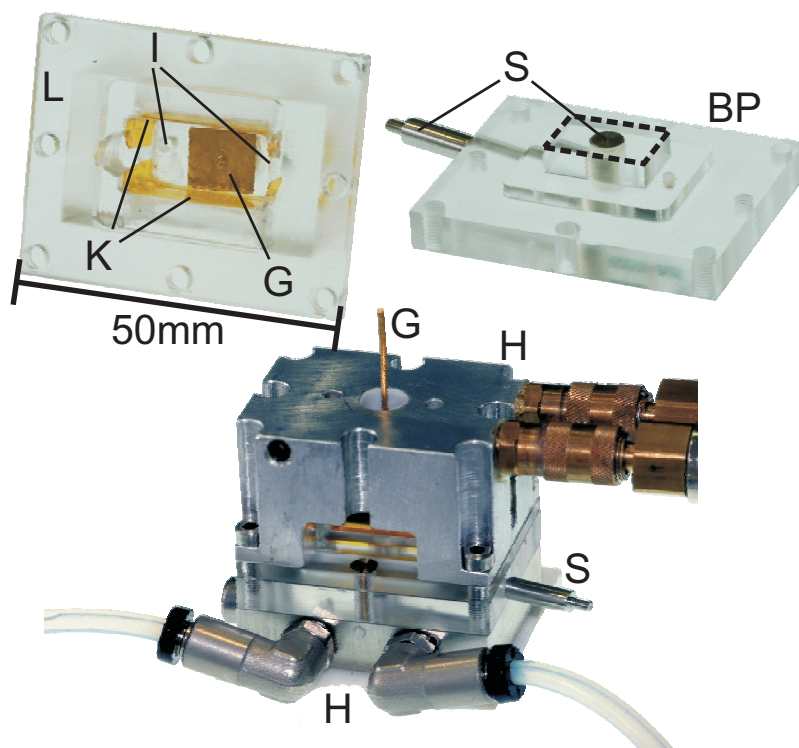[12]For the details of the deposition process see chapter 4.1.2.

Figure 4.8: *The chamber used for investigation of SSMs consists of a lid (L) and a base plate (BP). The silicon support is placed at the bottom (dotted line) and contacted from below by a metal pin (S). The counter electrode is a gold plate (G) in the top of the lid. An in- and outlet (I) for buffer exchange are also placed in the lid. The beam enters and exits the chamber through a kapton window (K).The whole chamber is temperature controlled by a heating device (H).*

As a first step in the preparation of SSMs the central support (dotted line in figure 4.8) for the silicon crystal is greased with Baysilone silicone paste (medium viscosity (Bayer; Germany)). This also works to seal of the space between substrate and electrode connector. A droplet of conductive silver is placed in the middle on top of the metal pin (S) and immediately covered with the silicon wafer. Subsequently, all other parts of the base plate are greased with the silicone paste and assembled.

4.3.2   SSM preparation

The preparation process of solid supported single bilayer lipid membranes is based on the fusion of small unilamellar vesicles (SUVs) on a hydrophilic substrate surface [WBK[+]84, RMB03, MMGK05, NGS06].

To prepare the SUV solution 5 mg of either a single lipid or a mixture (DOPC, DOPS, DPPC, DPPS) is dissolved in 1 mL chloroform. 200 μL lipid solution is taken and placed in a small vial. The solvent is evaporated in a vacuum chamber and the sample is kept there overnight. The aqueous buffer solution consists of 150 mM NaCl, 10 mM HEPES in MilliQ water and is regulated with NaOH to pH=7.4. In the case of anionic lipids, 2 mM $MgCl_2$ is added to the buffer solution. After evaporation of the organic solvent, the lipid films are rehydrated by adding 1 mL of the buffer to the vial. On vortexing, the solution becomes non-transparent and milky. Subsequently, the emulsion is fixed in a tip sonicator (Sonoplus, Bandelin; Berlin, Germany) and sonicated for about 15 minutes at 80% power until it becomes clear and transparent. To remove titanium splinters originating from the sonicator tip the SUV solution is centrifuged for 10 minutes at 14000 g.

After fixation of the substrate on the base plate it is put inside a plasma cleaner (Harrick; Ithaca, USA) for 2.5 minutes to hydrophilize the surface of the silicon, which will promote the adhesion and rupture of the vesicles. The chamber is closed by screwing the lid and connecting it to the heating circuit. After the temperature is raised to 40°C, 0.8 mL of the SUV solution is added to the chamber and the silicon surface is incubated for 1 h. To avoid further fusion of vesicles at the substrate surface the chamber is carefully rinsed with 40 mL - 60 mL buffer solution. Finally, it is mounted on the sample holder of the beamline goniometer and experiments are carried out according to chapter 3.5.

5 Theoretical model for x-ray phase contrast imaging of BLMs

In this chapter a model of simplified geometry will be introduced to enable structural and dynamical studies of bulged Black Lipid Membranes by x-ray phase contrast imaging (PCI). Furthermore, the propagation of wave fields interacting with this model system is described in the case of the Fresnel regime, comparable to in-line holography introduced by Gabor in 1948 [Gab48]. First experiments and the underlying theory have already been published in [BWZ+08, BMTS09, Mel09].
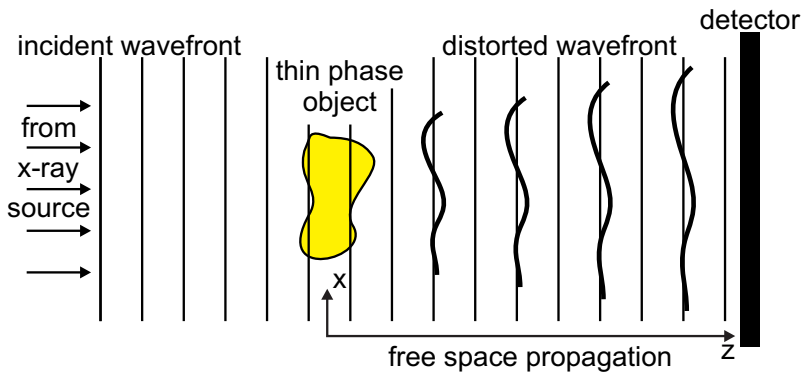

Figure 5.1: *Schematic representation of the principle idea of propagation based phase contrast imaging of a weak phase object. The distorted and the incident wavefront interfere on the detector after traveling along the z-axis in free space.*

For high x-ray energies many materials, especially the ones consisting of low-Z elements, e.g. biological samples, introduce the same problems as in optical microscopy: they become fully transparent in conventional "bright field" absorption images. In the case of visible light these challenges have been overcome by the introduction of phase contrast microscopy by Zernicke in 1942 [Zer42]. This technique is based on the interference of two fractions of a partially coherent wave field of wavelength λ that propagates through the object (see figure 5.1). One part, the reference wave, remains undistorted, since it undergoes no interaction with the material. The other one, the object wave, is diffracted by an angle $\Delta\alpha$ [Pag06] defined as

$$\Delta\alpha = \frac{\lambda}{2\pi}\frac{\partial\phi}{\partial x}. \qquad (5.1)$$

ϕ is the phase shift induced by the object, which is dependent on the optical properties, i.e. refractive index, along the x-axis.

In the x-ray regime the phase modulations of the photons traversing such an object are much increased and become several orders larger than the attenuation coefficients [MF95, AN01]. By the development of several x-ray phase sensitive techniques [Fit00, Nug10], such as diffraction [IB95, DGG⁺95a], grating [PWBD06, PDB⁺08], interferometry [BH65, Mom03] and the propagation based PCI methods, the observation of very thin and weak phase objectives has become possible.
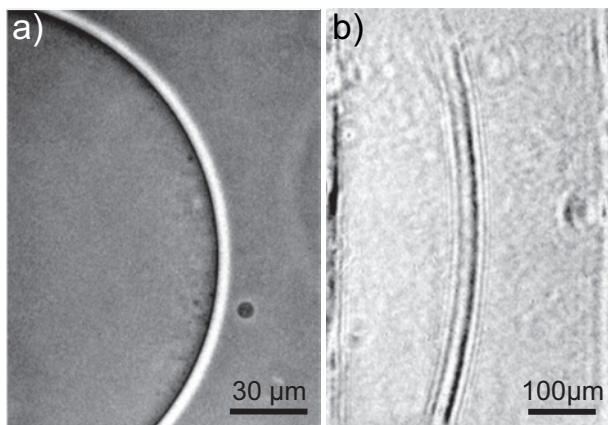

Figure 5.2: *Phase contrast visibility and resolution of objects, which are imaged by using different photon wavelengths, can clearly be distinguished: a) Light microscopy phase contrast image of a giant unilamellar vesicle made from DOPC in sucrose solution, which shows positive and negative interference fringes. b) X-ray phase contrast image of a bulged Black Lipid Membrane, which is freely suspended over an aperture in a solid substrate (prepared from DPhyPC lipids in aqueous buffer, propagation distance 3.63 m (ID10C)). By application of hydrostatic pressure across the membrane it bulges and becomes accessible for transmission x-ray phase contrast imaging.*

This chapter will exclusively deal with the description of the propagation based PCI or in-line holography, that was first described by Snigirev and colleagues in 1995 [SSK⁺95, ASKK96, RSS⁺96] and Cloetens and colleagues in 1996 [CBB⁺96]. At the same time the group of Wilkins presented their results, which were achieved using a micro-focus laboratory source, opening the possibility of clinical applications [DGG⁺95a, DGG⁺95b, WGG⁺96]. We now consider the structural

information which we can gain from PCI experiments conducted with x-rays. Note that a single bilayer can still be seen in phase contrast microscopy using visible light (see figure 5.2(a)), where the wavelength is much larger than the 5 nm thickness of the film. Consequently, the traversing wavefront will not carry any information on structures on the molecular length scale. When the wavelength becomes even smaller than the characteristic object dimension, as is the case for hard x-rays with $\lambda \lesssim 1$ Å, the visibility of the phase contrast pattern and the resolution must be distinguished from the previous case using visible light. Thus, we can expect the images structures in the x-ray regime to be determined by the interaction of the photons with structures in dimensions of λ. The two phase contrast images in figure 5.2, which were taken using visible light (a) and x-rays (b), nicely demonstrate the differences in the image formation processes.

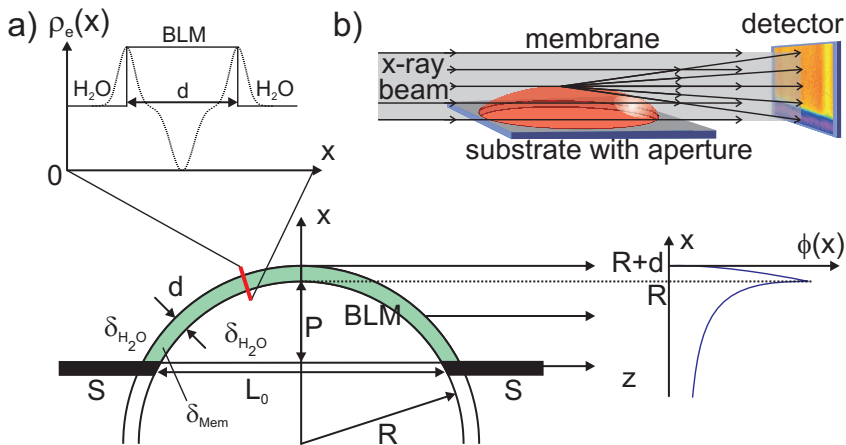## 5.1 Model assumption for bulged BLMs

Figure 5.3: *The system of bulged BLMs is modeled by the simplified assumption that the electron density $\rho_e(x)$ is constant across a membrane of thickness d. Based on experiments the BLM, supported by the substrate S, is drawn as a spherically bulged slab with radius R. For the calculation of the phase shift $\phi(x)$, the electron density is projected along the z-axis into a plane behind the membrane. b) Schematic representation of the experimental setup. The bulged BLM is imaged by using a transmitted x-ray beam. The detected image shows interference phase contrast of the transmitted and deflected x-rays.*

In analogy to the experimental simplification, namely the creation of a simple model membrane system, we will individually discuss the basics of image formation, before introducing more complexity. Therefore, we developed a simplified scheme of the BLM that can be included in the underlying equations being elucidated in the next section. This model is shown in figure 5.3. In the case of a swollen BLM of thickness d, that still includes organic solvent, we assume the electron density ρ to be constant across the membrane (see figure 5.3(a)). It is regarded as the most relevant parameter describing the scattering properties of x-rays in an object. In the following the dispersive part δ of the complex refractive index $n = 1 - \delta + i\beta$, instead of the electron density ρ_e, will be used. Both parameters are related as follows [Par54, AN01]:

$$\delta = \frac{\lambda^2 \rho_e r_0}{2\pi} \quad and \quad \rho_e = \frac{N_A Z \rho}{A} \tag{5.2}$$

with the wavelength λ, classical electron radius r_0, Avogadro's number N_A, atomic number Z, atomic weight A, and the electron density number ρ_e (including the material's density ρ). In the following the phase shift ϕ, that is induced by the propagation of the x-rays through the membrane, shall be derived. Based on the definition of thin phase objects, which is given in [Clo99, Pag06, Nug10], we assume the extension of the membrane along the z-axis and the interaction of the sample with the traversing photons to be very small. We consider no further propagation inside the object to occur, and thus the electron density can be projected into a plane behind the object. The phase profile is then simply

$$\phi(x) = -\frac{2\pi}{\lambda}\Delta\delta \int_{L_0} dz = -k\,\Delta\delta\,L(x), \tag{5.3}$$

with $\Delta\delta < 0$ the refractive index difference with respect to the surrounding water.

To make the membrane accessible to a transmitted x-ray beam it has to be "bulged out" from the supporting substrate S (see figure 5.2(b) and 5.3(b)), by application of a hydrostatic pressure across it. To determine $L(x)$ we now use a simplified geometric approach, i.e. we assume the membrane to be a smooth, spherical cap of thickness d under bulged conditions. This model appears to be well justified since the thermal fluctuations of the sphere will be suppressed by the dominating interfacial surface tension of the membrane, see discussion in chapter 2.1. The radius of the sphere is described by the radius R, or the diameter of the spanned aperture and the distance P between the outer rim and the support. The geometry of the experimental setup will be further described

in chapter 4. According to the simplified geometrical assumptions we can calculate the path length $L(x)$ (see figure 5.3) as follows

$$L(x) = \begin{cases} 2\left(\sqrt{(R+d)^2 - x^2} - \sqrt{R^2 - x^2}\right), & \text{if } x \le R \\ 2\sqrt{(R+d)^2 - x^2}, & \text{if } R < x \le R + d \\ 0, & \text{if } x > R + d. \end{cases} \quad (5.4)$$

By insertion of equation 5.4 into equation 5.3 we can calculate the phase shift ϕ, which is induced by the spherically bulged BLM along the path of the traversing x-rays (see figure 5.4).
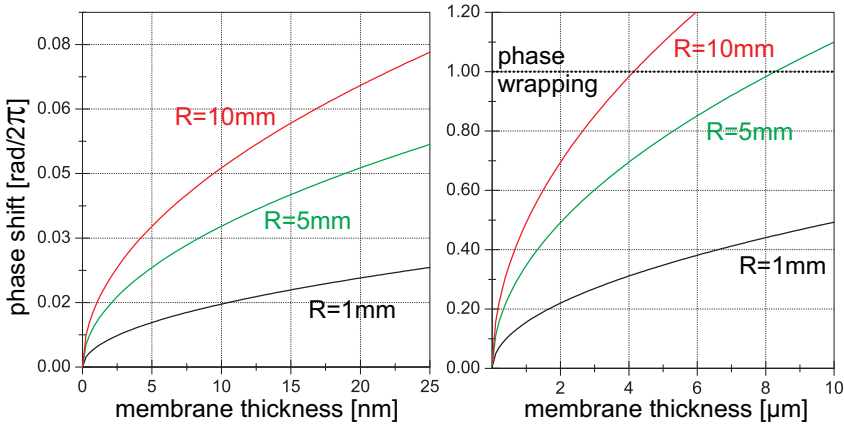

Figure 5.4: *Graphical representation of equation 5.3 including equation 5.4. The maximum accumulated phase shift of the x-rays at position $x = R$ inside the bulged membrane is plotted in units of 2π against the membrane thickness for different radii of curvature. The curves are calculated using the wavelength $\lambda = 0.708$ Å of photons with an energy of 17.5 keV and assuming a theoretical value $\Delta\delta = -1.23 \cdot 10^{-7}$ for the refractive index contrast between water and decane-lipid solution. It becomes obvious that phase shift can be easily increased by a factor of two as the radius of the bulged BLM is changed from 1 mm to 5 mm. For thick membranes a point can be reached where phase wrapping occurs.*

For further simplification we substitute $R' = \frac{R}{d}$ and $x' = \frac{x}{d}$. If we consider $R' \gg 1$ (i.e. $R \gg d$) we obtain a normalized path length

$$L_N(x') \approx 2 \cdot 2\sqrt{2R' + x'}\left[\sqrt{1 - x'} - \sqrt{-x'}\right], \, x' \epsilon \left[-R', 0\right]. \quad (5.5)$$

Because $|R'| \gg |x'|$ we obtain $2\sqrt{2R' + x'} \approx 2\sqrt{2R'}$, which leads to

$$L_N(x') = 2 \cdot 2\sqrt{2Rd} \begin{cases} \sqrt{1-x'} - \sqrt{-x'}, & \text{if } R' \le x' \le 0 \\ \sqrt{1-x'}, & \text{if } 0 < x' \le 1 \\ 0, & \text{if } x' > 1 \end{cases} \tag{5.6}$$

in units of membrane thickness d on the abscissa.

5.2 Propagation based phase contrast imaging of bulged BLMs

The formation of an image $E(x_d, y_d, z_d)$ at a position z_d in the detector plane D is given by propagating the impinging planar wave field (illumination function) $E(x, y, 0) = E_0$ interacting with the complex-valued optical transmission function [BW99, LK03, CBB$^+$96] $T(x, y) = B(x, y) \cdot e^{\mathrm{i}\phi(x,y)}$ along the direction of the beam (see figure 5.5).
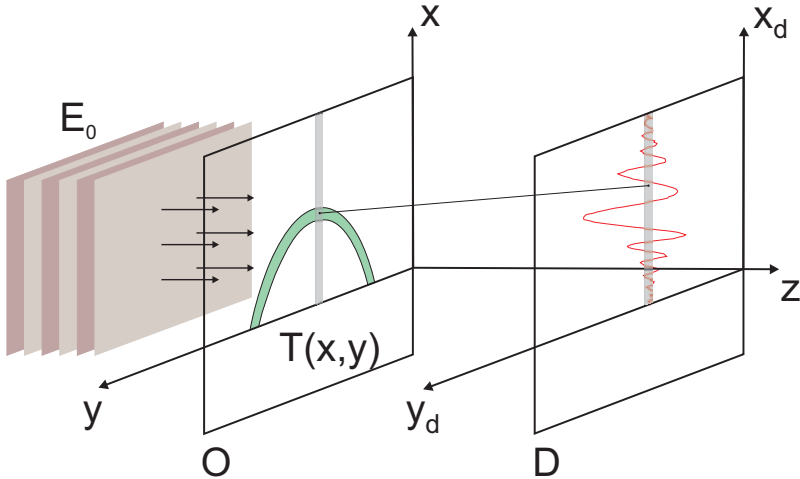

Figure 5.5: *The sample at position O is described by a transmission function T(x, y) obtained by projection of the electron density ρ(x) along the z-axis. After free space propagation of the exit wave over a distance z along the optical axis, a Fresnel interference pattern I(x) is recorded in the detector plane D, representing a phase contrast image of the projected density profile.*

This reflects the optical properties of the illuminated object at position O, where ϕ is the phase shift induced by the object and B describes the absorbtion, which

we will neglect here ($B=1$) since we are considering weak phase objects. Furthermore, we are only interested in the electron density distribution along a single axis $\rho(x)$. Thus we will restrict our discussions to the one-dimensional case in the following calculations and so for the wave field E_{in} in the plane behind the object:

$$E_{in} = E_0 \cdot T(x) = E_0 \cdot e^{i\phi(x)} \tag{5.7}$$

For a parallel beam geometry (illumination function considered as a plane wave) and scattering signals at small momentum transfers, the imaging process is described by the Kirchhoff diffraction integral using the paraxial Fresnel-approximation [Cow75, SSK$^+$95]:

$$E(x_d, z) = \sqrt{\frac{i}{\lambda z}} \int_{-\infty}^{\infty} E_{in} \, e^{\frac{ik}{2z}(x - x_d)^2} dx. \tag{5.8}$$

By using $\sqrt{i} = e^{i\frac{\pi}{4}}$, $k = \frac{2\pi}{\lambda}$ and equation 5.7 we can write equation 5.8 as

$$E(x_d, z) = E_0 \sqrt{\frac{k}{2\pi z}} e^{-i\frac{\pi}{4}} \int_{-\infty}^{\infty} e^{i\phi(x)} e^{\frac{ik}{2z}(x - x_d)^2} dx. \tag{5.9}$$

Alternatively equation 5.9 can be calculated instead of convolving the wave field E_{in} in real space with the *fresnel propagator kernel* [Gui77, CBB$^+$96, LK03]:

$$H(x, y) = \sqrt{\frac{k}{2\pi z}} e^{-i\frac{\pi}{4}} e^{\frac{ik}{2z}(x - x_d)^2} \tag{5.10}$$

by performing a multiplication in Fourier space described in detail in references [Clo99, Pag06, Nug10].

The detected intensity is given as $I(x, z) = |E(x_d, z)|^2$ for each propagation (defocus) distance z. For numerical computation of the Fresnel intensity profile $I(x, z)$, a simple box model of $\phi(x)$ can be used for the central interval of the object plane $[x_{min}, x_{max}]$, where the phase shift $\phi(x)$ is non-zero (see figure 5.6). The interval is divided into N segments of a constant phase shift $\phi_j = \phi(x_j)$, with $x_j = x_{min} + j\Delta$, and $K_j := T(x_{min} + j\Delta) = e^{i\phi(x_{min}+j\Delta)}$. Using Fresnel Sine and Cosine functions the field in the detector plane becomes

$$E_c(x) = \sum_{j=0}^{N-1} \frac{E_0 K_j}{\sqrt{2}} e^{-i\frac{\pi}{4}} \left[(C(w_{j+1}) - C(w_j)) \right. \tag{5.11}$$

$$\left. + i(S(w_{j+1}) - S(w_j)) \right] \tag{5.12}$$

with $w_j = \sqrt{\frac{k}{\pi z}}(x_{min} + j\Delta - x_d)$ and the Fresnel functions defined as follows:

$$S(w) = \int_0^w \sin\left(\frac{\pi}{2}\alpha^2\right) \tag{5.13}$$

$$C(w) = \int_0^w \cos\left(\frac{\pi}{2}\alpha^2\right) \tag{5.14}$$

To obtain the complete field $E(x) = E_c(x) + E_l(x) + E_r(x)$, the fields $E_l(x)$ and $E_r(x)$ due to the source points in the left and right half-planes (bordering the object interval $[x_{min}, x_{max}]$ in the sample plane) have to be added. For these regions constant (in practice often zero) relative phase shifts ϕ_l and ϕ_r can be assumed. For computational speed, the actual calculations of $I(x, z)$ during the least-squares fitting are performed in trapezoidal approximation of the transmission function $T(x)$. Therefore, the phase $\phi(x)$ in each segment is linearly approximated, and better accuracy can be obtained for a given number of segments (dashed line in figure 5.6).
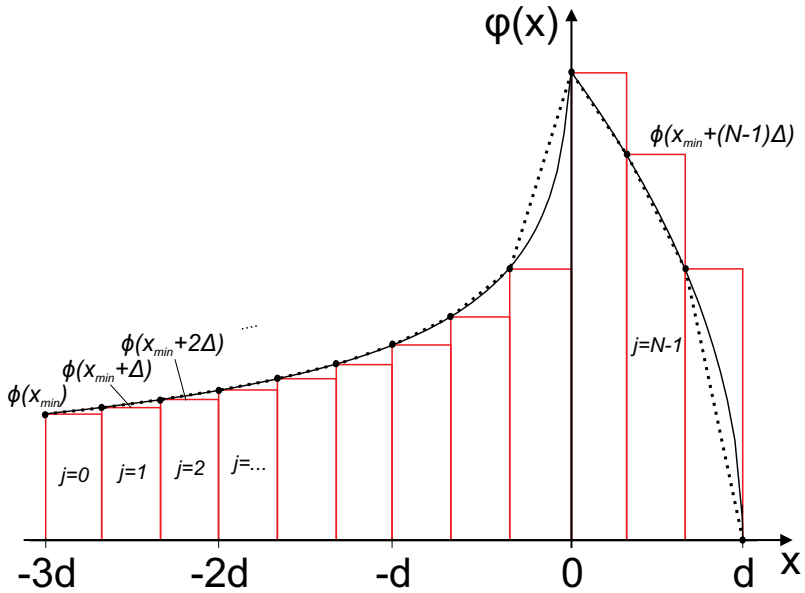

Figure 5.6: *The transmission function consisting of the phase $\phi(x)$ (solid line) is sub-divided into N slabs of constant phase $\phi(x_min) + j \cdot \Delta$ (red boxes). For computational speed, $\phi(x)$ is modeled by a trapezoidal approximation (dashed line).*

For a segment from x_j to x_{j+1}, the phase $\phi(x)$ is linearly approximated by

$$\phi_j^m = m_j x + b_j, \quad x \epsilon [x_j, x_{j+1}] \tag{5.15}$$

where $m_j = \frac{\phi_{j+1}-\phi_j}{x_{j+1}-x_j}$ and $b_j = \phi_j - m_j x_j$. We can now write the resulting electric field E_c as a sum of Fresnel-Kirchhoff integrals for segments with a linear phase shift

$$E_c(x_d, z) = E_0 \sqrt{\frac{k}{2\pi z}} e^{-i\frac{\pi}{4}} \sum_{j=0}^{N-1} \int_{x_j}^{x_{j+1}} e^{i(m_j x + b_j)} e^{\frac{ik(x-x_d)^2}{2z}} \, \mathrm{d}x. \tag{5.16}$$
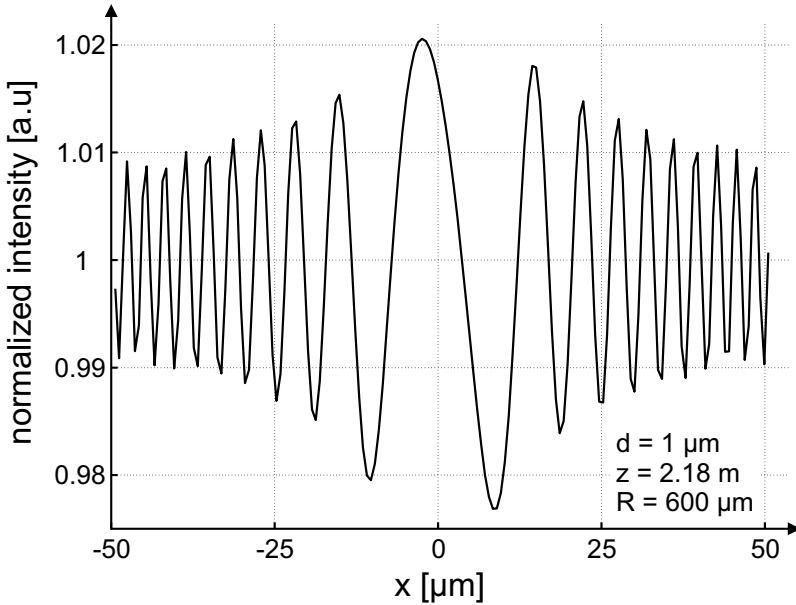

Figure 5.7: *Simulation of the fresnel diffraction pattern of a bulged membrane by using equation 5.17 and the depicted parameters ($\Delta\delta = -1.23 \cdot 10^{-7}$, $\lambda = 0.59$Å).*

Neglecting the constant phase factor $e^{-i\frac{\pi}{4}}$, the integrals over each segment can be written as

$$E_c(x_d, z) = \frac{E_0}{\sqrt{2}} \sum_{j=0}^{N-1} e^{i(b_j + m_j(x_d - \frac{m_j z}{2k}))} \tag{5.17}$$
$$\cdot \left[\left(\mathrm{C}\left(w_{j+1}^T \right) - \mathrm{C}\left(w_j^T \right) \right) + \mathrm{i}\left(\mathrm{S}\left(w_{j+1}^T \right) - \mathrm{S}\left(w_j^T \right) \right) \right]$$

with

$$w_j^T = \sqrt{\frac{k}{\pi z}} \left(x_j - x_d + \frac{m_j z}{k} \right). \tag{5.18}$$

From equation 5.17 the final fresnel diffraction pattern of a bulged BLM can now be calculated, as it is shown in figure 5.7[13]. At this point different predictions can be made about the expected results:

- At first, we see from equation 5.6 that a variation of the membrane thickness d and the radius R will have the same effect on the path length $L(x)$. In the same way, the phase $\phi(x)$ (see equation 5.3) and the fringe amplitude are changed. As a consequence, the exact knowledge of the radius R value is essential to precisely fit d. As the membrane tends to assume an almost spherical shape to reduce its surface tension we can deduce the radius along the propagation direction of the x-rays from the fitted contour of the membrane perpendicular to the beam (see section 6.3).

- Secondly, the dispersion coefficient $\Delta\delta$ influences the phase linearly (see equation 5.3), while d and R only contribute with a square root behavior. Thus, $\Delta\delta$ can be fitted separately. The data analysis is fixed to theoretical values to reduce the number of fit parameters and fit complexity.

- Finally, and most interestingly, the intensity will increase as the wavelength λ and the propagation distance z decrease. In terms of λ this improvements will be compensated by less interaction between photons and the sample with higher photon energies (see equation 5.2). Regarding z, the fringe distance will shrink on reduction of the propagation distance [Mel09] and finally lead to a loss in resolution. Since the energy is mostly fixed at synchrotron beams, we can overcome the limits in resolution for small z by using a divergent beam geometry.

5.3   Divergent beam imaging

In this work we also apply divergent beam propagation imaging to the presented membrane system. By using the geometry of a divergent beam, yielding a magnified phase contrast image of the object [MCM+07, BCG+09], one can compensate for wavelength and propagation distance dependent effects. This leads to an increasing phase contrast at the expense of fringe distance and, consequently, less resolution, as discussed before. Thus, it allows one to circumvent the limited resolution, which is mainly defined by the detector and is, in

---

[13]Simulations of different membrane models and their dependence on the characteristic system parameters d, R and z are discussed in [Mel09].

the best case, in the range of 1 µm (diameter of the point spread function (PSF)) [MDC^{+}09]. Especially in the case of Fresnel fringes originating from the BLM (see figure 5.7), the resolution of high spatial frequencies at high diffraction angles is increased. Thus, the propagation distance can be reduced without further loss in resolution. Consequently, we can take advantage of the fact that the phase sensitivity term of the Contrast Transfer Function (CTF) [SGF^{+}09], simply the fourier transform of the image intensity distribution, oscillates.
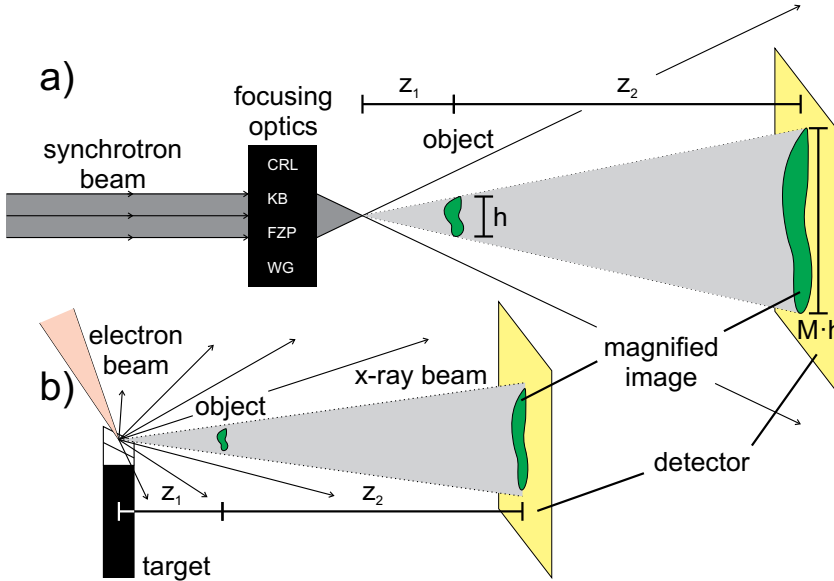
Figure 5.8: *Schematic representation of the divergent beam geometry for (a) a synchrotron and (b) a laboratory source setup. The object at position z_1 behind the focus is magnified at the detector by a factor M after propagation along a distance z_2. CRL: compound refractive lens, KB: Kirkpatrick-Baez mirror, FZP: Fresnel zone plate, WG: waveguide.*

On variation of the propagation distance z, the spatial frequency of the object $\nu_{x,y}$ and the wavelength λ, the phase contrast amplitudes in the image will change. The CTF gives direct access to the condition of optimal phase contrast for a weak phase object of dimension a at propagation distance z_{eff}:

$$1 \simeq 2\sqrt{\lambda z_{eff}}\,\nu_{x,y} \quad \Rightarrow \quad z_d = \frac{a^2}{2\lambda} \tag{5.19}$$

This is equivalent to the resolution criterion for two Airy patterns at distance z_d of two propagated point sources. They have to be separated by twice the radius $r_{FZ} = \sqrt{\lambda \, z_d}$ of the first Fresnel zone to be still distinguishable from each other [Wei02].

For a bulged BLM of thickness 1 μm, imaged by hard x-rays (20.92 keV, λ =0.59Å), the optimal defocus distance z_d is 8.5 mm. This distance could not be reached at a parallel beam setup (see chapter 6.1.1). There the fringe visibility at z =6 cm (for nearly the same photon energy as in the divergent setup) was dramatically decreased due to missing resolution (see chapter 7.1). In the divergent beam geometry (see chapter 7.2) the images show nice phase contrast signals even at very small propagation distances, z =3 mm, without any limitation by the detector PSF (see chapter 6.4).

It was shown [Fuh06] that a divergent beam experiment is equivalent to a parallel beam geometry when introducing an effective pixel size p_{eff}, which is the physical pixel size p_s divided by the magnification M (see figure 5.8). Furthermore, the propagation distance z is replaced by an effective propagation distance z_{eff}. M and z_{eff} are defined as follows [Fuh06, LCC$^+$97, MMW$^+$02]:

$$M = \frac{z_1 + z_2}{z_1}, \quad z_{eff} = \frac{z_1 \, z_2}{z_1 + z_2} \tag{5.20}$$

Experimentally a divergent beam geometry can be achieved in different ways (see figure 5.8). It has been described for hard x-ray synchrotron radiation using wave guides (WG) [Fuh06, dFJS$^+$98, LCC$^+$97], compound refractive lenses (CRL) [SKSL96, LSR$^+$99, SMK$^+$02] and Kirkpatrick-Baez-mirrors (KB) [MCM$^+$07, BCG$^+$09]. For point-like, also called micro-focus, lab sources various approaches are presented in literature [MMW$^+$02, MDG$^+$03, TOH07, OTVH08].

6 X-ray phase contrast imaging: experimental aspects

6.1 Synchrotron setups and experiments

6.1.1 Beamline layout at ID10C (Troïka III)

The parallel beam experiments are carried out at the insertion device 10C (Tro-ïka III) (see figure 6.1) undulator station of ESRF (Grenoble, France), which has a source size of 928 µm (h) x 23 µm (v) (FWHM) with a divergence of 28 µrad (h) x 17 µrad (v). The beam is monochromatized by a Diamond-(111)-crystal monochromator (mono) to 20.92 keV, with a bandpass of $\frac{\Delta\lambda}{\lambda}$ =3.7·10^{-5}, also see [BWZ^{+}08]. This corresponds to a x-ray photon wavelength of 0.592Å. The (unfocused) beam size at the sample is 1 mm x 1 mm, as controlled by a series of high quality motorized slits optimized for coherent scattering (PS, SS, ES). The beam is attenuated by a set of silicon absorbers (A). The primary beam intensity is recorded by a vertically positioned monitor close to the sample. Images are taken at the three different propagation distances z=0.06 m, 2.18 m, and 3.63 m, respectively, between sample and detector (as referred to as the defocus distance), using a Sensicam 12-bit CCD camera (PCO Imaging, Germany) with 1240 (h) x 1024 (v) pixels and a pixel size of 6.7 µm x 6.7 µm. The detector includes a scintillation foil (9.9 µm Europium doped Lutetium Aluminum Garnet (LuAG:Eu) on 170 µm undoped Yttrium Aluminium Garnet (YAG)), which is imaged by a 10x objective onto the detector. The effective theoretical pixel size of the images is then 0.67 µm. The experimental effective pixel size of the detector will be discussed in the section 6.4.
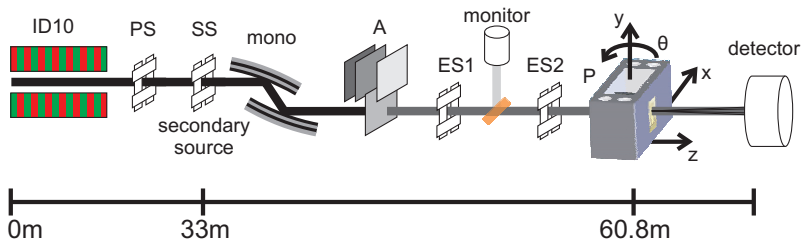

Figure 6.1: *Outline of the undulator station ID10C at ESRF, Grenoble, which is used for parallel / propagation beam imaging experiments of bulged BLMs. See text for explanation of components.*

6.1.2 Beamline layout of ID22NI

Divergent beam imaging experiments are performed at the insertion device 22NI undulator station at ESRF (Grenoble, France). Figure 6.2 shows a schematic

representation of the experimental setup. It includes a U42 undulator (ID22), which is operated at the third harmonic to deliver a pink x-ray beam with photons of 17.5 keV energy and a corresponding wavelength of 0.708 Å. The source size at the undulator is 700 μm (h) x 30 μm (v) (FWHM) with a divergence of 28 μrad (h) x 5 μrad (v).
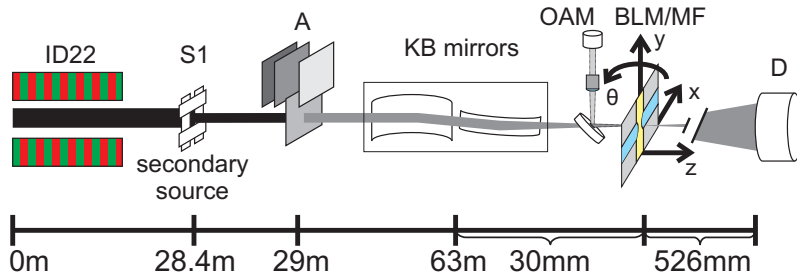

Figure 6.2: *Outline of the undulator station ID22NI at ESRF, Grenoble, which is used for divergent beam imaging experiments of bulged and microfluidic BLMs. See text for explanation of components.*

A set of slits (S1) defines a secondary source size of 25 μm in the horizontal direction, while in the vertical a size of 30 μm is given by the undulator. The focusing Kirkpatrick-Baez (KB) mirror-pair is located in the experimental hutch [HRC+01, HCRM05]. The sample (S) (either BLM chamber (figure 4.1) or microfluidic device (figure 4.6)) is placed in the focus of the KB system that coincides with the focus of the on-axis microscope (OAM). A drilled mirror allows for the simultaneous detection of light microscope and x-ray images and thus a faster alignment of the sample in the beam. The focus is located 30 mm downstream the KB mirrors and has a diameter of 130 nm (v) and 140 nm (h), which was measured by performing knife edge scans in both directions. Optionally, a set of polished silicon absorbers can be placed in the beam to attenuate the intensity. The detector (D) is a Fast-REadout, Low-Noise (FRELON 2000; ESRF, Grenoble[14]) CCD camera [LCM+07]. It is combined with a 24 μm thick LSO:Tb (Terbium doped Lutetium-Oxoorthosilikat, Lu_2SiO_5) scintillator, optimized for high resolution imaging, that converts the x-rays into visible light photons of 550 nm wavelength and is supported by a 170 μm YSO (Ytterbium-Oxoortho-silicate, Yb_2SiO_5) substrate [CRP+09, MDC+09, RCMD09]. It is placed 526 mm behind the KB focus. The image is magnified by a 10x objective and a 2.5x eye-piece to fit the dimension of the 14-bit Kodak KAF4320 CCD chip with a physical pixel size of 24 μm and a resolution of 2048 pixels x 2048 pixels. Thus, the

---

[14]Development by Analog Transient Electronics Group (ATEG) in the ESRF Instrument Support Group.

effective theoretical pixel size of the images is 0.96 µm. The experimental effective pixel size, also described as the point spread function (PSF) of the detector, will be discussed in section 6.4. The field of view is reduced to a size of 1500 pixels x 1500 pixel corresponding to the beam diameter at the detector position. The position z of the sample was varied in a range of defocusing distances $3\,\text{mm} \le z \le 200\,\text{mm}$, with respect to the KB mirror focus. The microfluidic devices are mounted on a specially designed holder, which allows movement to very small z positions, i.e. close to the KB focus, which results in a large magnification (see 5.20).

6.2   X-ray phase contrast imaging measurements

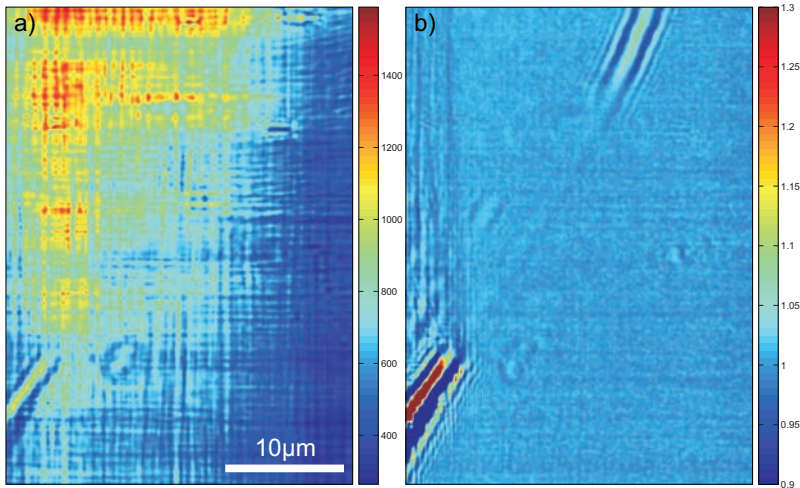**Figure 6.3:** *a) Raw image from ID22NI beamline, which is taken with illumination time 0.5 s at an effective propagation distance $z_{eff} = 18.1\,mm$ and is fully dominated by KB mirror artefacts. The BLM can hardly be recognized. b) After background correction the features of the sample become visible. For higher visibility the images are smoothed by a disk function of five pixels radius. . Raw data: abreakf-175, background: abreakf-172. BLM made of DPhyPC in aqueous buffer.*

The steps of alignment and image acquisition for both bulged BLMs and mf-BLMs are very similar. Thus, the following description will be restricted to the case of BLMs. After the preparation of the membrane, as described in chapter 4.1.4, the sample is roughly moved to the center of the beam by translation

along x, y and z axes (see figures 6.1 and 6.2). Subsequently, the sample is aligned by rotating it around θ so that the substrate (Teflon or silicon) is perfectly parallel to the beam. The aperture, which is spanned by the BLM, is located by turning the sample 20° or more in θ. At the aperture the substrate becomes slightly transparent. When Teflon foils are used, the edges of the aperture can be seen inside the foil, even for parallel alignment. After this step the membrane is bulged into the beam (see figure 5.2), by running the pump, which is connected to the buffer reservoir on the back side of the BLM. The data can be taken image by image, or by running a fast acquisition series that allows frame rates up to 5 fps in full resolution. Figure 6.3 shows a representative raw and background corrected image of 0.5 s illumination time, which was at a propagation distance z_1 =20 mm at the ID22NI beamline. From figure 6.3(a) it can easily be seen that the artefacts of the beamline optics dominate the entire image. Thus, the acquisition of empty beam images is of great importance. These are taken by moving the sample, e.g. the BLM, out of the beam by only a small translation so that the x-rays still traverse the aqueous buffer solution. Figure 6.3(b) shows the raw image after division by the background image.

6.3   Data treatment

Figure 6.4 describes the basic steps of raw data treatment and reduction. The recorded raw images (figure 6.3(a) and 6.4(a)) are corrected for dark count and empty beam intensity variations by means of a MatLab (version 2009b, Mathworks; MA, USA) graphical user interface (GUI) called *start-straighten-profiles-gui* [Mel09]. The position of the bulged membrane is defined by three data points, which have to be precisely placed along the contour. To increase the visibility of the very weak scattering signal of the thin Black Lipid Membranes every image is smoothed by a radial disk function with a five pixels radius. Subsequently, a circle with free radius of curvature R is fitted to the three points assuming spherical symmetry (figure 6.4(b)). Along a defined region of interest (ROI), where the contrast of the signal is homogeneous, radial cuts across the membrane diffraction signal are taken. A second GUI, called *start-extract-profiles-gui* [Mel09], is used to perform the final intensity profile extraction. The intensity of the radial cuts is mapped to a rectangular array in polar coordinates (angular and radial position) (figure 6.4(c)). After averaging the intensities in the ROI over angular coordinates (column sum), a one-dimensional representation of the Fresnel fringes $I(x, z)$ is obtained along with representative error bars. As described in chapter 5.3, the effective pixel size z_{eff} is calculated for the case of divergent beam experiments and according to this the abscissa is rescaled. The intensity profile is finally treated by least-squares fitting the the-

oretical model (figure 6.4(d)). Further information about the fitting procedure is given in section 6.5.
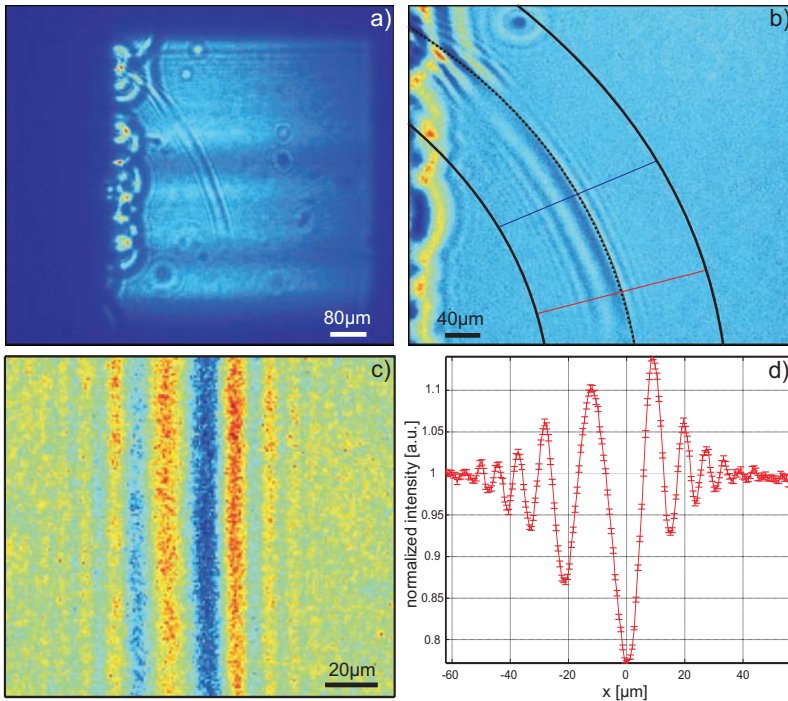

Figure 6.4: *Illustration of the data reduction scheme: a) Raw images recorded at different detector positions z, showing the contour of the membrane and vesicles adhering to the substrate in phase contrast, with the associated Fresnel fringes. b) Empty beam intensity variations are removed by division with empty beam images. This yields smooth intensity images, which are additionally convolved with a five pixels radial disk function to increase visibility of thin BLMs. c) The spherical contour is transformed into polar coordinates by taking radial cuts along a defined region of interest. d) One-dimensional intensity curves $I(x,z)$ result from summation along the vertical axis.*

6.4   Detector point spread function and partial coherence

Before we discuss the fitting procedure and data evaluation, we will briefly introduce two essential effects, namely the *partial coherence* of the beam and the

point spread function (PSF) of the detector, which influence the Fresnel fringe visibility and image resolution.

6.4.1 Partial coherence of synchrotron radiation

To a certain degree an insertion device, i.e. undulator based photon generation, can be considered as an extended, fully incoherent source. Partial coherence is achieved by propagation of the beam along a distance z, i.e. the distance z_1 between source and sample. Furthermore, the transverse coherence length ξ_l and, consequently, the visibility of interference patterns, e.g. Fresnel fringes, increases as the lateral dimension Δs of the source decreases. This can be understood as follows: an object which is illuminated by an extended source of size Δs at distance z_1, will be smeared in terms of the intercept theorem by Δx in the image (detector) plane at distance z_2 (see figure 6.5).
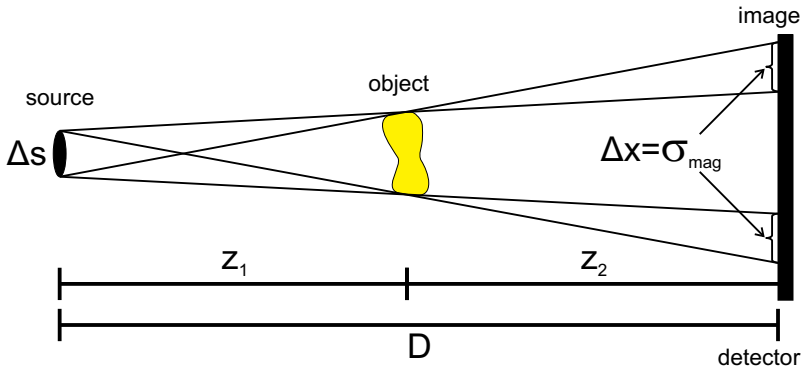

Figure 6.5: *Schematic representation of the smearing $\Delta x = \sigma_{mag}$ of an image at distance z_2 behind an object, which is illuminated by an extended source Δs source at distance z_1.*

This relation is described by the following equation [Wei02, Sch08]:

$$\Delta x = \frac{z_2}{z_1} \Delta s \tag{6.1}$$

If we consider the source to have an Lorentzian shaped intensity distribution then the smearing will also be of this shape. The use of a Lorentzian function instead of a Gaussian is motivated by the following fact. In both experiments, optics with a beam defining aperture, i.e slits and mirrors (see sections 6.1.1 and 6.1.2), are used to create a secondary source. This will always give an Airy

pattern-like beam profile. A function with broad side tails, i.e. a Lorentzian, might thus be better suited to describe such secondary sources. Additionally, the use of a Lorentzian gives better fit results compared to a Gaussian function. The contribution of partial coherence, depending on z_1, z_2, and Δs, to the image formation is nothing else but a convolution of the theoretical simulated image with a Lorentzian function of FWHM $\sigma = \frac{\sigma_{mag}}{M}$ with $\sigma_{mag} \equiv \Delta x$. Here σ is the value, which is obtained from the fit procedure in the demagnified image and σ_{mag} corresponds to the image on the detector. Experimental values and a corresponding fit of equation 6.1 will be shown in figures 7.7 and 7.17of sections 7.1 and 7.2. Consequently, the fitted values of σ can be revised and checked for the agreement to theoretical predictions. In some images both thin and thick regions of the membrane are detected simultaneously. As the fringe visibility is much higher for the thicker part of the membrane, the σ values can be fitted in these regions with high precision and used to fit the profiles of thin membrane regions in the same image.

6.4.2 Point spread function

The second effect that can have an effect on the image formation is the point spread function (PSF) of the detector system. It was shown that especially for high resolution, scintillator based detectors, knowledge of the PSF can be of certain importance for the simulation and fitting of the experimental data [KRSS98, MK06]. In this work we have seen no limitation of the image resolution by a smearing of the detector. This becomes obvious when looking at the images, when due to the magnification the Fresnel fringes are highly oversampled, i.e. each oscillation is composed of 20 or more pixels. This is also confirmed by the graphs in the respective results (see figures 7.7 and 7.17). We show that the FWHM σ of the envelope function of the fringe pattern is exclusively dependent on the propagation distance. If there was a contribution of the detector PSF we would see an asymptotic behavior of the graph for large σ, i.e. increasing $\frac{z_2}{z_1}$. We can therefore exclude a suitable effect of the PSF in the propagation regimes where the images are taken. This justifies restricting to a single Lorentzian envelope function, as described in the following section.

6.5 Data fitting procedure

Data fitting is performed in MatLab (version 2009b, Mathworks; MA, USA) using a χ^2-minimization algorithm called "Nelder-Mead simplex method" [LRWW99]. It is used by the MatLab implemented function *fminsearchbnd*, allowing for the introduction of boundaries to the fitting parameters. The main

variables, which contribute to the image formation were introduced in chapter 5, namely the thickness d, the radius R, the refractive index difference $\Delta\delta$ and the effective propagation distance z_{eff}. The determination of R was described in section 6.3. $\Delta\delta = \delta_{BLM} - \delta_{H_2O}$ is calculated according to equation 5.2 using the literature electron density values of water, solvent (decane), and lipids, so that we get $\Delta\delta = -1.23 \cdot 10^{-7}$. z_{eff} is defined by the experimental setup (see equation 5.20). Two additional parameters, x_{shift} and I_{shift}, are introduced to correct for errors in the image processing. x_{shift} shifts the diffraction pattern along the x-axis, since the accurate position of the membrane is unknown. I_{shift} compensates for an offset in the intensity that may result from slight differences between mean intensities of the object and background images. As characterized in the previous section, the last fitting parameter is the FWHM σ of the convolved Lorentzian function. This takes into account both the finite lateral coherence length of the x-rays, originating from the finite source size [dFJS+98], and the point spread function of the detector, even if no limitation could be detected from the latter. The computational details and the source codes of the algorithms used in the fitting procedure refer to [Mel09].

The fitting is performed by starting with a free fit of the diffraction pattern, leaving d, x_{shift}, I_{shift} and σ free. Although the zero position of z_{eff} is defined by the geometrical dimensions of the beamline setup, a refinement of the measured values within a reasonable range is allowed during the fit. Subsequently, the values and their boundaries were reduced step by step to end up with the determination of the membrane thickness d. The χ^2-errors of the fits are calculated as follows: After the final fit result P_0 and the corresponding χ_0^2 is obtained every fit parameter P_i is varied in such way that a value of χ_0^2+1 is reached. Thus we get an upper and lower value for every P_i, for which holds $P_{i-} < P_0 < P_{i+}$ with $\chi^2(P_{i-}, P_{i+}) = \chi_0^2 + 1$.

7 X-ray phase contrast imaging: structural results

This chapter will present the results which are obtained from experiments at the two undulator beamlines ID10C (Troika III) and ID22NI at ESRF in Grenoble, France. At first we will discuss the phase contrast imaging results for the parallel beam geometry from five representative examples, which have already been published in [BMTS09]. Subsequently, we will get to the scope of this chapter, namely divergent beam imaging which enables the visualization of thinned, bimolecular membranes.
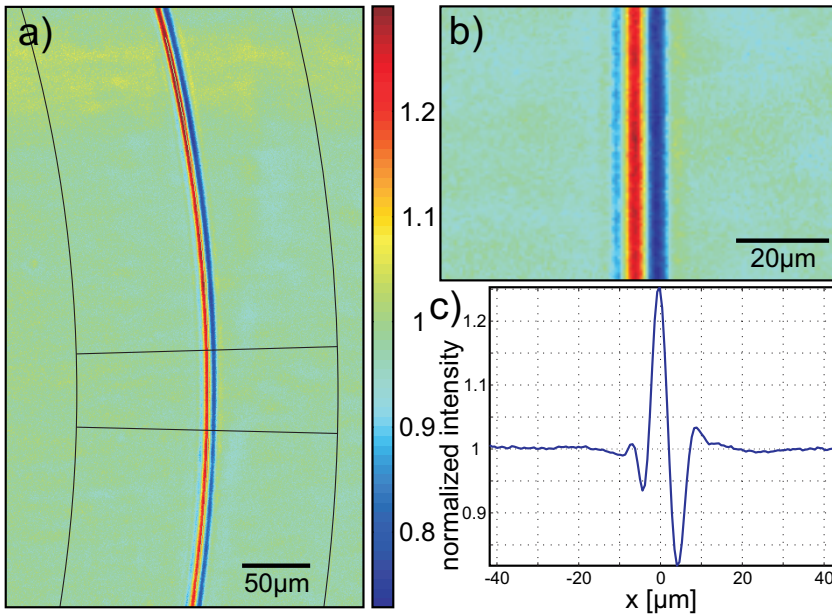
Figure 7.1: *a) X-ray phase contrast image of a Black Lipid Membrane obtained from the first experiment, which is performed at the BM05 (ESRF; Grenoble, France) with ROI (solid lines). b) After summation of the straightened ROI the one dimensional intensity pattern c) is obtained. The readers attention is directed to the poor fringe visibility, although this film is still thick and swollen with solvent. Images taken at $z_{eff} = 1.25\,m$ with illumination time 0.5 s. Raw data: DPhyPC_p60114. BLM made of DPhyPC in aqueous buffer.*

Before starting with quantitative results, the very first experiment shall be presented. It was carried out at the bending magnet beamline BM05 at ESRF, where

the visibility of Black Lipid Membranes in x-ray phase contrast images was shown for the first time [BWZ⁺08]. A bulk membrane of DPhyPC lipid in aqueous buffer can be observed at a propagation distance of 1.25 m and becomes invisible when it thins to a certain thicknesses. Due to inappropriate experimental conditions, such as a lack of coherence and focusability, the visibility of Fresnel fringes is very weak and, thus, only a qualitative result is shown in figure 7.1. It may be compared to the results in the next sections to reveal improvements in the experimental protocols used for imaging of BLMs.

7.1 Parallel beam imaging

In the parallel beam setup at ID10C (see figure 6.1), we have worked at three different propagation distances $z = 6$ cm, 2.18 m and 3.63 m. According to this the data sets are referred to as *short*, *middle* and *long* and will be discussed separately in the following sections[15]. The fit results for each distance and the respective image are shown as insets in the figures. We have obtained errors of less than 1% of the absolute intensity values for the intensity profiles of the following data sets. Such a small value results from homogeneous noise levels in the images and an average over a large number of horizontal lines in the straightened diffraction patterns and, thus, errors will not be shown for the parallel beam experiments. The membranes shown in the images of this section are made of DPhyPC in aqueous buffer (following preparation protocol in section 4.1.4) as long as not indicated differently. The same holds for the underlying model, namely the bulged membrane slab model, which is used in the fitting procedure of the intensity profiles and has been presented in chapter 5.

7.1.1 Long propagation distance

Figure 7.2(a) shows a representative diffraction pattern which was recorded at the longest propagation distance of 3.63 m. The fit in 7.2(b) matches the experimental data reasonably well, yielding a relatively small χ^2 compared to profiles which are extracted from other positions along the contour. A reason for this could be an uncertainty in R, since the membrane is prepared across an elliptic aperture meaning the membrane curvature will differ in both directions. As a result, a refinement of R was allowed during the fit. From comparison of Lorentzian and Gaussian convolution functions, and the characteristic FWHM values σ, we obtain a better fit quality of about 20%-30% for the Lorentzians [Mel09]. This is in agreement with the assumed shape of the illumination function, that is defined by the secondary source (see chapter 6.4).

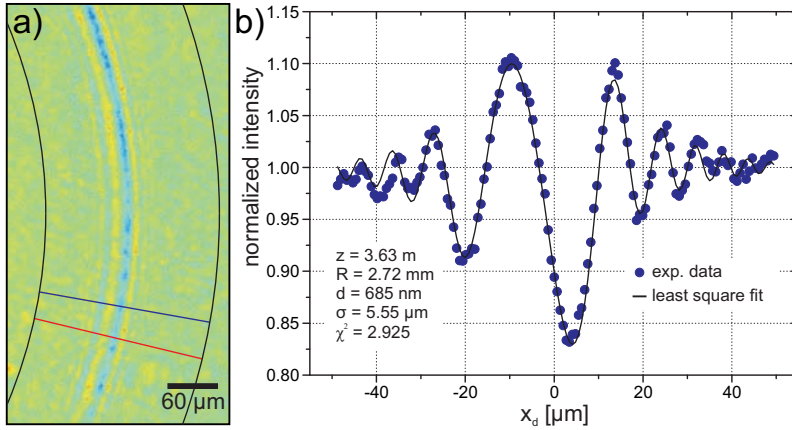[15]A list of data sets and details of the image formation process are presented in [Mel09].

Figure 7.2: *a) Representative phase contrast image of a bulk BLM (DPhyPC) taken at a distance of z = 3.63 m. The diffraction pattern nicely shows the propagated Fresnel fringes. b) The intensity profile I(x) was extracted from the ROI between the red and blue line in (a). Fit results indicate a bulk state of the membrane with d = 685 nm. $\Delta\delta$ is fixed to its theoretical values. After a refinement of R, σ and z, d is finally fitted.*
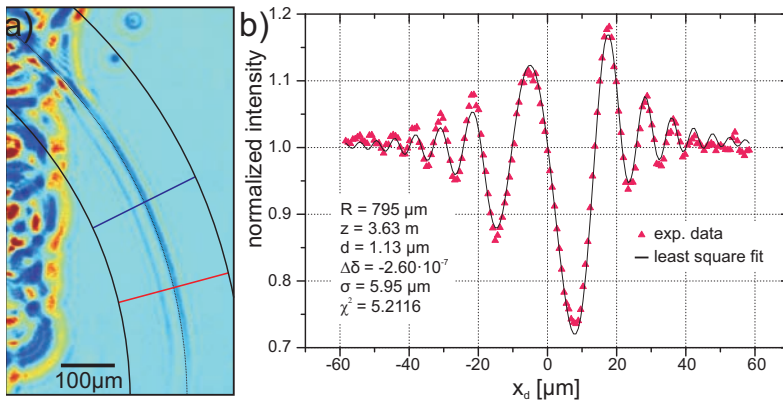

Figure 7.3: *a) Black Lipid Membranes have been prepared in a sucrose-buffer solution to increase the contrast between lipid bilayer and surrounding water. b) The theoretical values can be confirmed by the fit values, but an effect on the fringe visibility for thin membranes is not obtained. R, z and σ are fixed during the fit.*

As well as the previous experiments where using a standard buffer (see chapter 4.1.4), we also prepared Black lipid Membranes in a sucrose/buffer solution (5 mg sucrose/5 mg buffer solution). Kisilev and coworkers [KLK$^+$01] have used this method to increase the electron density contrast between lipid vesicles and the bulk water and consequently obtain stronger small angle scattering signals. For the given solution we obtain an increase of the theoretical $\Delta\delta$ from $-1.23\cdot10^{-7}$ to $-2.14\cdot10^{-7}$ [Mel09]. We can see from the fitted results in figure 7.3 that $\Delta\delta = -2.60\cdot10^{-7}$ is in the order of magnitude expected from theoretical calculation, while yielding a reasonable χ^2. From fitting series along the contour of the membrane we can show that the resolution limit does not allow for the determination of thickness values below $d = 200$ nm. The main goal of this experimental modification, namely the improvement of fringe visibility especially for the thin membrane, could not be achieved with a detectable effect.
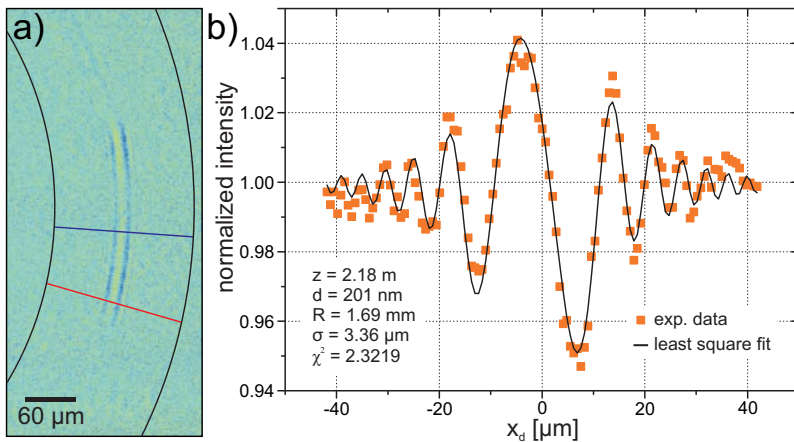
7.1.2 Middle propagation distance

Figure 7.4: *a) 2D image showing a domain of trapped solvent inside the lipid membrane. The thin regions next to it are invisible due to a lack of phase contrast between the lipid bilayer and surrounding aqueous buffer. b) As nearly all the solvent is expelled from the membrane, the fit yields a relatively small d value. Thicknesses below this value could not be achieved during the experiments due to an insufficient signal-to-noise ratio.*

The following data are taken at a distance of 2.18 m. The phase contrast image in figure 7.4(a) shows a part of the membrane where thicker regions of the membrane co-exist with invisible, i.e. thin regions, which cannot be resolved

anymore. The structure in the image corresponds to a domain of trapped solvent inside the membrane. The fitting of $I(x)$ (see figure 7.4(b)) yields a thickness of $d = 201\,$nm with a small $\chi^2 = 2.322$. Taking into account that the region around the ROI is already thinned, this value seems quite reasonable. Nevertheless, this result is hardly reproducible for other ROIs along the contour. It is extraordinary since it is the only (local) minimum of χ^2 for which the fit algorithm does not diverge. At a sudden point in the fitting process, where values comparable to the presented ones are reached, the radius R tends to increase at the expense of d, which is decreased. This corresponds to theoretical expectations but exceeds the experimental limitations when R reaches values of more than $10\,$mm. No significant changes can be observed in the fitted curve, but χ^2 slowly decreases. The conclusion can be drawn that our theoretical model of the bulged lipid membrane (see chapter 5), cannot describe the experimental circumstances in this exclusive case.
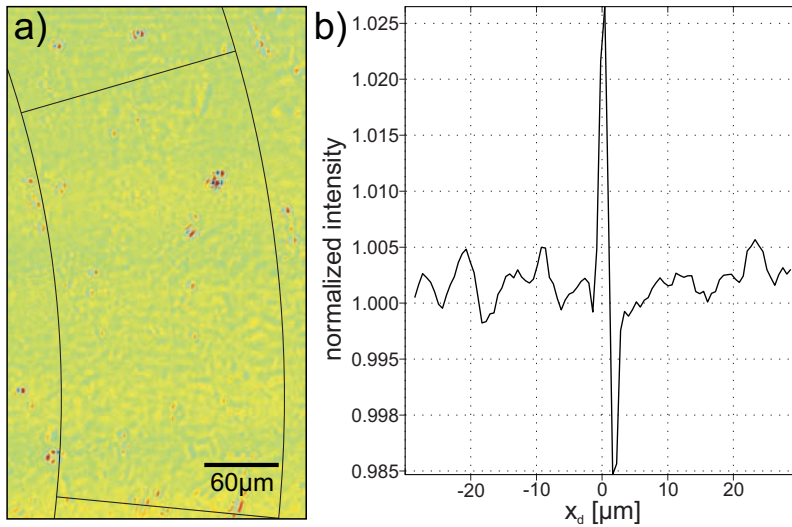
7.1.3   Short propagation distance

Figure 7.5: *a) Diffraction pattern at a propagation distance of $z = 6\,$cm. The BLM, although still in the bulk state, can hardly be resolved. No Fresnel fringe oscillations are visible. b) Due to the lack of information a quantitative evaluation of the intensity profile was not performed. The data are an average along the whole ROI between the two horizontal, black lines.*

When the sample-detector distance z_2 is decreased the images enter the direct imaging regime, which is also called the edge enhancement regime. This can be seen in figure 7.5(a), where no propagation effects, e.g. Fresnel fringes, are obtained in the diffraction pattern. In chapter 5, it was predicted that for a decrease in z an increase in the intensity $I(x, z)$ will be obtained. Experimentally this is not the case for the parallel beam imaging, where a decrease of z at the same time results in a shrinkage of the diffraction pattern. This can be observed when comparing the presented images acquired at the three imaging distances above. The loss of fringe oscillations at higher deflection angles is clearly visible due to the missing propagation of the diffraction pattern (see equation 5.1). Thus the high frequency oscillations cannot be resolved. They are smeared out due to the limited detector resolution, i.e. the finite size of the PSF. Since the amount of characteristic information in the intensity profile is poor (see figure 7.5(b)), a quantitative analysis of the data at this propagation distance is not performed.

7.1.4 Thinning of Black Lipid Membranes

Figure 7.6 reflects a membrane state in which swollen and thinned regions co-exist. It is taken at the middle propagation distance of $z = 2.18$ m, which was presented before (see figure 7.4). In the diffraction pattern the membrane contour appears like a "free arc in air". The accumulated solvent in the Plateau-Gibbs-border and the local thickness yields a strong phase contrast signal, while the thinned region towards the center of the bulged membrane is not visible. The Fresnel fringes in figure 7.6(a) appear to be axially symmetric and thus very similar to the diffraction pattern, which is expected from a single phase slit. In [Mel09] we have shown that this kind of intensity profile can be fitted by a thin phase slit model instead of the bulged membrane model presented in chapter 5. This fitting model becomes especially applicable when the membrane is very thick and the curvature is negligible in the direction of the beam, as it is the case for this image. Here the aperture is elliptic with the larger axis parallel to the propagation direction of the beam and the smaller one oriented vertically, yielding a radius $R = 580\,\mu$m of the contour. The most interesting fit parameter is the width d of the phase slit, which corresponds to the membrane thickness. Additionally, the intensity profile is dependent on the propagation distance z for which an average value $z = 2.22$ m of all single profiles was used. The same procedure is performed for the phase shift $\phi = 1.5$ rad (see equation 5.3) and the Lorentzian FWHM $\sigma = 4.46\,\mu$m. From the background corrected image (see figure 7.6(a)) twelve intensity profiles are extracted along the contour length s, while each of them is averaged over 20 radial line cuts. Figure 7.6(b) nicely visualizes the decrease of intensity oscillations towards the membrane center.
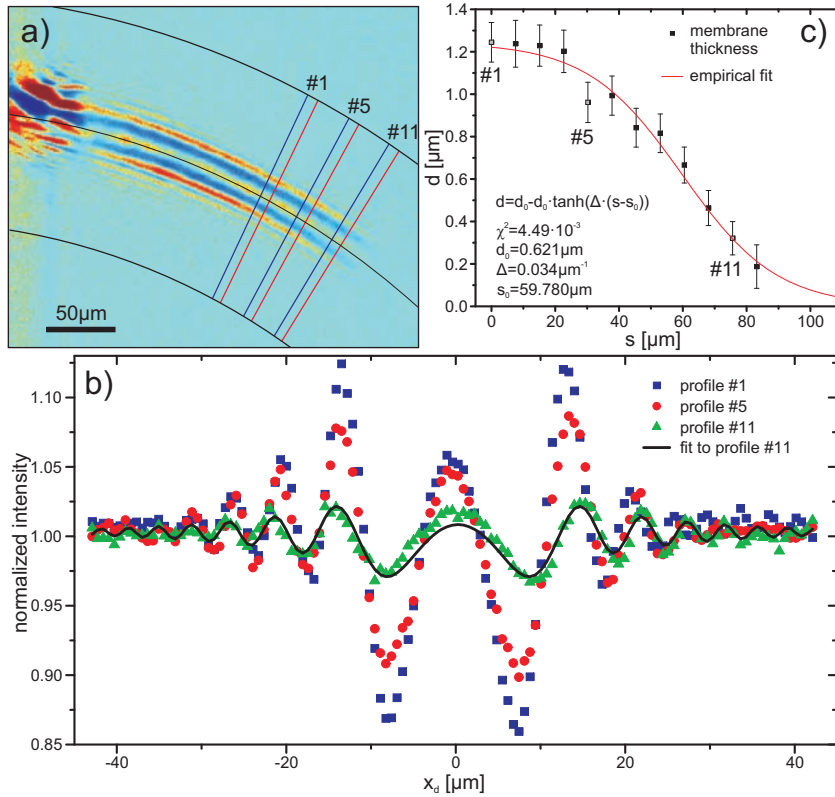
Figure 7.6: *a) Image of a bulk membrane close to the Plateau-Gibbs-border, with a series of ROIs along the membrane contour at propagation distance z = 2.18 m. The membrane is visualized during the thinning process from a swollen to a bimolecular film; the latter one cannot be resolve here. b) Intensity profiles are extracted from (a) as an average over 20 radial cuts. The thinning process progressed from the center of the bulged membrane towards the Plateau-Gibbs-border near the substrate and is accompanied by a loss of contrast in the intensity profiles. c) The decrease of membrane thickness d as determined from fits with the contour length s and an empirical fit (see equation 7.1).*

The corresponding thickness values along the contour are plotted in figure 7.6(c) and follow an empirical *tanh*-profile:

$$d = d_0 - d_0 \cdot \tanh(\Delta(s - s_0)) \tag{7.1}$$

with $d_0 = 0.621\,\mu m$, $\Delta = 0.034\,\mu m^{-1}$ and $s_0 = 59.780\,\mu m$. The fit quality is indicated by a value of $\chi^2 = 4.49 \cdot 10^{-3}$. Based on the presented theory (see figure 1.2 in chapter 2.2) the assumed geometrical model seems to be well justified. The profile is regarded as a snapshot of the co-existing swollen state, i.e two lipid monolayers separated by a reservoir of n-decane, and the bimolecular membrane with expelled solvent.

In addition to the static analysis of a single image, we have taken a time series to show the dynamics of the membrane thinning process (see supporting online material of [BMTS09]). Both temporal and spatial resolution are limited by the signal-to-noise ratio, which is in the range of 1-2 % for this imaging regime. It restricts the resolution in d to about 200 nm and allows for illumination times not shorter than about 100 ms. However, the quantitative analysis reveals information about the membrane thinning in an *in vitro* environment with a lateral resolution along the membrane contour on the micrometer scale. Considering the physiological experimental conditions this has not been achieved by any other method, such as the investigation based on visible light or electron microscopy (see chapter 1.2).

7.1.5   Partial coherence at ID10C

Figure 7.7 shows the values of $\sigma_{mag} = \Delta x$ in dependence of $\frac{z_2}{z_1}$, so that the slope should correspond to the FWHM of the source size Δs (see equation 6.1). Note that the fit range is restricted to the averaged σ_{mag} values obtained from the intensity profiles at long and middle propagation distances, since no fit values can be extracted from the short propagation distance. We obtain $\Delta s_{ID10C} = 43.1(16)\,\mu m$ for the illuminating source size. This value can be compared to the instrumental source sizes (FWHM) of 928 μm horizontally or 23 μm vertically. Interestingly, this strong anisotropy of the undulator source is not reflected in the smearing parameter Δx which varies little with the direction of the cross section (membrane orientation). Therefore, we can consider the source size derived from fitting the smearing parameter, as and effective source size determining the coherence and resolution characteristics of the phase contrast imaging. The distinction between the instrumental and the effective source size is further justified by the fact, that additional slits and optical elements between undulator and the sample act in a beam defining manner and change the coherence properties. In particular, slits are used 33 m downstream of the undulator to cut the beam to a size of 200 μm in both directions. The sample was placed 27.8 m behind this secondary source (see figure 6.1). The data treatment and the plot presented here therefore offer a practical procedure to determine and to optimize the relevant coherence and resolution properties for phase contrast imaging of a composite optical system.
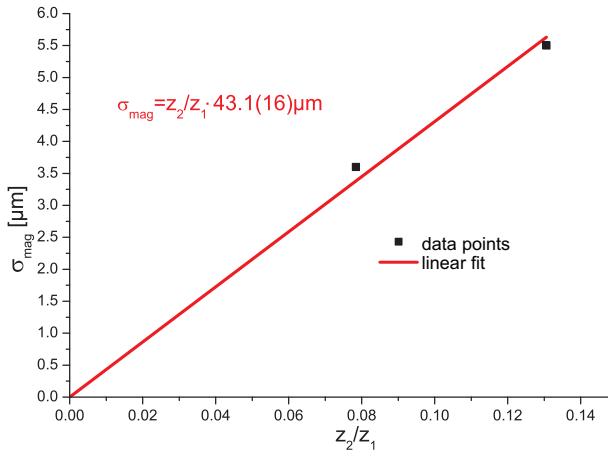
Figure 7.7: *Average of the experimental results determining the image smearing parameter σ_{mag} plotted against the propagation distance ratio z_2/z_1 for parallel beam imaging at ID10C. The predicted linear dependency (see equation 6.1) is shown, while the source size Δs is given by the slope of the linear fit. For further explanations see text. Estimated errors are about 10% of the obtained values, which result from the various number of fitted results at both propagation lengths.*

7.2   Divergent beam imaging

In the previous chapter we showed that the theory which was developed in chapter 5 can be used to describe the image formation of bulged Black Lipid Membranes in transmitted x-rays. In this section, we present quantitative and qualitative results which are obtained from divergent beam imaging at the ID22-NI undulator station (see chapter 6.1.2). In the following, a representative number of images, which were selected out of a few thousand, will be shown and discussed in more detail.

7.2.1   Bulged BLMs

We have seen that the resolution limit of the parallel beam experiments is about 200 nm. Beyond this the signal-to-noise ratio becomes significantly worse and a quantitative analysis is impossible. Note that all BLMs in this chapter are prepared from a solution of DPhyPC-n-decane in aqueous buffer solution by the "painting" method according to the preparation protocol presented in chapter 4.1.4. The fitting procedures of the related intensity profiles are performed by

using the bulged membrane slab model introduced in chapter 5 including the
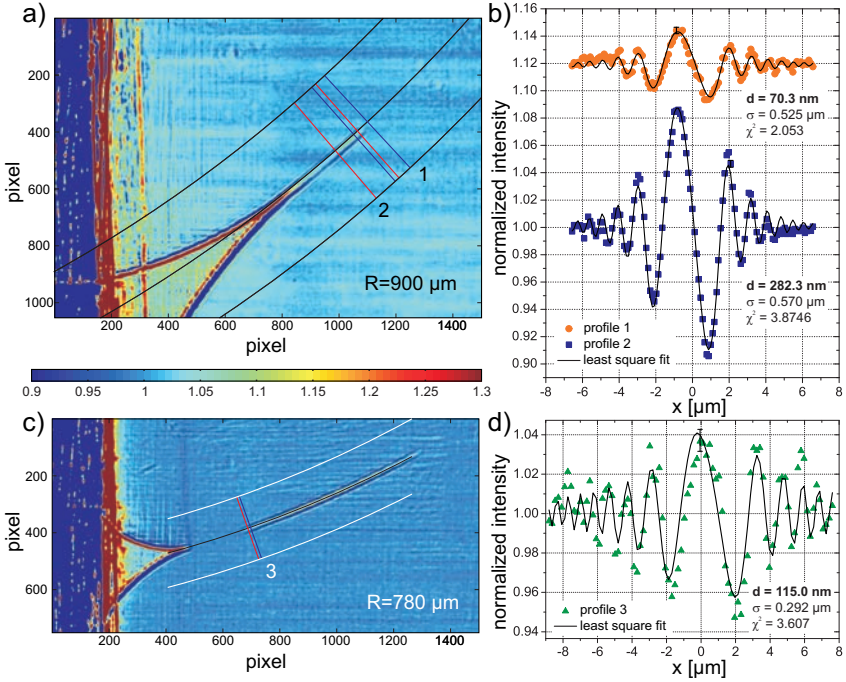theoretically calculated refractive index difference $\Delta\delta = -1.23 \cdot 10^{-7}$.

Figure 7.8: *Three intensity profiles showing the improvements in resolution
compared to figure 7.6. Images a) blm5-298-260 and c) abreakf-928-925
show parts of the thinning BLM. Profiles b) 1 and 2 and d) 3 are extracted
from ROIs, which are defined by the two black, the blue and the red lines.
The fitted membrane thicknesses can be found in the insets. See text for
further explanations. As was mentioned previously, the errors of the inten-
sity values are homogeneous along the profile. Thus, a single representa-
tive error bar is shown. In (b) intensity profiles are shifted for clarity. Pa-
rameters used for the fitting procedure are shown in table 1.*

Every intensity profile being presented in this section is labeled with a number
to simplify its identification and discussion. The radius R of the contour, which
is used in the fitting algorithm as a fixed parameter, is determined geometri-
cally from the diffraction patterns. Due to the fact that not every fit parameter
is discussed in detail for every image all relevant parameters are listed in table
1 at the end of this section in a more detailed fashion.

Figure 7.8 shows two images (a) and (c) from which we have extracted diffraction profiles (b) and (d) belonging to regions in the Black Lipid Membrane much thinner than the previously presented 200 nm. The corresponding data sets[16] are (a,b) *blm5-298-260* and (c,d) *abreakf-928-925*. Every profile in this section is labeled with a number. The fit results for every data set, which are not mentioned explicitly in the text, are given in table 1. Images were taken at effective propagation distances (a) $z_{eff} \approx 50.1$ mm and (c) $z_{eff} = 77.43$ mm, where the signal of the bimolecular membrane region is still not detectable. The fitted thicknesses are shown in the insets of figure 7.8(b) and (d). Further fit results are listed in table 1. When the images are compared to figure 7.5 it can be seen that the detector resolution is non-limiting, since the over-sampling ratio of the Fresnel fringe oscillations is much higher. In all cases z_{eff} is refined at the beginning of the fit. For *profile 1* and *profile 2* we obtain nearly the same value of z_{eff}, which also holds for σ. An explanation for the unexpected small value of $\sigma = 0.292$ in *profile 3* cannot be given. Theoretically it should increase for larger z_{eff}, i.e. in comparison to (a). Usually this is caused by an uncertainty in the fitted circle. If it does not perfectly match the contour of the membrane there will be a tilt in the straightened ROI (see chapter 6.3). Consequently, the average over the line cuts will smear out the oscillations. Since *profile 3* is only averaged over 10 line cuts this appears very unlikely. Nevertheless, the low χ^2 values show a reasonable fit precision. Figure 7.8 is designed to show how the gap in resolution between parallel and divergent beam geometry can be closed. When reaching $z_{eff} \lesssim 20$ mm an improved contrast in the thicker regions is obtained, as shown by *profile 4* (data: *blm5-986-984*) in **figure 7.9**. In table 1 it can be seen that a film thickness of $d < 10$ nm is resolved for one image, where $z_{eff} > 20$ mm. The increase in fringe visibility, as predicted by equation 5.16, becomes clear when *profile 4* is compared to *profile 3*. A maximum fringe amplitude of about 2.5% of *profile 4*, at an effective propagation distance $z_{eff} = 3.169$ mm is obtained. The membrane in this case is about 40 nm thick. For *profile 3* a much thicker region of $d = 115$ nm at $z_{eff} = 77.426$ mm shows an amplitude of about 4%, while thinner parts can hardly be resolved. When we follow the contour to the bottom left corner of figure 7.9(a), where it no longer matches the circular fit, Fresnel fringes from even thinner parts seem to be visible. A quantitative analysis of this region is impossible due to background artefacts originating from the mirror system. The following images will further emphasize the importance of background corrections.

---

[16]The first part in the notation is the filename of the image, the second one is the number of the raw object image and the third is the background/empty beam image. A table of data sets and the related filenames is given in table 1.
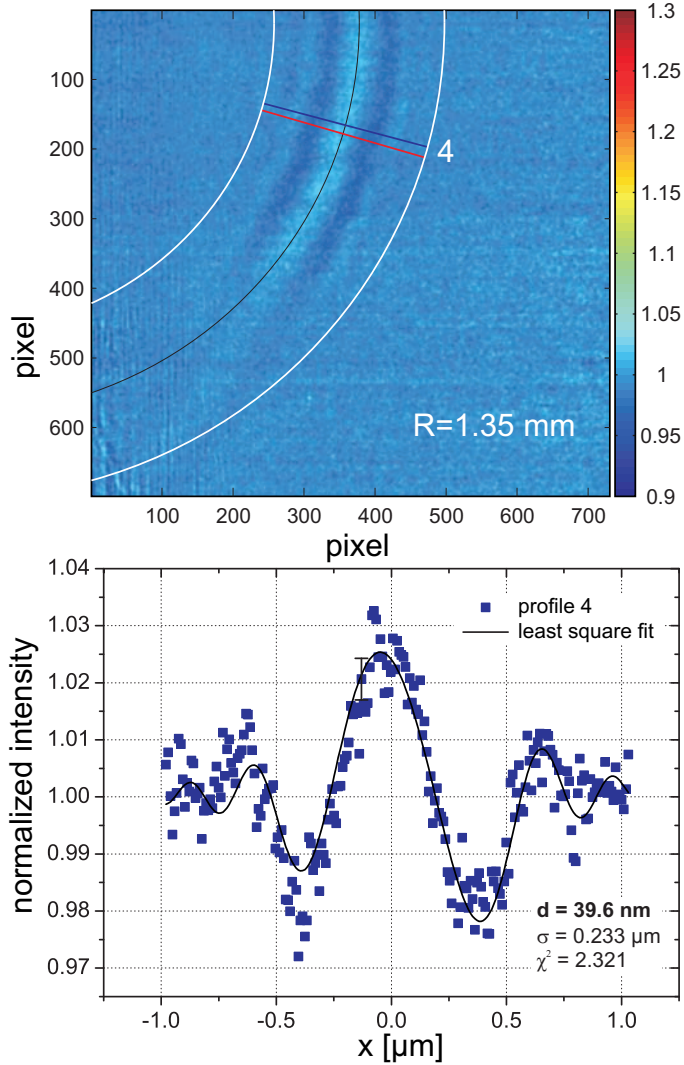
Figure 7.9: Image of a co-existing region of thick and thin BLM region. Accord-
ing to equation 5.16 the contrast at smaller propagation distances (here
$z_{eff} = 3.196$) is increased and the membrane, which in this case is 40 nm
thick, can be clearly resolved. Strong curvature of contour is due to wave
front distortions induced by the KB mirrors. Images: data: blm5-986, back-
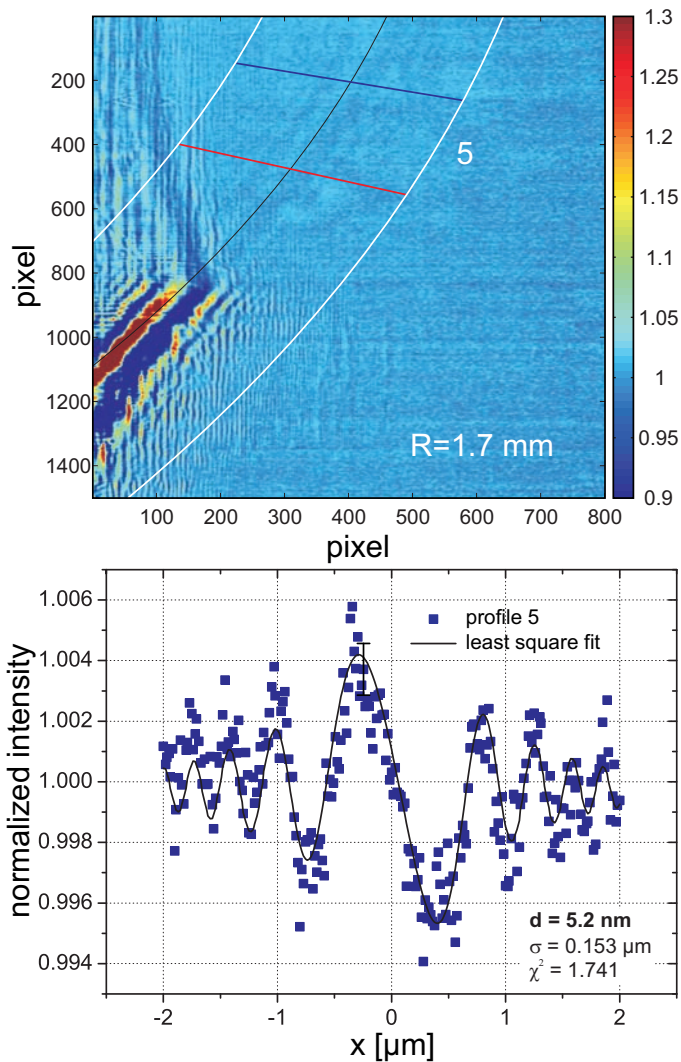ground: blm5-984.

Figure 7.10: *a) First image of a thinned Black Lipid Membrane visualized by x-ray phase contrast imaging. The membrane is prepared from a DPhyPC-n-decane solution by the "painting" method of Müller and Rudin as described in chapter 4.1.4. Experimental parameters are z_{eff} = 6.748 mm, R = 1.7 mm, M = 76.93 and illumination time 0.5 s. b) The thickness of d = 5.2 nm is in good agreement with literature values of thinned membranes. Images: data: blm5-1074, background: blm5-1073.*

Up to now we have mainly focused on improvements in resolution, which are achieved by changing the geometry of the illuminating beam.

Figure 7.10 presents the first image of a thin bimolecular Black Lipid Membrane of 5.2 nm thickness, which is visualized by phase contrast imaging in the hard x-ray regime. The effective propagation distance is $z_{eff} = 6.748$ mm and the radius is $R = 1.7$ mm. The ROI in figure 7.10(a), which was used to extract a reasonable *profile 5* (data: *blm5-1074-1073*) with minimum noise, covers a range of 270 line cuts. This is much more than in the previous profiles and one has to take care that the fringe visibility is homogeneous along the membrane contour in this part of the diffraction pattern. Nevertheless, there is still a chance that it includes contributions of slightly thinner and thicker regions. The thickness has an upper fit value of $d_{max} = 7.1$ nm (+37%) and a lower one of $d = 2.5$ nm (−52%). The main limitation here is a poor signal-to-noise ratio in the phase contrast image. Thus the errors of the intensity values are relatively large (see representative error in figure 7.10(b)). Consequently χ^2 will still give reasonable values for aforementioned variations of d.

Figure 7.11 shows the same membrane as in figure 7.10, but more strongly bulged and at a position 6 mm closer to the focus of the KB mirrors. Between the two images z_1 is reduced from 7.5 mm to 1.5 mm, This simple procedure increases the magnification by a factor of 4.75. The magnification in *profile 6* (data: *blm5-1029-1028*) is $M = 365.09$ for $z_{eff} = 1.433$ mm. The increased oversampling ratio of the Fresnel oscillations is clearly visible. We do not obtain a significant change in the fringe amplitude, which is about 4‰. The fit result for d is the same as before, as well as its upper and lower limits and the FWHM of the Lorentzian is slightly reduced from $\sigma = 0.153$ (*profile 5*) to $\sigma = 0.143$ (*profile 6*), as expected. Both intensity profiles show a linear offset in the data, which has not been corrected so far. This leads to a mismatch of the fitting curve on one or the other side of the central oscillation.

Figure 7.12 depicts another representative diffraction pattern, *profile 7* (data: *abreakf-236-235*), of a thin BLM extracted from a different measurement. The image is recorded at an effective propagation distance of $z_{eff} = 7.623$ mm, which gives a magnification of $M = 67.99$. The obtained thickness of $d = 5.7$ nm fits the results from *profile 5* and *profile 6*. $\sigma = 0.291$ is relatively large compared to *profile 5*. This results from the large ROI, which includes 803 line cuts. It can hardly be fitted by a circle, without deviating from the membrane contour. Such a large ROI is needed in this special case since mirror artefacts could not be completely eliminated by the background correction. Consequently, the noise level in *profile 7* is very high and the upper and lower errors become approximately ±60% of the absolute values.

Table 1 summarizes profile data for all our experiments, where data presented in the preceding figures are written in bold.
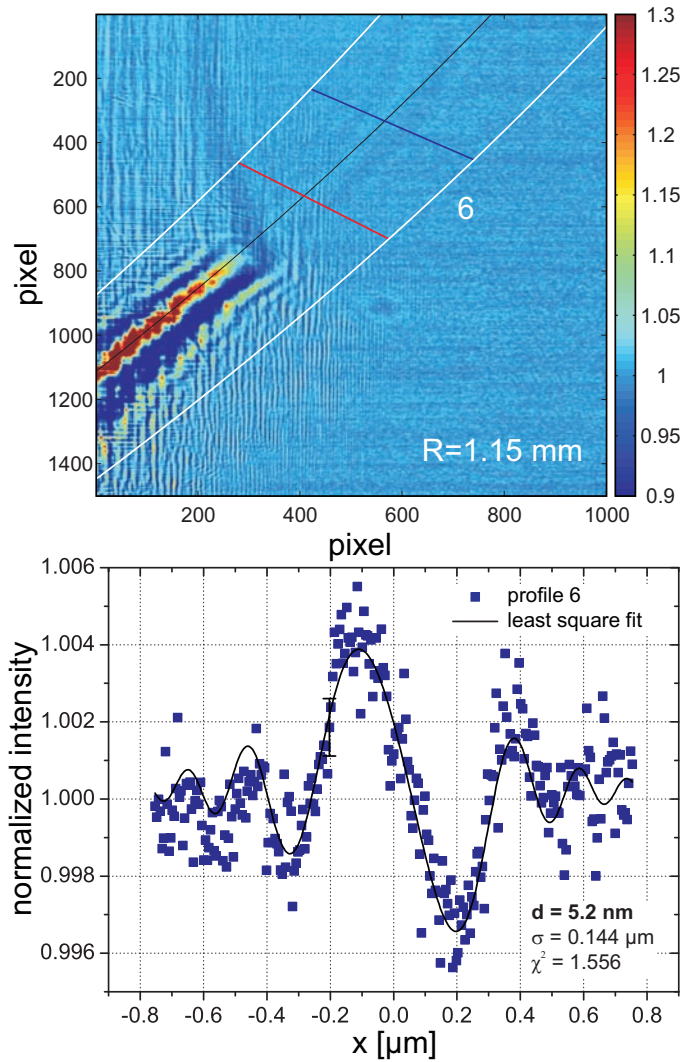
Figure 7.11: *a) The sample is moved approximately 6 mm closer to the KB focus with respect to the position in previous figure 7.10(a) yielding z_{eff} = 1.433 mm and M = 365.09. b) Profile 6 is extracted from virtually the same ROI and gives identical fit results. Images: data:* blm5-1029, *background:* blm5-1028.
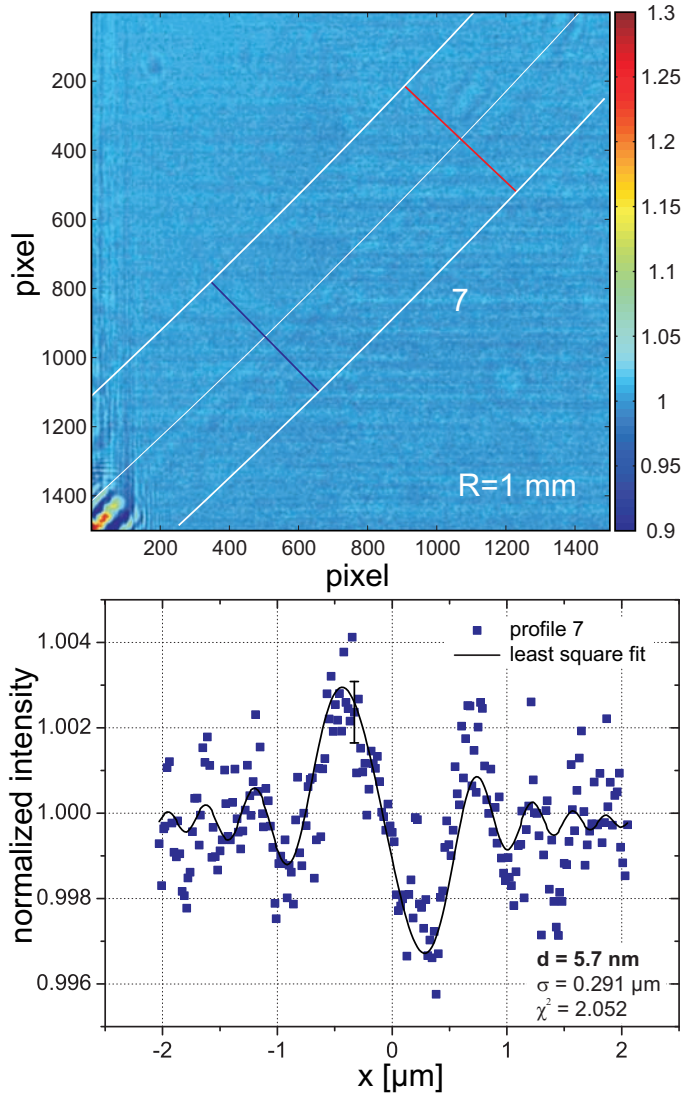
Figure 7.12: *a) Image of a thin BLM obtained from another preparation. Experimental parameters: z_{eff} = 7.623 mm, R = 1 mm and magnification M = 67.99. b) Although* Profile 7 *is average over 803 line cuts it shows a large noise level due to dominating mirror artefacts. Images: data:* abreakf-236, *background:* abreakf-235.

z_{eff} [mm]	d [nm]	M	R [mm]	σ [μm]	χ^2
0.784	4.1	669.76	1400	0.078	1.773
Profile 6: blm5/blm5_1029-1028, profile: 1, fit:124538; 0.5 s; Teflon: ø1.4 mm					
1.433	**5.2**	**366.08**	**1150**	**0.144**	**1.568**
1.676	8.1	312.90	1500	0.150	1.818
2.883	5.7	181.42	1150	0.209	2.657
3.105	3.0	168.43	1340	0.201	1.879
Profile 4: blm5/blm5_986-984, profile: 2, fit:114726; 0.5 s; Teflon: ø1.4 mm					
3.169	**39.6**	**164.98**	**1350**	**0.233**	**2.321**
3.467	7.4	150.72	1200	0.288	1.274
3.541	10.1	147.55	1200	0.248	2.738
6.336	4.3	82.01	2545	0.173	1.593
Profile 5: blm5/blm5_1074-1073, profile: 1, fit:145507; 0.5 s; Teflon: ø1.4 mm					
6.748	**5.2**	**76.93**	**1700**	**0.153**	**1.755**
Profile 7: blm5/abreakf_236-235, profile: 1, fit:164641; 0.5 s; Teflon: ø1.4 mm					
7.623	**5.7**	**67.99**	**1000**	**0.291**	**2.070**
7.802	6.0	66.40	1160	0.220	1.329
7.892	108.0	65.64	830	0.135	6.565
9.086	5.7	56.87	800	0.214	1.860
15.829	7.5	32.20	900	0.446	2.477
16.976	9.0	29.95	950	0.629	1.927
17.738	7.5	28.62	1200	0.347	2.795
17.794	8.9	28.52	1200	0.426	2.369
45.493	6.8	10.46	2500	0.356	2.753
Profile 1: blm5/blm5_298-260, profile: 3, fit:150640; 0.5 s; Teflon: ø1.4 mm					
50.037	**70.3**	**9.39**	**900**	**0.525**	**2.053**
Profile 2: blm5/blm5_298-260, profile: 1, fit:151605; 0.5 s; Teflon: ø1.4 mm					
50.143	**282.3**	**9.37**	**900**	**0.570**	**3.941**
76.336	655.7	5.68	780	0.314	10.397
Profile 3: blm5/abreakf_928-925, profile: 3, fit:111142; 0.5 s; Teflon: ø1.4 mm					
77.426	**115.0**	**5.58**	**780**	**0.292**	**3.607**

Table 1: *The table shows the fit results of 23 intensity profiles sorted by the fitted effective propagation distance z_{eff}. Additional fit parameters are thickness d and FWHM σ of the Lorentzian convolution function. The error of the fit is given by χ^2, while R was estimated geometrically and is fixed for all calculations. M is the magnification according to equation 5.20. Previously presented profiles are marked in bold.*

7.2.2 Microfluidic BLMs

In chapter 4.2 we presented a novel type of model membrane, namely the microfluidic BLM (mfBLM). We have discussed the advantages of this system and given a detailed description of its preparation. This section will summarize the results, which are obtained from phase contrast imaging using mfBLMs as an alternative to bulged BLMs in divergent beam experiments.

Figure 7.13(a) (data: *run8-1208-1408*) shows a representative diffraction pattern of a mfBLM. The film is still thick due to remaining solvent meaning that the visibility of Fresnel fringes is relatively high. Extracted *profile 8* is depicted in (b), along with a least-squares fit to the data.
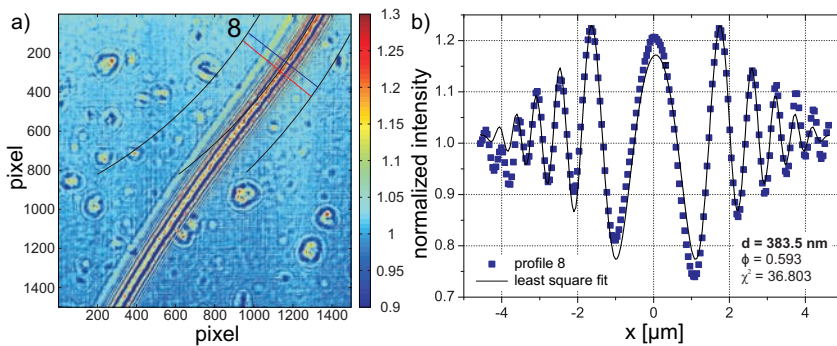
Figure 7.13: *a) Diffraction pattern of a microfluidic BLM (mfBLM) prepared from a Monoolein-squalene solution / water at an effective propagation distance of 29.67 mm. The Fresnel fringes are highly visible at high deflection angles. Glue residues at the surface of the self-adhesive kapton window material produce parasitic features in the image. b)* Profile 8 *is extracted from the ROI in (a). Due to planar sample geometry it can be fitted using a symmetric phase slit model [Mel09], which is characterized by the phase shift φ and the thickness d. Images: data:* run8-1208*, background:* run8-1408.

The symmetry of the intensity profile can be explained by the geometry of the mfBLM. A pressure gradient Δp across the membrane induced by the two pumps will always make the membrane shift inside the channel. When they are stopped the membrane will stay at a fixed position. Now $\Delta p = 0$ should hold and the membrane should favor a planar orientation to minimize its surface tension. Since it is composed of symmetric monolayers, we can explain the symmetry of the intensity pattern in the same way, as for parallel beam thinning series (see figure 7.6) by using the symmetric phase slit approach. The

thickness of $d = 383.5$ nm is large, as expected. The fit result of $\phi = 0.593$ can be used to calculate the path length of the x-rays through the membrane. According to equation 5.3 we get

$$L = \frac{\phi}{-k\,\Delta\delta} = \frac{0.593}{8.872\cdot 10^4\cdot 1.23\cdot 10^{-7}}\,\mu m = 54.341\,\mu m, \qquad (7.2)$$

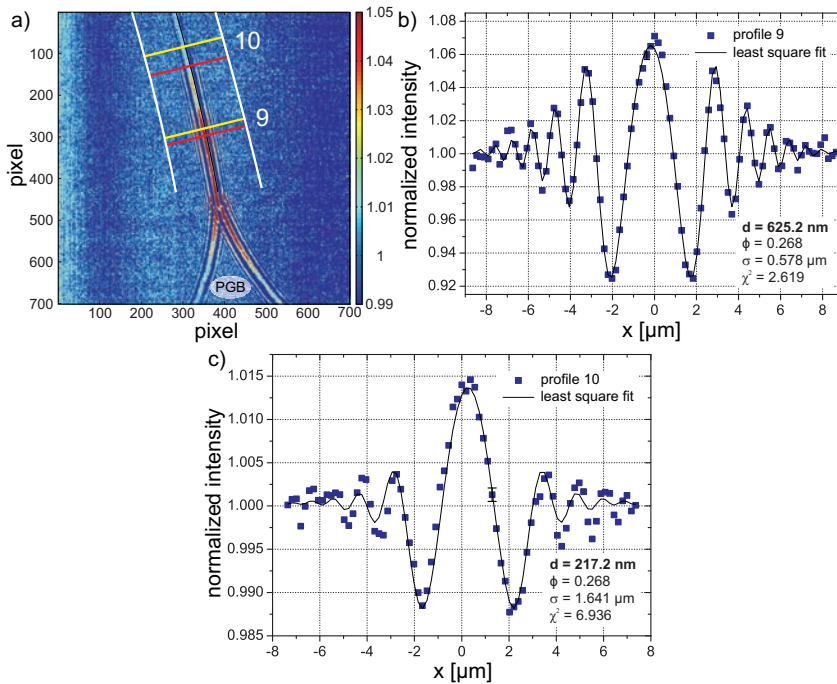which at the same time corresponds to the diameter of the membrane patch.

Figure 7.14: *a) Diffraction pattern of the transition region during the "zipper-like" effect of a microfluidic BLM (mfBLM) close to the Plateau-Gibbs border (PGB) (Monoolein-squalene / water, z_{eff} =94.21 mm). The Fresnel fringes disappear in regions where the membrane has already thinned and only a single maximum is left. b) Profile 9, along with a reasonable least-squares fit, showing a large thickness at the position of a thick, domain of residual solvent. c) Profile 10, which is located close to the bimolecular membrane region, cannot be fitted comparably accurately due to a notable contribution of the PGB to the diffraction pattern. Images: data:* hunt01-7072, *background:* hunt01-7073.

This value appears to be quite reasonable for a channel depth of 300 μm. It can be seen in figure 7.13(b) that the fit shows slight deviations from *profile 8* in the central region. It is also not able to catch the slight asymmetry of the first order minima. Consequently, the $\chi^2 = 36.803$ is still remarkably large in comparison to *profiles 1-7*. The phase contrast image in figure 7.13(a) reveals structures which are related to residues of glue on the self-adhesive kapton foil. These can induce parasitic scattering, which contributes to the diffraction pattern of the membrane and leads to deviations from the theoretical intensity profile, as obtained in *profile 8*. In the absence of glue on the kapton surface, i.e. in the experiments where bulged BLMs were investigated, such features cannot be observed.

Figure 7.14(a) (data: *hunt01-7072-7073*) shows the transition region between the Plateau-Gibbs border and the bimolecular region of an mfBLM, which has recently formed through the so-called "zipper-like" process. The fresnel fringes close to the PGB are much more strongly pronounced than in the thinner regions. *Profile 9* in figure 7.14(b) is extracted from a position in figure 7.14(a), where a domain of residual organic solvent just migrates towards the PGB. Figure 7.14(c) shows *profile 10*, which is extracted from a ROI in the transition region. Here the fringe visibility is already poor.
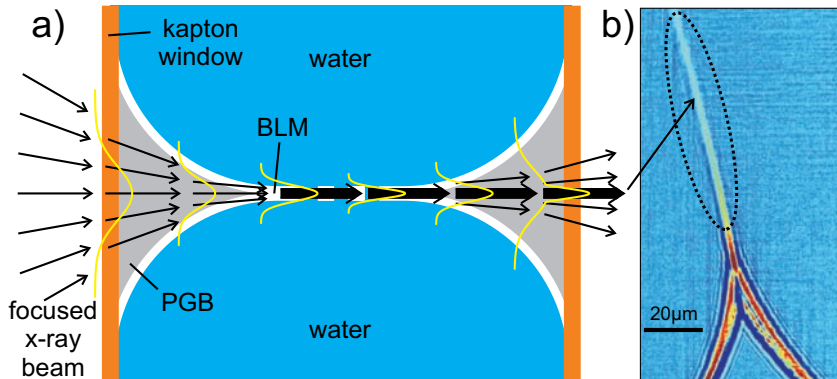
Figure 7.15: *a) Schematic representation of the "focusing" effect of the Plateau-Gibbs border. This results in an intensity maximum in (b) at the position of the thinned membrane. Images of (b): data:* hunt01-7072, *background:* hunt01-7105, *for experimental details see figure 7.14.*

Regarding the fit result of $d = 625.2$ nm for *profile 9*, it is much larger than for *profile 8*. This is due to the smaller $\phi = 0.268$, which only gives a path length $L = 24.559$ μm for the x-rays to travel through the film. Regarding *profile 10*,

which is depicted in figure 7.14(c), we obtain a dominant contribution of the central maximum. Compared to this the higher order oscillations only have little intensity. To match this strong decay the fit algorithm increases the FWHM of the Lorentzian up to $\sigma = 1.614$, while it is only $\sigma = 0.578$ in *profile 9*. Consequently, the intensity is strongly decreased, which can only be compensated by an increase in the thickness. A value of $d = 217.2$ nm is unexpectedly high for a profile at a position so close to the bilayer part of the film. However, when *profile 10* is fitted with the σ value of *profile 9*, we obtain a reasonable thickness of 78.4 nm. Except for the central maximum, the higher order fringes are fitted much more accurately with this constraint. The schematic representation in figure 7.15(a) gives a possible explanation for the intensity observed after the membrane has thinned (see figure 7.15(b)). We consider it as a "focusing" effect of the Plateau-Gibbs border. The impinging x-rays are reflected at the PGB-water interface, to be guided to the contact region of the two monolayers where they are concentrated. The resulting image at the detector can be considered as a superimposition of the diffraction pattern and the central intensity peak. The dominance of the latter is the reason why the thinned state of the mfBLM, which will show intensity variations of only 0.1 % (see 7.2.1), cannot be observed in any of the diffraction patterns.
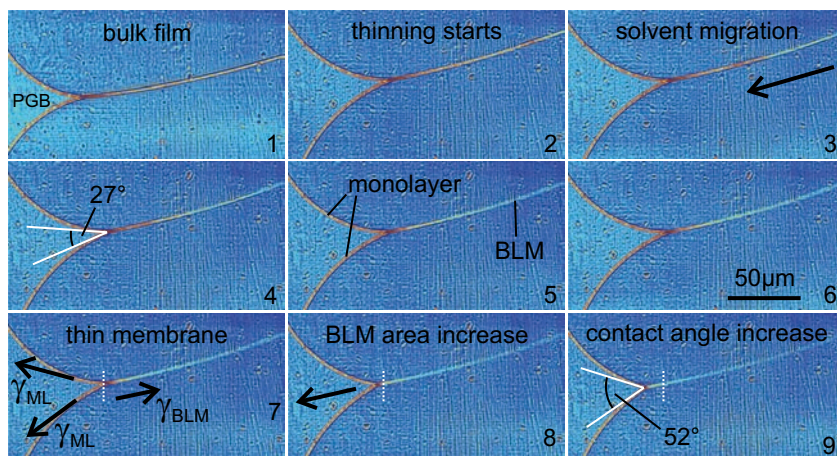

Figure 7.16: *Image series of the "zipper-like" effect, which occurs during the transformation from a bulk film (1) to a bimolecular membrane (7). The migration of solvent (2-6) and the change in contact angle between the lipid monolayers and the BLM (4,9) is shown. See text for details. Images: data: hunt01-7001, 7054, 7064, 7068, 7071, 7072, 7073, 7078, 7150, background: hunt01-10049.*

An image series of the "zipper-like" effect, which occurs during the transformation from a bulk film to a bimolecular membrane, is shown in figure 7.16. It can be nicely visualized due to the interfacial geometry in the microfluidic setup. Two monolayers of Monoolein molecules, which assemble at the squalene-water interface, get in contact and strong Fresnel fringes appear in the diffraction pattern (1). Driven first by adhesive and subsequently by van der Waals forces the domains of solvent in the gap between the two monolayers are expelled to the Plateau-Gibbs border (2-6). Finally, a thin bilayer membrane forms (7). It was discussed in chapter 2.1 that the bifacial tension of the BLM γ_{BLM} is smaller than twice the interfacial tension of the monolayers γ_{ML} (7) (see equation 2.9). Consequently a force occurs, which results in BLM expansion (8) and sets the BLM under tension (see figure 2.1). According to equation 2.10 we see that the free energy difference ΔF between two monolayers and the thinning film decreases as the contact angle increases. While it is still about 27° in the swollen state it becomes approximately 52° in the case of the bimolecular membrane (9), where ΔF reaches a minimum (see figure 2.4). For a quantitative discussion of the absolute values of ΔF, the surface tension γ_{ML} of the Monoolein monolayer at the squalene-water interface needs to be known. Considering the contact angles in (4) and (9) we can conclude that the free energy difference changes from $\Delta F = 2 \cdot \gamma_{ML} \cdot \left(\cos(\frac{27°}{2}) - 1 \right) = -0.055 \gamma_{ML}$ in (4) to $\Delta F = -0.202 \gamma_{ML}$ for the bilayer membrane in (9). When assuming interfacial tension $\gamma_{ML} \approx 1$ mN/m the absolute ΔF is in the order of magnitude of the value obtained from the free energy plot in figure 2.4.

7.2.3 Partial coherence at ID22NI

Figure 7.17 shows the values of σ_{mag} plotted against Δs on $\frac{z_2}{z_1}$, which are extracted from divergent beam imaging experiments performed at ID22NI. The slope of the graph in figure 7.17 according to equation 6.1 is $\Delta s_{ID22} = 188(12)$ nm. For the underlying experiments this value fits the dimension of the KB focus, which was measured to be 130 nm in diameter. Consequently, the fitted σ values seem to be in good agreement with the expected values. A potential explanation for slight disagreement in the σ values is that the given values are averaged over all membrane orientations, while the size of the KB focus is only known for the vertical and horizontal direction. It is more likely that the coherence length in every other direction is larger and thus the smearing, i.e. σ, is increased. An improvement to reduce potential uncertainties in σ, which also have an influence on the fitting quality of the intensity profiles, could be achieved by determining σ from a priori known test structures with defined geometries. Subsequently, the obtained values can be used as a fixed parameter in the fitting procedure.
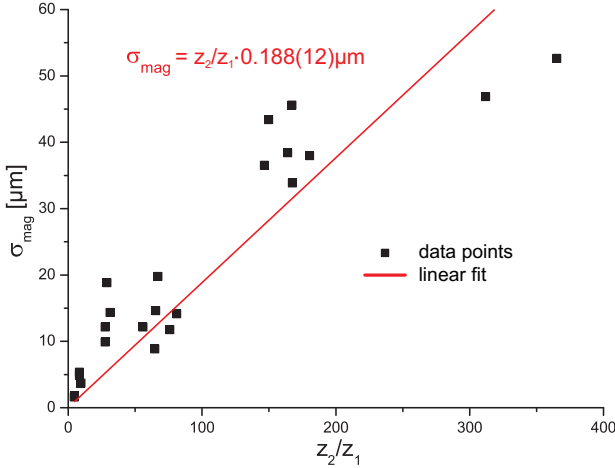
Figure 7.17: *The image smearing parameter σ_{mag} plotted against the propagation distance ratio z_2/z_1 for divergent beam geometry at ID22NI. The predicted linear dependency (see equation 6.1) is shown, while the source size Δs is given by the slope of the linear fit. Error bars are not depicted, but a mean error is estimated to be approximately 50% of the absolute values.*

7.3 Discussion

From a comparison of the results obtained with parallel and divergent beam imaging, improvements in resolution become obvious. In summary, the experiments show a much higher sensitivity to smaller phase changes and, thus, an increase in resolution at decreasing z_{eff}, as it was achieved in the divergent beam imaging. This is in perfect agreement with the theoretical predictions in chapter 5.

A systematic increase of χ^2 is obtained for higher propagation distances. This results from the smaller relative errors of the intensity profiles for thicker membrane regions. Errors which are large relative to small intensity values will consequently give better fit qualities. This fact must be regarded when discussing the values of χ^2.

At the beginning of the fitting procedure the effective propagation distance z_{eff} is refined and the obtained values are always about 10% smaller than the measured ones. The reason for this is still unclear, but it should have an effect on the calculation, because a smaller z_{eff} yields a smaller effective pixel size and, consequently, the intensity profile will shrink. This point was not included in the evaluation of the data so far.

However, two facts do need to be emphasized here. The first one is that the diffraction signal of the bilayer region is stable and does not disappear over recording times of up to 30 minutes, as is the case for swollen membranes.
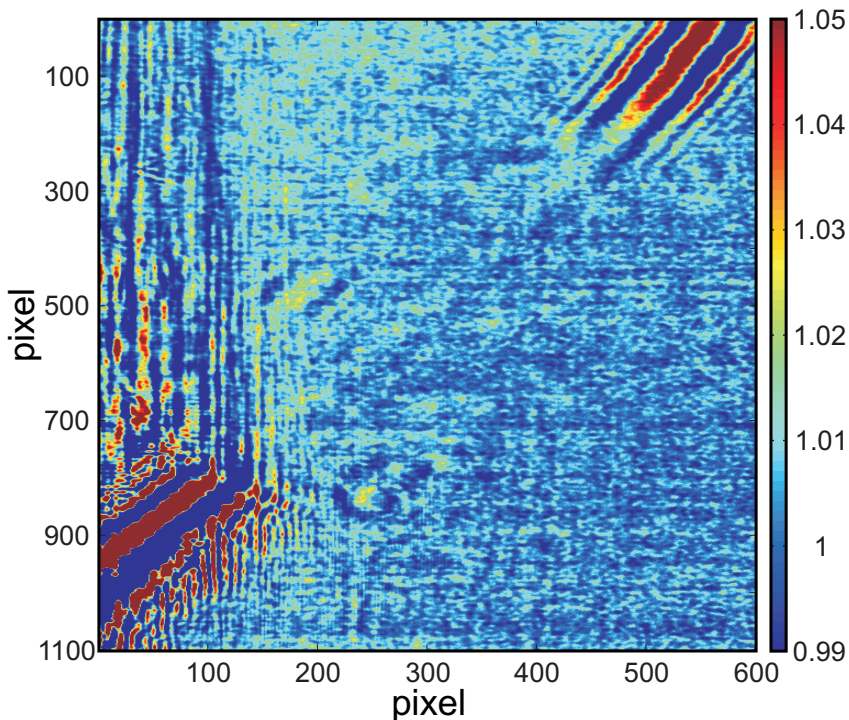

Figure 7.18: *Interference artefacts which originate from the KB mirrors in the divergent beam experiments show a strong contribution to the diffraction patterns, although an empty beam correction is performed. Consequently, the signal-to-noise ratio is decreased and the resolution of thinned Black Lipid Membrane regions becomes almost impossible. Images: data:* abreakf-175*, background:* abreakf-172.

Thus, it represents the final state of the membrane a long time after the thinning has taken place. Therefore we can be sure that the images show a thinned bilayer membrane. Furthermore, the determined film thicknesses, in the range from 5 nm to 9 nm for the thinned regions (see table 1), are in perfect agreement with the values reported in the references cited in chapter 1.2 [TD66, Tie67b, HT68, Whi70, AMH70, Whi80]. Experiments which have used x-ray reflectivity studies on solid supported lipid bilayers report a head to head distance of

4 nm for fully hydrated membrane stacks made from diphytanoylphosphatidyl-choline [WHLH95]. A reason for the different values of d may be the underlying model of constant electron density, which is described in chapter 5. This will not hold anymore for the case of a thin lipid bilayer, where there will be different scattering contributions from headgroups and hydrocarbon chains. A more complex model structure has to be implemented.

Our experiments cannot answer the question about the amount of organic solvent, which is postulated to always remain in between the two lipid monolayers (see chapter 2.4). This would also result in larger membrane thicknesses.

The relatively large errors of the fit values originate from the poor image quality after background correction. The very weak phase contrast signals of only 0.1 % become dominated by the remaining mirror artefacts. Figure 7.18 shows the contour of a thin BLM. Its diffraction pattern is heavily disturbed by parasitic scattering consisting of regularly spaced vertical and horizontal lines. Consequently, the signal-to-noise ratio in the intensity profiles is reduced and larger fit errors are obtained (see e.g. *profile 7* in figure 7.12). The use of x-ray waveguides in our recent experiments on cells circumvents this experimental problem [GKK+10], since the waveguides produce a much more homogeneous far field. Another solution could be the accumulation of more, but briefer, illuminations, alternately taking object and background images. This would reduce the time dependent shift between two images. Subsequently they are summed up, and the correction is performed.

Finally it should be pointed out that no beam damage is observed during the experiments. This is always an important issue when, on reaching a critical flux density, the degeneration of the sample can take place. In the focused beam experiments the BLMs are stable even when they were translated through the KB mirror focus, where they are exposed to a flux density of $10^{19}\frac{\text{photons}}{\text{mm}^2\,\text{s}}$.

The resolution of membranes thicknesses d on nanometer length scales confirms that potential undulations must be much smaller than d or much slower than the maximum accumulation time of 1 s. This is in good agreement with the previously discussed predictions (see chapter 2.1) from literature, which state that the thermal fluctuations are suppressed by the relatively high surface tension of BLMs [HBRS98, Tie67a, Tie68b, MSS+09]. If there was a contribution of undulations in the BLM, it might result in a smearing of the spherical cap, which consequently leads to an increase in the observed membrane thickness. But, as it is shown by the perfect agreement of the theoretical model and the experimental data, the contributions of undulations must be small enough that the model assumptions still hold.

We have presented efforts to increase the contrast and thus the visibility of the thinned bilayers by compositional modification of the experimental model

membrane system. These approaches did not shown a remarkable effect. A great advance, which was already presented in chapter 5.1, is achieved by using bulged BLMs. By raising the radius of curvature, the accumulated phase of the x-rays inside the BLM is easily increased by a factor of two (see figure 5.4). In future experiments the visualization and resolution of thinned BLMs can take advantage of this effect next to the experimental improvements and developments of the imaging setup, which are discussed in the following outlook.

8 Conclusions and outlook

We have used x-ray phase contrast imaging to study the structure and dynamics of Black Lipid Membranes. Our experimental results are in perfect quantitative agreement with the numerical simulation of the imaging mechanism. To this end, we have solved the direct imaging problem with a remarkable resolution and without further use of phase retrieval algorithms. In contrast to thickness determinations from reflected light and capacitance experiments, the high lateral resolution of this novel application of phase contrast imaging to BLMs enables a differentiation between the thin lipid bilayer and regions of larger thickness.

We can conclude that we have visualized for the first time an unstained, thinned bimolecular film of thickness on the nanometer scale by the use of partially coherent x-rays in a divergent beam geometry. It is important to stress that this imaging scheme is fully compatible with hydrated biomolecular samples in excess solution. The setup and system show high stability in x-ray beams, without the typical effects of radiation induced damage observed for solid supported membranes. The presented experimental scheme is therefore well-suited for the *in vitro* study of biologically more complex samples.

Further progress in the structural analysis of thinned lipid bilayers beyond the proof-of-concept experiments presented here could be reached by experimental improvements, including dedicated instrumentation, detectors, and coherence optimized optics. Above all, the development of highly coherent, bright x-ray sources, i.e. free electron lasers, and the progress in the design of x-ray optics, especially small x-ray waveguides [SKFB08, GNK+10, KGK+10], will be the key to increasing phase contrast signals and thus a resolution high enough to resolve molecular details of membrane.

Matched to these experimental improvements to resolve more structural details, a generalization of the electron density model used for the data analysis, beyond a simple hydrophobic sheet, would be a necessary and straightforward extension of this work. An improved model could be composed for example of three Gaussians, two representing the lipid head groups and the third one the hydrocarbon region.

We expect further improvements of data evaluation by the application of advanced phase retrieval algorithms based on the approaches which were presented by Langer [LPGP08] and Nugent [NGC+96]. The first result of using such an improved Gerchberg-Saxton algorithm for the reconstruction of Fresnel imaging data has recently been shown by our group [GKK+10]. However, for the underlying sample geometry of bulged Black Lipid Membranes the film thickness will always be encoded in the projected transmission function. Due to this fact, the solution of the direct problem with a maximum of three fitting

parameters has proved to be the most robust way.

For the direct access to the membrane thickness, with a reduced number of fitting parameters, an experimental setup was presented for the planar imaging of lipid bilayers in microfluidic devices. From the presented results, using this novel type of membrane system, we have seen that the theoretical model might have to be adapted to correct for the contributions of the PGB to the diffraction images.

The investigation of the influence of electric fields on the structure of lipid membranes has shown that the detectable thickness changes are in the order of the achievable resolution. These variations in the layer structure follow the predictions of Burgess [BLH+04, BLH+05] but in much smaller dimensions. Regarding the electric field unbinding, the experiments have shown to be in perfect agreement with Burgess and Charitat and colleagues [LFC06, CLF08]. The influences of the supporting substrate remain unclear and need to be investigated in future experiments. Thus, we propose the study of the electric field effects on membrane structure in the absence of the solid substrate, which, as we have discussed before, always induces perturbations of the lipid system. Our approach of structural determination based on the imaging of bulged and freestanding, i.e. electrophysiologically accessible, membranes is well suited for studies of the influence of electric fields, which will be applied in the next investigations.

In future, the improvement of experimental conditions may also enable the generation of tomograms, in which the membrane is rotated in the beam. We have shown image series along the contour, which can then be used to perform a 3D reconstruction of the bulged lipid bilayer with corresponding thickness values.

As a next step, we will use giant unilamellar vesicles (GUVs), as a solvent free membrane system, for high resolution studies of the interactions and fusion of lipid bilayers in microfluidic devices. It was not presented in this thesis, but microfluidic setups enable electrophysiological investigations of lipid membranes. A combination of these two techniques will enable the investigation of membrane-membrane interactions in electric fields with high a spatial resolution. Future experiments on protein-membrane and protein-protein interaction, as well as improved studies of membrane-colloid interactions [Nov08] are proposed.

As it was nicely stated in references [DFH82, FFI03] there is a need of alternative, high resolution techniques to investigate sub-molecular structures of membranes and the proteins that are embedded in them. The present work could hopefully contribute to this interdisciplinary effort.

A Appendix

A.1 List of abbreviations and physical parameters

A	:	membrane area
α	:	deflection angle
B	:	absorption coefficient
BLM	:	Black Lipid Membrane
c	:	ionic concentration
c_m	:	specific membrane capacitance
C_m	:	membrane capacitance
d	:	membrane thickness
d'	:	solvent layer thickness
D	:	diffusion coefficient
DOPC	:	1,2-dioleoyl-sn-glycero-3-phosphocholine
DOPS	:	1,2-dioleoyl-sn-glycero-3-phospho-L-serine
DPhyPC	:	1,2-diphytanoyl-sn-glycero-3-phosphocholine
DPPC	:	1,2-dipalmitoyl-sn-glycero-3-phosphocholine
DPPS	:	1,2-dihexadecanoyl-sn-glycero-3-phospho-L-serine
E	:	electromagnetic field
e_0	:	elementary charge
F	:	surface free energy
I	:	intensity
k_B	:	Boltzmann constant
L	:	path length through membrane
M	:	magnification
mfBLM	:	microfluidic BLM
N_A	:	Avogadro's number
n_e	:	electron density number
n_m	:	molecular surface density
p	:	pressure acting on membrane
P	:	permeability
PCI	:	phase contrast imaging
PDMS	:	poly(dimethylsiloxane)
PGB	:	Plateau-Gibbs border
Q	:	charge
R	:	bulged membrane radius
r	:	particle radius

R_c	:	gas constant
r_m	:	specific membrane resistance
R_m	:	membrane resistance
R_S	:	Stoke´s friction
r_0	:	classical electron radius
s	:	length of surfactant molecule
SSM	:	solid supported membrane
$T(x)$	:	transmission function
U_s	:	steric repulsion potential
U_v	:	electrocompression potential
U_{vdw}	:	attractive van der Waals potential
V_m	:	transmembrane potential
z	:	ion valency
Z	:	atomic number
z_1	:	source-sample distance
z_2	:	sample-detector distance
z_{eff}	:	effective sample-detector distance
Δs	:	FWHM of source size (Gaussian shape)
Δx	:	smearing parameter, equivalent to σ_{mag}
ε_m	:	dielectric constant of membrane
ε_0	:	permittivity
γ_{BLM}	:	interfacial / "bifacial" tension of BLM
γ_{ML}	:	interfacial tension of lipid monolayer
η	:	viscosity
θ	:	contact angle between bulk and bimolecular film
λ	:	photon wavelength
φ	:	electric potential
Φ	:	ion flux density
ν	:	velocity
ξ_l	:	transverse coherence length
ρ	:	electron density
σ	:	Lorentzian FWHM in demagnified coordinates
σ_{mag}	:	Lorentzian FWHM in magnified coordinates
ϕ	:	phase shift
ω	:	angular frequency

A.2   Tools for reflectivity data extraction from 2D images

eval_config.m

```
1   % this file contains all the variables that belong to the evaluation of one
2   % dataset
3
4   % FILE SYSTEM PARAMETERS
5   % folder containing the data structure acquired at the MS-SLS
6   project_folder = 'Y:\Messzeiten\2009\MS_PSI_Juni_2009_blm_refl_20081059\ebilayer_20090610';
7   p.project_folder = project_folder;
8
9   % relative path to the spec scan logs; path is to be relative to the
10  % project folder
11  speclogs_path = '/spec/scanlogs/';
12  p.speclogs_path = speclogs_path;
13
14  % name of the scanlog files
15  scanlog_prefix = 'noname_scan';
16  p.scanlog_prefix = scanlog_prefix;
17  scanlog_postfix = '_log.dat';
18  p.scanlog_postfix = scanlog_postfix;
19
20  % relative path to the detector images; path is to be relative to the
21  % project folder
22  image_path = '/pixel/images/';
23  p.image_path = image_path;
24
25  % images filename
26  image_prefix = 'image_';
27  p.image_prefix = image_prefix;
28  image_postfix = '.img';
29  p.image_postfix = image_postfix;
30
31
32  % DATA EVALUATION PARAMETERS
33  % scans belonging to dataset
34  scans = [1165 1166 1167 1168 1169 1170 1171 1172 1173];
35  p.scans = scans;
36
37  % size of the ROI inside which the program will look for the specular peak
38  roi_scan_size_y = 20;
39  p.roi_scan_size_y = roi_scan_size_y;
40  roi_scan_size_x = 20;
41  p.roi_scan_size_x = roi_scan_size_x;
```

main.m

```
1   % this is the main evaluation script
2
3
4   % load parameters for the dataset to be evaluated
5   % eval_config;
6   addpath('scans_882_890/');
7   eval_config_882_890;
8
9   % switches
10  select_datapoints_switch = 1;
11  select_ROIs_switch = 1;
12  read_scanlogs_switch = 1;
13
14
15
16  if select_datapoints_switch == 1
17  % parameter
18      dummy = struct([]);
19      data = struct('calibration_images_info',dummy);
20  else
21      load(['data_scans_' num2str(p.scans(1)) '-' num2str(p.scans(end)) '.mat']);
22  end
23
24
25  % read in the scandata into a matlab cell; see function for details
26  if read_scanlogs_switch == 1
27      scandata = readscanlogs(p);
28  else
29      load(['scan_data_scans_' num2str(p.scans(1)) '-' num2str(p.scans(end)) '.mat']);
30  end
31
```

```
32  % select the images with mouse that will be used to track the movement of
33  % the specular peak; for details see function SELECT_DATAPOINTS
34  if select_datapoints_switch == 1
35      data.calibration_images_info = select_datapoints(scandata,p);
36  end
37
38  % data.lin_regression = fit_max_positions(data,p);
39
40  if select_ROIs_switch == 1
41  data.ROIs = background_peak_selection(data,p);
42  end
43
44  for index1 = 1:length(scandata)
45      scandata{index1}.extracted = extract_intensity_data(index1,scandata,data,p);
46  end
47
48
49  save(['data_scans_' num2str(p.scans(1)) '-' num2str(p.scans(end)) '.mat'],'data');
50  save(['parameters_scans_' num2str(p.scans(1)) '-' num2str(p.scans(end)) '.mat'],'p');
51  save(['scandata_scans_' num2str(p.scans(1)) '-' num2str(p.scans(end)) '.mat'],'scandata');
```

calc_refl_curve_merge.m

```
1   function val = calc_refl_curve_ab(scandata,p)
2
3   close all;
4
5   % refl_plot:
6   % this function plots the reflection curve for the selected dataset
7
8   % plot colors:
9   plot_colors = ['b','g','r','c','m','y','k','w'];
10
11
12  %%%%%%%%%%%%%%%%%%%%%%%%%%%%%%%%%%%%%%%%%%%%%%%%%%%%%%%%%%%%%%%%%%%%%%%%%%%%%%%%
13  % Calculate Corrected Reflectivity Curve for the fixed ROI Selection
14  %%%%%%%%%%%%%%%%%%%%%%%%%%%%%%%%%%%%%%%%%%%%%%%%%%%%%%%%%%%%%%%%%%%%%%%%%%%%%%%%
15  for index1 = 1:length(scandata)
16      filter = 1./(scandata{index1}.transm);
17      monitor = 1./(scandata{index1}.mon);
18      summed_intensity = scandata{index1}.extracted.peak_count_sum;
19      background_intensity = (scandata{index1}.extracted.background_count_mean_1 + scandata{index1}.extracted.
            background_count_mean_2)/2;
20      roi_pixel_number = scandata{index1}.extracted.roi_pixel_count;
21
22      corr_intensity = monitor .* filter .* (summed_intensity - background_intensity .* roi_pixel_number);
23
24      % normalize intensity of subsequent scan to the previous scan
25      if index1 ~= 1
26          if index1 == 2
27          corr_intensity = corr_intensity .* scandata{index1-1}.extracted.roi_corr_intensity(end)/corr_intensity(2);
28          elseif index1 == 6
29          corr_intensity = corr_intensity .* scandata{index1-1}.extracted.roi_corr_intensity(end-2)/corr_intensity(1);
30          elseif index1 == 8
31          corr_intensity = corr_intensity .* scandata{index1-1}.extracted.roi_corr_intensity(end-4)/corr_intensity(1);
32          else
33          corr_intensity = corr_intensity .* scandata{index1-1}.extracted.roi_corr_intensity(end-1)/corr_intensity(1);
34          end
35      end
36
37      scandata{index1}.extracted.roi_corr_intensity = corr_intensity;
38  end
39
40
41  %%%%%%%%%%%%%%%%%%%%%%%%%%%%%%%%%%%%%%%%%%%%%%%%%%%%%%%%%%%%%%%%%%%%%%%%%%%%%%%%
42  % Plot Reflectivity Curve for the fixed ROI Selection
43  %%%%%%%%%%%%%%%%%%%%%%%%%%%%%%%%%%%%%%%%%%%%%%%%%%%%%%%%%%%%%%%%%%%%%%%%%%%%%%%%
44  figure(1);
45  index1 = 1;
46      final_roi_corr_intensity = scandata{index1}.extracted.roi_corr_intensity(1:end-1);
47      final_oh = scandata{index1}.oh(1:end-1);
48
49  for index1 = 2:length(scandata)
50      if index1 == 2
51      final_roi_corr_intensity = cat(1,final_roi_corr_intensity,scandata{index1}.extracted.roi_corr_intensity(2:end-2));
52      final_oh = cat(1,final_oh,scandata{index1}.oh(2:end-2));
53      elseif index1 == 6
54      final_roi_corr_intensity = cat(1,final_roi_corr_intensity,scandata{index1}.extracted.roi_corr_intensity(2:end-1));
55      final_oh = cat(1,final_oh,scandata{index1}.oh(2:end-1));
56      elseif index1 == 8
```

```
57        final_roi_corr_intensity = cat(1,final_roi_corr_intensity,scandata{index1}.extracted.roi_corr_intensity(2:end-2));
58        final_oh = cat(1,final_oh,scandata{index1}.oh(2:end-2));
59      elseif index1 == 9
60        final_roi_corr_intensity = cat(1,final_roi_corr_intensity,scandata{index1}.extracted.roi_corr_intensity(2:end-2));
61        final_oh = cat(1,final_oh,scandata{index1}.oh(2:end-2));
62      else
63        final_roi_corr_intensity = cat(1,final_roi_corr_intensity,scandata{index1}.extracted.roi_corr_intensity(1:end-2));
64        final_oh = cat(1,final_oh,scandata{index1}.oh(1:end-2));
65      end
66    end
67
68    semilogy(final_oh,abs(final_roi_corr_intensity), plot_colors(1))
69    hold on;
70
71    %% plot data for thresholded ROI
72    for index1 = 1:length(scandata)
73      filter = 1./(scandata{index1}.transm);
74      monitor = 1./(scandata{index1}.mon);
75      summed_intensity = scandata{index1}.extracted.threshold_roi_count;
76      background_intensity = (scandata{index1}.extracted.background_count_mean_1 + scandata{index1}.extracted.
                background_count_mean_2)/2;
77      roi_pixel_number = scandata{index1}.extracted.threshold_roi_pixel_number;
78
79      corr_intensity = monitor .* filter .* (summed_intensity - background_intensity .* roi_pixel_number);
80
81      % normalize intensity of subsequent scan to the previous scan
82      if index1 ~= 1
83        if index1 == 2
84          corr_intensity = corr_intensity .* scandata{index1-1}.extracted.threshold_corr_intensity(end)/corr_intensity(2);
85        elseif index1 == 6
86          corr_intensity = corr_intensity .* scandata{index1-1}.extracted.threshold_corr_intensity(end-2)/corr_intensity(1);
87        elseif index1 == 8
88          corr_intensity = corr_intensity .* scandata{index1-1}.extracted.threshold_corr_intensity(end-4)/corr_intensity(1);
89        else
90          corr_intensity = corr_intensity .* scandata{index1-1}.extracted.threshold_corr_intensity(end-1)/corr_intensity(1);
91        end
92      end
93
94      scandata{index1}.extracted.threshold_corr_intensity = corr_intensity;
95    end
96    % hold off;
97
98    %%%%%%%%%%%%%%%%%%%%%%%%%%%%%%%%%%%%%%%%%%%%%%%%%%%%%%%%%%%%%%%%%%%%%%%%%%%%%
99    % Plot Reflectivity Curve for the thresholded/selected ROI Selection
100   %%%%%%%%%%%%%%%%%%%%%%%%%%%%%%%%%%%%%%%%%%%%%%%%%%%%%%%%%%%%%%%%%%%%%%%%%%%%%
101   index1 = 1;
102       final_threshold_corr_intensity = scandata{index1}.extracted.threshold_corr_intensity(1:end-1);
103
104   for index1 = 2:length(scandata)
105     if index1 == 2
106       final_threshold_corr_intensity = cat(1,final_threshold_corr_intensity,scandata{index1}.extracted.
                threshold_corr_intensity(2:end-2));
107     elseif index1 == 6
108       final_threshold_corr_intensity = cat(1,final_threshold_corr_intensity,scandata{index1}.extracted.
                threshold_corr_intensity(2:end-1));
109     elseif index1 == 8
110       final_threshold_corr_intensity = cat(1,final_threshold_corr_intensity,scandata{index1}.extracted.
                threshold_corr_intensity(2:end-2));
111     elseif index1 == 9
112       final_threshold_corr_intensity = cat(1,final_threshold_corr_intensity,scandata{index1}.extracted.
                threshold_corr_intensity(2:end-2));
113     else
114       final_threshold_corr_intensity = cat(1,final_threshold_corr_intensity,scandata{index1}.extracted.
                threshold_corr_intensity(1:end-2));
115     end
116   end
117
118   semilogy(final_oh,abs(final_threshold_corr_intensity), plot_colors(3))
119   hold off;
120
121   %%%%%%%%%%%%%%%%%%%%%%%%%%%%%%%%%%%%%%%%%%%%%%%%%%%%%%%%%%%%%%%%%%%%%%%%%%%%%
122   % Format and save reflectivity courves
123   %%%%%%%%%%%%%%%%%%%%%%%%%%%%%%%%%%%%%%%%%%%%%%%%%%%%%%%%%%%%%%%%%%%%%%%%%%%%%
124   tmp=[2*final_oh,abs(final_roi_corr_intensity)];
125   save(['reflectivity_roi_' num2str(p.scans(1)) '-' num2str(p.scans(end)) '.txt'],'tmp','-ascii')
126
127   tmp=[2*final_oh,abs(final_threshold_corr_intensity)];
128   save(['reflectivity_th_' num2str(p.scans(1)) '-' num2str(p.scans(end)) '.txt'],'tmp','-ascii')
```

References

[AH68]   D.M. Andrews and D.A. Haydon. Electron microscope studies of lipid bilayer membranes. *Journal of Molecular Biology* **32**, 149 (1968).

[AL78]   O. Alvarez and R. Latorre. Voltage-dependent capacitance in lipid bilayers made from monolayers. *Biophysical Journal* **21**, 1 (1978).

[Alb94]   B. Alberts. *The Cell.* Garland (1994).

[ALS03]   G. Adam, P. Läuger, and G. Stark. *Physikalische Chemie und Biophysik.* Springer (2003).

[AMH70]   D. M. Andrews, E. D. Manev, and D. A. Haydon. Composition and energy relationships for some thin lipid films, and the chain conformation in monolayers at liquid-liquid interfaces. *Special Discussions of the Faraday Society* **1**, 46 (1970).

[AN01]   J. Als-Nielsen. *Elements of Modern X-Ray Physics.* Wiley (2001).

[ARW$^+$09] S. Aeffner, T. Reusch, B. Weinhausen, , and T. Salditt. Membrane fusion intermediates and the effect of cholesterol: An in-house x-ray scattering study. *European Physical Journal E* **30**, 205 (2009).

[ASKK96]   A.Snigirev, I. Snigireva, V.G. Kohn, and S.M. Kuznetsov. On the requirements to the instrumentation for the new generation of the synchrotron radiation sources. beryllium windows. *Nuclear Instruments & Methods in Physics* **370**, 634 (1996).

[BCG$^+$09] P. Bleuet, P. Cloetens, P. Gergaud, D. Mariolle, N. Chevalier, R. Tucoulou, J. Susini, and A. Chabli. A hard x-ray nanoprobe for scanning and projection nanotomography. *Review of Scientific Instruments* **80**, 056101 (2009).

[BDOB91]   J.J. Benattar, J. Daillant, O.Belorgey, and L. Bosio. Langmuir monolayers and newton black films: Two-dimensional systems investigated by x-ray reflectivity. *Physica A: Statistical and Theoretical Physics* **172**, 225 (1991).

[Bee06]   A. Beerlink. Planare, freistehende Lipidmembranen für die Röntgenstrukturanalyse. Master's thesis, University of Göttingen (2006).

[BEL66]   A.V. Babakov, L.N. Ermishkin, and E.A. Liberman. Influence of electric field in the capacity of phospholipid membranes. *Nature* **210**, 953 (1966).

[BH65]   U. Bonse and M. Hart. An x-ray interferometer. *Applied Physics Letters* **6**, 155 (1965).

[BLH+04]   I. Burgess, M. Li, S.L. Horswell, G Szymanski, J. Lipowski, and J. Majewski S. Satija. Electric field driven transformation of a supported model biological membrane - an electrochemical and neutron reflectivity study. *Biophysical Journal* **86**, 1763 (2004).

[BLH+05]   I. Burgess, M. Li, S.L. Horswell, G. Szymanski, J. Lipkowski, S. Satija, and J. Majewski. Influence of the electric field on a bio-mimetic film supported on a gold electrode. *Colloids and Surfaces B: Biointerfaces* **40**, 117 (2005).

[BLRH75]   D.E. Brooks, Y.K. Levine, J. Requena, and D.A. Haydon. Van der waals forces in oil-water systems from the study of thin lipid films: Iii. comparison of experimental results with hamaker coefficients calculated from lifshitz theory. *Proceedings of the Royal Society of London A* **347**, 179 (1975).

[BMTS09]   A. Beerlink, M. Mell, M. Tolkiehn, and T. Salditt. Hard x-ray phase contrast imaging of black lipid membranes. *Applied Physics Letters* **95**, 203703 (2009).

[BOLM75]   R. Benz, O.Fröhlich, P. Läuger, and M. Montal. Electrical capacity of blck lipid films and of lipid bilayers made from monolayers. *Biochimica et Biophysica Acta* **394**, 323 (1975).

[Boy59]   C.V. Boys. *Soap Bubbles: Their Colours ant the Forces which Mould Them.* Dover Science (1959).

[Bro94]   H. Brockman. Dipole potential of lipid membranes. *Chemistry and Physics of Lipids* **73**, 57 (1994).

[BS06]   A. Beerlink and T. Salditt. Investigation of biological membranes. *Nanopticum* **1**, 6 (2006).

[BW99]   M. Born and E. Wolf. *Principles of Optics.* Cambridge University Press (1999).

[BWZ⁺08] A. Beerlink, P.-J. Wilbrandt, E. Ziegler, D. Carbone, T.H. Metzger, and T. Salditt. X-ray structure analysis of free-standing lipid membranes facilitated by micromachined apertures. *Langmuir* **24**, 4952 (2008).

[CBAFG99] T. Charitat, E. Bellet-Amalric, G. Fragneto, and F. Graner. Adsorbed and free lipid bilayers at the solid-liquid interface. *European Physical Journal E* **8**, 583 (1999).

[CBB⁺96] P. Cloetens, R. Barrett, J. Baruchel, J.-P. Guigay, and M. Schlenker. Phase objects in synchrotron hard x-ray imaging. *Journal of Physics D: Applied Physics* **29**, 133 (1996).

[CC67] R.J. Cherry and D. Chapman. Refractive index determination of lecithin black films. *Journal of Molecular Biology* **30**, 551 (1967).

[CC69a] R.J. Cherry and D. Chapman. Optical determination of the thickness of thin lipid films. *Journal of Theoretical Biology* **24**, 137 (1969).

[CC69b] R.J. Cherry and D. Chapman. Optical properties of black lecithin films. *Journal of Molecular Biology* **40**, 19 (1969).

[CCG66] J.S. Clunie, J.M. Corkill, and J.F. Goodman. Structure of black foam films. *Discussions of the Faraday Society* **42**, 34 (1966).

[Cev90] G. Cevc. Membrane electrostatics. *Biochimica et Biophysica Acta* **1031**, 311 (1990).

[CGOT63] J.M. Corkill, J.F. Goodman, C.P. Ogden, and J.R. Tate. The structure and stability of black foam films. *Proceedings of the Royal Society of London A* **273**, 84 (1963).

[Cla01] R.J. Clarke. The dipole potential of phospholipid membranes and methods for its detection. *Advances in Colloid and Interface Science* **89**, 263 (2001).

[CLF08] T. Charitat, S. Lecuyer, and G. Fragneto. Fluctuations and destabilization of single phospholipid bilayers. *Biointerphases* **3**, FB3 (2008).

[Clo99] P. Cloetens. *Contribution to Phase Contrast Imaging, Reconstruction and Tomography with Hard Synchrotron Radiation*. PhD thesis, Free University of Brussel (1999).

[CMP+00]   N. Cuvillier, F. Millet, V. Petkova, M. Nedyalkov, and J.J. Benattar. Structure of freestanding phospholipidic bilayer films. *Langmuir* **16**, 5029 (2000).

[COVS05]   D. Constantin, C. Ollinger, M. Vogel, and T. Salditt. Electric field unbinding of solid-supported lipid multilayers. *European Physical Journal E* **18**, 273 (2005).

[Cow75]   J.M. Cowley. *Diffraction physics.* Elsevier Science B.V. (1975).

[CPN+00]   N. Cuvillier, V. Petkova, M. Nedyalkov, F. Millet, and J.J. Benattar. Protein insertion within a biological freestanding film. *Physica B: Condensed Matter* **283**, 1 (2000).

[CRC02]   V. Cherezov, K.M. Riedl, and M. Caffrey. Too hot to handle? synchrotron x-ray damage of lipid membranes and mesophases. *Journal of Synchrotron Radiation* **9**, 333 (2002).

[Cro73]   J.M. Crowley. Electrical breakdown of bimolecular lipid membranes as an electromechanical instability. *Biophysical Journal* **13**, 711 (1973).

[CRP+09]   A. Cecilia, A. Rack, D. Pelliccia, P.-A. Douissard, T. Martin, M. Couchaud, K. Dupre, and T. Baumbach. Studies of LSO:Tb radio-luminescence properties using white beam hard x-ray synchrotron irradiation. *Radiation Effects and Defects in Solids* **164**, 517 (2009).

[CS00]   W. Römer C. Steinem. Pore-spanning lipid bilayers visualized by scanning force microscopy. *Journal of American Chemical Society* **122**, 8085 (2000).

[DAB+06]   R. Dimova, S. Aranda, N. Bezlyepkina, V. Nikolov, K.A. Riske, and R. Lipowsky. A practical guide to giant vesicles. probing the membrane nanoregime via optical microscopy. *Journal of Physics: Condensed Matter* **18**, S1151 (2006).

[Dai09]   J. Daillant. Recent developments and applications of grazing incidence scattering. *Current Opinion in Colloid & Interface Science* **14**, 396 (2009).

[DBAB+05]   J. Daillant, E. Bellet-Amalric, A. Braslau, T. Charitat, G. Fragneto, F. Graner, S. Mora, F. Rieutord, and B. Stidder. Structure and fluctuations of a single floating lipid bilayer. *Proceedings of the National Academy of Sciences* **102**, 11639 (2005).

[Dea08]   D.W. Deamer. How leaky were primitive cells? *Nature* **454**, 37 (2008).

[DEKP07]   Rolf Dootz, Heather Evans, Sarah Köster, and Thomas Pfohl. Rapid prototyping of x-ray microdiffraction compatible continuous microflow foils. *Small* **3**, 96 (2007).

[DFH82]   J.P. Dilger, L.R. Fisher, and D.A. Haydon. A critical comparison of electrical and optical methods for bilayer thickness detemination. *Chemistry and Physics of Lipids* **30**, 159 (1982).

[dFJS$^+$98]   D. di Fonzo, W. Jark, G. Soullie, A. Cedola, S. Lagomarsino, P. Cloetens, and C. Riekel. Submicrometre resolution phase-contrast radiography with the beam from an x-ray waveguide. *Journal of Synchrotron Radiation* **5**, 376 (1998).

[DG09]   J. Daillant and A. Gibaud, editors. *X-ray and Neutron Reflectivity*. Springer (2009).

[DGG$^+$95a]   T.J. Davis, D. Gao, T.E. Gureyev, A.W. Stevenson, and S.W. Wilkins. Phase contrast imaging of weakly absorbing materials using hard x-rays. *Nature* **373**, 595 (1995).

[DGG$^+$95b]   T.J. Davis, T.E. Gureyev, D. Gao, A.W. Stevenson, and S.W. Wilkins. X-ray image contrast from a simple phase object. *Physical Review Letters* **74**, 3173 (1995).

[DH35]   J.F. Danielli and H.Davson. A contribution to the theory of permeability of thin filmss. *J. Cell. Comp. Phys.* **5**, 495 (1935).

[DL41]   B. Derjaguin and L. Landau. Theory of the stability of strongly charged lyophobic sols and of the adhesion of strongly charged particles in solutions of electrolytes. *Acta Physico Chemica URSS* **14**, 633 (1941).

[DPR64]   J.F. Danielli, K.G.A. Pankhurst, and A.C. Riddiford, editors. *Recent Progress in Surface Science*, volume 1. Academic Press, New York (1964).

[DRI$^+$07]   S.M. Danauskas, M.K. Ratajczak, Y. Ishitsuka, J. Gebhardt, D. Schultz, M. Meron, B. Lin, and K.Y.C. Lee. Monitoring x-ray beam damage on lipid films by an integrated brewster angle microscope/x-ray diffractometer. *Review of Scientific Instruments* **78**, 103705 (2007).

[ET03]   T. Ederth and R.K. Thomas. A neutron reflectivity study of drainage and stratification of aot foam films. *Langmuir* **19**, 7727 (2003).

[FFI03]   H. Fujiwara, M. Fujihara, and T. Ishiwata. Dynamics of the spontaneous formation of a planar phospholipid bilayer: A new approach by simultaneous electrical and optical measurements. *Journal of chemical physics* **119**, 6768 (2003).

[FH86]   R.F. Flewelling and W. Hubbell. The membrane dipole potential in a total membrane model. *Biophysical Journal* **4**, 541 (1986).

[Fit00]   R. Fitzgerald. Phase-sensitive x-ray imaging. *Physics Today* **53**, 23 (2000).

[FST06]   K. Funakoshi, H. Suzuki, and S. Takeuchi. Lipid bilayer formation by contacting monolayers in a microfluidic device for membrane protein analysis. *Analytical Chemistry* **78**, 8169 (2006).

[Fuh06]   C. Fuhse. *X-ray waveguides and waveguide-based lensless imaging.* PhD thesis, University of Göttingen (2006).

[Gab48]   D. Gabor. A new microscopy principle. *Nature* **161**, 777 (1948).

[GBK⁺10]   R. S. Gracià, N. Bezlyepkina, R. L. Knorr, R. Lipowsky, and R. Dimova. Effect of cholesterol on the rigidity of saturated and unsaturated membranes: fluctuation and electrodeformation analysis of giant vesicles. *Soft Matter* **6**, 1472 (2010).

[GG25]   E. Gorter and F. Grendel. On bimolecular layers of lipoids on the chromocytes of the blood. *The Journal of Experimental Medicine* **41**, 439 (1925).

[Gib48]   J.W. Gibbs. *On the Equilibrium of Heterogeneous Substances.* Yale University Press, New Haven (1948).

[Gib61]   J.W. Gibbs. *The scientific papers.* Dover Publications, New York (1961).

[GKK⁺10]   K. Giewekemeyer, S.P. Krüger, S. Kalbfleisch, M. Bartels, C. Beta, and T. Salditt. Lensless biological x-ray microscopy using waveguides. *Physical Review Letters* **-**, submitted (2010).

[GLSW99]   T. Gutsmann, J.W. Larrick, U. Seydel, and A. Wiese. Molecular mechanisms of interaction of rabbit cap18 with outer membranes of gram-negative bacteria. *Biochemistry* **38**, 13643 (1999).

[GNK+10]   K. Giewekemeyer, H. Neubauer, S. Kalbfleisch, S. P. Krüger, and T. Salditt. Holographic and diffractive x-ray imaging using waveguides as quasi-point sources. *New Journal of Physics* **12**, 035008 (2010).

[GRZ+92]   K. Gawrisch, D. Ruston, J. Zimmerberg, V.A. Parsegian, R.P. Rand, and N. Fuller. Membrane dipole potentials, hydration forces and the ordering of water at membrane surfaces. *Biophysical Journal* **61**, 1213 (1992).

[GS07]   K. Giewekemeyer and T. Salditt. Counterion distribution near a monolayer of variable charge density. *Europhysics Letters* **79**, 18003 (2007).

[Gui77]   J. P. Guigay. Fourier transform analysis of fresnel diffraction patterns and in-line holograms. *Optik* **46**, 121 (1977).

[Gup72]   M.L. Gupta. Comments on the dipole model and phase transitions in biological membranes. *Biophysical Journal* **12**, 1367 (1972).

[Hag03]   S.O. Hagge. *Charakterisierung der Eigenschaften rekonstituierter planarer Membranen und deren Änderung durch porenbildende Proteine mit Hilfe von elektrischen und optischen Methoden.* PhD thesis, University of Kiel (2003).

[Haw06]   M.H. Hawton. An analytic treatment of the condensation of phospholipid chains. *Journal of Biological Physics Today* **5**, 141 (2006).

[HBRS98]   R. Hirn, T.M. Bayerl, J.O. Rädler, and E. Sackmann. Collective membrane motions of high and low amplitude, studied by dynamic light scattering and micro-interferometry. *Faraday Discussion* **111**, 17 (1998).

[HCRM05]   O. Hignette, P. Cloetens, G. Roasting, and C. Morawe. Efficient sub 100nm focussing of hard x-rays. *Review of Scientific Instruments* **76**, 063709 (2005).

[HDGT67]   F.A. Henn, G.L. Decker, J.W. Greenawalt, and T.E. Thompson. Properties of lipid bilayer membranes separating two aqueous

phases: electron microscope studies. *Journal of Molecular Biology* **24**, 51 (1967).

[Hei07]   T. Heimburg. *Thermal Biophysics of Membranes.* Wiley-VCH (2007).

[HHT64]   T. Hanai, D. A. Haydon, and Janet Taylor. An investigation by electrical methods of lecithin-in-hydrocarbon films in aqueous solutions. *Proceedings of the Royal Society of London A* **281**, 377 (1964).

[HHT65]   T. Hanai, D. A. Haydon, and J.L. Taylor. Polar group orientation and the electrical properties of lecithin bimolecular leaflets. *Journal of Theoretical Biology* **9**, 278 (1965).

[HHT⁺84]   R.R. Highfield, R.P. Humes, R.K. Thomas, P.G. Cummins, D.P. Gregory, J. Mingins, J.B. Hayter, and O. Schaerpf. Critical reflection of neutron from a soap film. *Journal of Colloid and Interface Science* **97**, 367 (1984).

[Hil84]   B. Hille. *Ionic Channels of Excitable Membranes.* Sinauer, Massachusetts (1984).

[Hil04]   M. Hildenbrand. *Modulation kollektiver Membrandynamik im mesoskopischen Bereich durch Einbau und Adsorption von Biomolekülen.* PhD thesis, University Würzburg (2004).

[HL82]   W. Hoppe and W. Lohmann. *Biophysik.* Springer Verlag, 2. edition (1982).

[HNB07]   M.A. Holden, D. Needham, and H. Bayley. Functional bionetworks from nanoliter water droplets. *Journal of American Chemical Society* **129**, 8650 (2007).

[Hoo57]   R. Hooke. *The History of the Royal Society of London.* A. Millar, London (1757).

[HRC⁺01]   O. Hignette, G. Roasting, P. Cloetens, A. Rommeveaux, and A. Freund. Submicron focussing of hard x-rays with reflecting surfaces at the ESRF. *Proceedings of SPIE* **4499**, 105 (2001).

[HT65]   C. Huang and T.E. Thompson. Properties of lipid bilayer membranes separating two aqueous phases: Determination of membrane thickness. *Journal of Molecular Biology* **13**, 183 (1965).

[HT68]   D. A. Haydon and J.L. Taylor. Contact angle for thin lipid films and the determination of london-van der waals forces. *Nature* **217**, 739 (1968).

[HW80]   D.B. Hough and L.R. White. The calculation of hamaker constants from lifshitz theory with application to wetting phenomena. *Advances in Colloid and Interface Science* **14**, 3 (1980).

[HWSG04]   S.O. Hagge, A. Wiese, U. Seydel, and T. Gutsmann. Inner field compensation as a tool for the characterization of asymmetric membranes and peptide-membrane interactions. *Biophysical Journal* **86**, 913 (2004).

[HWT64]   C. Huang, L. Wheeldon, and T.E. Thompson. The properties of lipid bilayer membranes separating two aqueous phases: Formation of a membrane of simple composition. *Journal of Molecular Biology* **8**, 148 (1964).

[IB95]   V.N. Ingal and E.A. Beliaevskaya. X-ray plane-wave topography observation of the phase-contrast from a noncrystalline object. *Journal of Physics D* **28**, 2314 (1995).

[Int09]   Internetsource. *Cm-Measurements with PATCHMASTER EPC10 (Tutorial)*. http://www.heka.com/support/tuto.html (2009).

[Int10]   Internetsource. *Colors of a soap film*. http://www.bmo.physik.-uni-muenchen.de/lehre/WS08/E3/vorlesung-E3.html (2010).

[Ise92]   C. Isenberg. *The Science of Soap Films and Soap Bubbles*. Dover Publications Inc. (1992).

[Isr92]   J.N. Israelachvili. *Intermolecular and Surface Forces: With Applications to Colloidal and Biological Systems*. Academic Press (1992).

[Iva88]   I.B. Ivanov, editor. *Thin Liquid Films: Fundamentals and Applications*. Dekker New York (1988).

[Joh05]   B.R.G. Johnson. *Biomimetic Scaffolds for Phospholipid Bilayers*. PhD thesis, University of Leeds (2005).

[KGK$^+$10] S.P. Krüger, K. Giewekemeyer, S. Kalbfleisch, M. Bartels, H. Neubauer, and T. Salditt. Sub-15 nm beam confinement by two crossed x-ray waveguides. *Optics Express* **-**, accepted (2010).

[KLK+01]   M.A. Kiselev, P. Lesieur, A.M. Kisselev, D. Lombardo, M. Killany, S. Lesieur, and M. Ollivon. A sucrose solutions application to the study of model biological membranes. *Nuclear Instruments and Methods in Physics Research A* **470**, 409 (2001).

[KP10]   S. Köster and T. Pfohl. Fabrication of microfluidic devices. personal communication, (2010).

[KRSS98]   A. Koch, C. Raven, P. Spanne, and A. Snigirev. X-ray imaging with submicrometer resolution employing transparent luminescent screens. *Journal of the Optical Society of America A* **15**, 1940 (1998).

[LCC+97]   S. Lagomarsino, A. Cedola, P. Cloetens, S. di Fonzo, W. Jark, G. Soullié, and C. Riekel. Phase contrast hard x-ray microscopy with submicron resolution. *Applied Physics Letters* **71**, 2557 (1997).

[LCM+07]   J.-C. Labiche, D.F. Carreiras, O. Mathon, S. Pascarelli, M.A. Newton, G.G. Ferre, C. Curfs, G. Vaughan, and A. Homs. The fast read-out low noise camera as a versatile x-ray detector for time resolved dispersive extended x-ray absorption fine structure and diffraction studies of dynamic problems in materials science, chemistry and catalysis. *Review of Scientific Instruments* **78**, 091301 (2007).

[LFC06]   S. Lecuyer, G. Fragneto, and T. Charitat. Effect of an electric field on a floating lipid bilayer: A neutron reflectivity study. *European Physical Journal E* **21**, 153 (2006).

[LK03]   W. Lauterborn and T. Kurz. *Coherent optics*. Springer (2003).

[Lon30]   F. London. Zur theorie und systematik der molekularkräfte. *Zeitschrift für Physik* **63**, 245 (1930).

[LPGP08]   M. Langer, P.Cloetens, J.-P. Guigay, and F. Peyrin. Quantitative comparison of direct phase retrieval algorithms in in-line phase tomography. *Med. Phys.* **35**, 4556 (2008).

[LRWW99]   J.C. Lagarias, J.A. Reeds, M.H. Wright, and P.E. Wright. Convergence properties of the nelder-mead simplex method in low dimensions. *SIAM Journal on Optimization* **2009**, 112 (1999).

[LSR+99]   B. Lengeler, C.G. Schroer, M. Richwin, J. Tümmler, M. Drakopoulos, A. Snigirev, and I. Snigireva. A microscope for hard x rays

based on parabolic compound refractive lenses. *Applied Physics Letters* **74**, 3924 (1999).

[LT69]   E.A. Liberman and V.P. Topaly. Permeability of bimolecular phospholipid membranes for fat-soluble ions. *Biophysics* **14**, 477 (1969).

[MCD10]   L. Malaquin, T. Charitat, and J. Daillant. Supported bilayers: Combined specular and diffuse x-ray scattering. *European Physical Journal E* **31**, 285 (2010).

[McL89]   S. McLaughin. The electrostatic properties of membranes. *Annual Review of Biophysics and Biophysical Chemistry* **18**, 113 (1989).

[MCM⁺07]   R. Mokso, P. Cloetens, E. Maire, W. Ludwig, and J.Y. Buffiere. Nanoscale zoom tomography with hard x rays using kirkpatrick-baez optics. *Applied Physics Letters* **90**, 144104 (2007).

[MDC⁺09]   T. Martin, P.-A. Douissard, M. Couchaud, A. Cecilia, T. Baumbach, K. Dupre, and A. Rack. Lso-based single crystal film scintillator for synchrotron-based hard x-ray micro-imaging. *IEEE Transactions on Nuclear Science* **56**, 1412 (2009).

[MDG⁺03]   S. Mayo, T. Davis, T. Gureyev, P. Miller, D. Paganin, A. Pogany, A. Stevenson, and S. Wilkins. X-ray phase-contrast microscopy and microtomography. *Optics Express* **11**, 2289 (2003).

[Med94]   R. Medenwaldt. *Development of X-Ray Microscopy in Aarhus and Ultra Thin Foil Production to Speed Up High Resolution X-Ray Optics.* PhD thesis, Universität Aarhus (1994).

[Mel09]   M. Mell. Phase contrast imaging of lipid bilayer model membranes using hard x-rays. Master's thesis, University of Göttingen (2009).

[MF95]   A. Momose and J. Fukuda. Phase-contrast radiographs of non-stained rat cerebellar specimen. *Medical Physics* **22**, 375 (1995).

[MJ66]   K.J. Mysels and M.N. Jones. Direct measurement of the variation of double-layer repulsion with distance. *Discussions of the Faraday Society* **42**, 42 (1966).

[MK88]   P.-M. Möglich and G. Kretzschmar. Optical determination of the thickness of single planar thin lipid films using the symmetrical three-layer model. *Colloid and Polymer Science* **266**, 739 (1988).

[MK06]   T. Martin and A. Koch. Recent developments in x-ray imaging with micrometer spatial resolution. *Journal of Synchrotron Radiation* **15**, 180 (2006).

[MM72]   M. Montal and P. Mueller. Formation of biomolecular membranes from lipid monolayers and a study of their electrical properties. *Proceedings of the National Academy of Sciences* **69**, 3561 (1972).

[MMGK05]   C. E. Miller, J. Majewski, T. Gog, and T. L. Kuhl. Characterization of biological thin films at the solid-liquid interface by x-ray reflectivity. *Physical Review Letters* **94**, 2381041 (2005).

[MMW$^+$02] S.C. Mayo, P.R. Miller, A.W. Wilkins, T.J. Davis, D. Gao, T.E. Gureyev, D. Paganin, D.J. Parry, A. Pogany, and A.W. Stevenson. Quantitative x-ray projection microscopy: phase-contrast and multispectral imaging. *Journal of Microscopy* **207**, 79 (2002).

[MN05]   E.D. Manev and A.V. Nguyen. Critical thickness of microscopic thin liquid film. *Advances in Colloid and Interface Science* **114-115**, 133 (2005).

[Mom03]   A. Momose. Phase-sensitive imaging and phase tomography using x-ray interferometers. *Optics Express* **11**, 2303 (2003).

[Mon74]   M. Montal. Formation of bimolecular membranes from lipid monolayers. *Methods in Enzymology* **32**, 545 (1974).

[MRTW62a] P. Müller, D.O. Rudin, H.T. Tien, and W.C. Wescott. Reconstitution of excitable cell membrane structure in vitro. *Circulation* **26**, 1167 (1962).

[MRTW62b] P. Müller, D.O. Rudin, H.T. Tien, and W.C. Wescott. Reconstitution of excitable cell membrane structure in vitro and its transformation into an excitable system. *Nature* **194**, 979 (1962).

[MSF59]   K.J. Mysels, K. Shinoda, and S. Frankel. *Soap films. Study of their Thinning and a Bibliography*. Pergamon Press, New York (1959).

[MSK$^+$08] S.S. Mansy, J.P. Schrum, M. Krishnamurthy, S. Tobe, D.A. Treco, and J.W. Szostak. Template-directed synthesis of a genetic polymer in a model protocell. *Nature* **454**, 122 (2008).

[MSS⁺09]   I. Mey, M. Stephan, E.K. Schmitt, M.M. Müller, M.B. Amar, C. Steinem, and A. Janshoff. Local membrane mechanics of pore-spanning bilayers. *Journal of American Chemical Society* **131**, 7031 (2009).

[MT06]   K. Morigaki and K. Tawa. Vesicle fusion studied by surface plasmon resonance and surface plasmon fluorescence spectroscopy. *Biophysical Journal* **91**, 1380 (2006).

[Mys64]   K.J. Mysels. Soap films and some problems in surface and colloid chemistry. *The journal of physical chemistry* **68**, 3441 (1964).

[Mys68]   K.J. Mysels. Dynamic processes in soap films. *The Journal of General Physiology* **52**, 113 (1968).

[New74]   I. Newton. *Theory of light and colours (in soap bubbles).* n.A. (1674).

[NGC⁺96]   K.A. Nugent, T.E. Grureyev, D.F. Cookson, D. Paganin, and Z. Barnea. Quantitative phase imaging using hard x-rays. *Physical Review Letters* **77**, 2961 (1996).

[NGS06]   E. Novakova, K. Giewekemeyer, and T. Salditt. Structure of two-component lipid membranes on solid support: An x-ray reflectivity study. *Physical Review E* **74**, 051911 (2006).

[NL69]   B. Neumcke and P. Läuger. Nonlinear electrical effects in lipid bilayer membranes: II. intergration of the generalized nernst-planck equations. *Biophysical Journal* **9**, 1160 (1969).

[Nov08]   E. Nováková. *Structure of charged two-component lipid membranes and their interaction with colloids studied by different X-ray and microscopy techniques.* PhD thesis, University of Göttingen (2008).

[NP70]   B.W. Ninham and V.A. Parsegian. Van der waals forces: Special characteristics in lipid-water systems and a general methos of calculation baeds on the lifshitz theory. *Biophysical Journal* **10**, 646 (1970).

[NS76]   E. Neher and B. Sackmann. Single-channel currents recorded from membrane of denervated frog muscle fibres. *Nature* **260**, 799 (1976).

[Nug10]   K.A. Nugent. Coherent methods in the x-ray sciences. *Advances in Physics* **59**, 1 (2010).

[Ohk69]   S. Ohki. The electrical capacitance of phospholipid membranes. *Biophysical Journal* **9**, 1195 (1969).

[Ohk80]   S. Ohki. Membrane potential and ion permeability of lipid bilayer membranes. *Bioelectrochemistry and Bioenergetics* **7**, 487 (1980).

[OKS⁺05]   A. Otten, S. Köster, B. Struth, A. Snigirev, and T. Pfohl. Microfluidics of soft matter investigated by small angle x-ray scattering. *Journal of Synchrotron Radiation* **12**, 745 (2005).

[Oli05]   V. Oliynyk. *Experimental study of membranes: lipid domain forming and peptide aggregation.* PhD thesis, Universität Göttingen (2005).

[OTST08]   S. Ota, W.-H. Tan, H. Suzuki, and S. Takeuchi. Microfluidic formation of lipid bilayers array for membrane transport analysis. *MEMS* **1**, 18 (2008).

[OTVH08]   M. Otendal, T. Tuohimaa, U. Vogt, and H.M. Hertz. A 9 kev electron-impact liquid-gallium-jet x-ray source. *Review of Scientific Instruments* **79**, 016102 (2008).

[Ove60]   J.T.G. Overbeek. Black soap films. *Journal of Physical Chemistry* **64**, 1178 (1960).

[Pag06]   D.M. Paganin. *Coherent X-Ray Optics.* Oxford University Press (2006).

[Pan99]   M. Panitz. Gold-Zonenplatten als Röntgenobjektive für Photonenenergien um 4 kev. Master's thesis, Universität Göttingen (1999).

[Par54]   L.G. Parratt. Surface studies of solids by total reflection of x-rays. *Physical Review* **95**, 359 (1954).

[PBN02]   V. Petkova, J.J. Benattar, and M. Nedyalkov. How to control the molecular architecture of a monolayer of proteins supported by a lipid bilayer. *Biophysical Journal* **82**, 541 (2002).

[PDB⁺08]   F. Pfeiffer, C. David, O. Bunk, T. Donath, M. Bech, G. Le Duc, A. Bravin, and P. Cloetens. Region-of-interest tomography for grating-based x-ray differential phase-contrast imaging. *Physical Review Letters* **101**, 16810 (2008).

[Pfe90]   W. Pfeffer. Zur Kenntniss der Plasmahaut und der Vacuolen. *Abhandlungen der sächsischen Akademie der Wissenschaften* **16**, 187 (1890).

[PGW90]   D. Platikanov, H.A. Graf, and A. Weiss. X-ray scattering by black foam films. *Colloid & Polymer Science* **268**, 760 (1990).

[PGWC93]   D. Platikanov, H.A. Graf, A. Weiss, and D. Clemens. X-ray scattering by black foam films: New data analysis. *Colloid & Polymer Science* **271**, 106 (1993).

[Pla73]   J. A. F. Plateau. *Statique experimentale et theorique des liquides soumis aux seules forces moleculaires.* Gauthiers-Villars, Paris (1873).

[PML⁺02]   U. Peterson, D.A. Mannock, R.N.A.H. Lewis, P. Pohl, R.N. McElhaney, and E.E. Pohl. Origin of membrane dipole potential: Contribution of the phospholipid fatty acid chains. *Chemistry and Physics of Lipids* **117**, 19 (2002).

[Pre88]   David M. Prescott. *Cells.* Jones and Bartlett (1988).

[PWBD06]   F. Pfeiffer, T. Weitkamp, O. Bunk, and C. David. Phase retrieval and differential phase contrast imaging with low brilliance x-ray sources. *Nature Physics* **2**, 258 (2006).

[QCR⁺07]   A. Quist, A. Chand, S. Ramachandran, C. Daraio, S. Jin, and R. Lal. Atomic force microscopy imaging and electrical recording of lipid bilayers supported over microfabricated silicon chip nanopores: Lab-on-a-chip system for lipid membranes and ion channels. *Langmuir* **23**, 1375 (2007).

[RBH75]   J. Requena, D.F. Billett, and D.A. Haydon. Van der waals forces in oil-water system from the study of thin lipid films: I. measurement of the contact angle and the estimation of the van der waals free energy of thinning of a film. *Proceedings of the Royal Society of London A* **347**, 141 (1975).

[RBH77]   J. Requena, D.E. Brooks, and D.A. Haydon. Van der waals forces in oil-water systems. *Journal of Colloid and Interface Science* **58**, 26 (1977).

[RCMD09]   A. Rack, M. Couchaud, T. Martin, and K. Dupre. *Patent: Szintillatorelement sowie Festkörperstrahlungsdetektor mit solchem.* DE102007054700 (A1) (2009).

[Req75]   J. Requena. Lenses and compression of black lipid membranes by an electric field. *Biophysical Journal* **15**, 77 (1975).

[Röm04]   W. Römer. *Impedance analysis and single ion channel recordings on pore-suspending lipid bilayers based on highly ordered pore arrays*. PhD thesis, Universität Regensburg (2004).

[RMB03]   R. Richter, A. Mukhopadhyay, and A. Brisson. Pathways of lipid vesicle deposition on solid surfaces: A combined qcm-d and afm study. *Biophysical Journal* **85**, 3035 (2003).

[RSS+96]   C. Raven, A. Snigirev, I. Snigireva, P. Spanne, A. Souvorov, and V. Kohn. Phase-contrast microtomography with coherent high-energy synchrotron x rays. *Applied Physics Letters* **69**, 1826 (1996).

[Sac95]   E. Sackmann. *Handbook of Biological Physics, Volume 1*. Elsevier Science B.V. (1995).

[Sac96]   E. Sackmann. Supported membranes: Scientific and practical applications. *Science* **271**, 43 (1996).

[Sal03]   T. Salditt. Lipid-peptide interaction in oriented bilayers probed by interface-sensitive scattering methods. *Current Opinion in Structural Biology* **13**, 467 (2003).

[SBW+09]   P.E. Schneggenburger, A. Beerlink, B. Worbs, T. Salditt, and U. Diederichsen. A novel heavy-atom label for side-specific peptide iodination: Synthesis, membrane incorporation and x-ray reflectivity. *ChemPhysChem* **10**, 1567 (2009).

[SC71]   R. Simons and P.E. Ciddor. Optical properties of membrane models at arbitrary angles of incidence. *Biochimica et Biophysica Acta* **233**, 296 (1971).

[Sch08]   A. Schropp. *Experimental Coherent X-Ray Diffractive Imaging: Capabilities and Limitations of the Technique*. PhD thesis, University of Hamburg (2008).

[SGF+09]   T. Salditt, K. Giewekemeyer, C. Fuhse, S.P. Krüger, R. Tucoulou, and P. Cloetens. Projection phase contrast microscopy with a hard x-ray nanofocused beam: Defocus and contrast transfer. *Physical Review B* **79**, 184112 (2009).

[SI02]   P. Sens and H. Isambert.   Undulation instability of lipid mem-branes under an electric field. *Physical Review Letters* **88**, 128102 (2002).

[Sim70]   R. Simons.   The thickness of bimolecular lipid membranes. *Biochimica et Biophysica Acta* **203**, 209 (1970).

[SK80]   V.S. Sokolov and V.C. Kuz'min. Study of surface potential differ-ence in bilayer membranes according to the second harmonic re-sponse of capacitance current. *Biofizika* **25**, 170 (1980).

[SKFB08]   T. Salditt, S. P. Krüger, C. Fuhse, and C. Bahtz. High-transmission planar x-ray waveguides. *Physical Review Letters* **100**, 184801 (2008).

[SKSL96]   A. Snigirev, V. Kohn, I. Snigirev, and B. Lengeler. A compound refractive lens for focusing high-energy x-rays. *Nature* **384**, 49 (1996).

[SLSM02]   T. Salditt, C. Li, A. Spaar, and U. Mennicke. X-ray reflectivity of solid-supported multilamellar membranes. *European Physical Journal E* **7**, 105 (2002).

[SMB+04]   C. Sultanem, S. Moutard, J.J. Benattar, F. Djedaïni-Pilard, and B. Perly. Hydration of black foam films made of amphiphilic cy-clodextrins. *Langmuir* **20**, 3311 (2004).

[SMK+02]   C. G. Schroer, J. Meyer, M. Kuhlmann, B. Benner, T. F. Günzler, B. Lengeler, C. Rau, T. Weitkamp, A. Snigirev, and I. Snigireva. Nanotomography based on hard x-ray microscopy with refractive lenses. *Applied Physics Letters* **81**, 1527 (2002).

[SN72]   S.J. Singer and G.L. Nicolson. The fluid mosaic model of the struc-ture of cell membranes. *Science* **175**, 720 (1972).

[SRS+86]   C.R. Safinya, D. Roux, G.S. Smith, S.K. Sinha, P. Dimon, N.A. Clark, and A.M. Bellocq. Steric interactions in a model multimembrane system: A synchrotron study. *Physical Review Letters* **57**, 2718 (1986).

[SS59]   C.V Sternling and L.E. Scriven. Interfacial turbulence: Hydrody-namic instability and the marangoni effect. *A.I.Ch.E. Journal* **5**, 514 (1959).

[SS60]   L.E. Scriven and C.V. Sternling. The marangoni effects. *Nature* **187**, 186 (1960).

[SS90]   M. Seul and M.J. Sammon. Preparation of surfactant multilayer films on solid substrates by deposition from organic solution. *Thin solid films* **185**, 287 (1990).

[SSK+95]   A. Snigirev, I. Snigireva, V. Kohn, S. Kuznetsov, and I. Schelokov. On the possibilities of x-ray phase contrast microimaging by coherent high-energy synchrotron radiation. *Review of Scientific Instruments* **66**, 5486 (1995).

[SSS79]   P. Schoch, D.F. Sargent, and R. Schwyzer. Capacitance and conductance as tools for the measurement of asymmetric surface potentials and energy barriers of lipid bilayer membranes. *Journal of Membrane Biology* **46**, 71 (1979).

[SSS+90]   G.S. Smith, E.B. Sirota, C.R. Safinya, R.J. Plano, and N.A. Clark. X-ray structural studies of freely suspended ordered hydrated dmpc multimembrane films. *Journal of Chemical Physics* **92**, 4519 (1990).

[SSSC88]   G.S. Smith, E.B. Sirota, C.R. Safinya, and N.A. Clark. Structure of the lb phases in a hydrated phosphatidylcholine multimembrane. *Physical Review Letters* **60**, 813 (1988).

[Str03]   L. Stryer. *Biochemie.* Spektrum, 5. edition (2003).

[Stu81]   G. Stulen. Electric field effects on lipid membrane structure. *Biochimica et Biophysica Acta* **640**, 621 (1981).

[TBGO98]   H.T. Tien, R.H. Barish, L.-Q. Gu, and A.L. Ottova. Supported bilayer membranes as ion and molecular probes. *Analytical Science* **14**, 3 (1998).

[TBL+02]   J.F. Tranchant, F. Bonté, S. Leroy, M. Nedyalkov, D. Platikanov, I. Javierre, and J.J. Benattar. Black foam films from aqueous solutions of a mixture of phospholipids and a permeation enhancer. *Journal of Colloid and Interface Science* **249**, 398 (2002).

[TCD66]   H. T. Tien, S. Carbone, and E.A. Dawidowicz. Formation of black lipid membranes by oxidation products of cholesterol. *Nature* **212**, 718 (1966).

[TD66]   H.T. Tien and E.A. Dawidowicz. Black lipid films an aqueous media: A new type of interfacial phenomenon. *Journal of colloid and interface science* **22**, 438 (1966).

[Tei07]   J. Teissie. Biophysical evects of electric welds on membrane water interfaces: a mini review. *European Biophysical Journal* **36**, 967 (2007).

[TH66a]   J. Taylor and D. A. Haydon. Stabilization of thin films of liquid hydrocarbon by alkyl chain interaction. *Discussions of the Faraday Society* **42**, 51 (1966).

[TH66b]   T.E. Thompson and C.H. Huang. Thickness of bilayer membranes. *Journal of Molecular Biology* **16**, 576 (1966).

[Tie66]   H.T. Tien. Thickness and molecular organization of bimolecular lipid membranes in aqueous media. *Journal of Molecular Biology* **16**, 577 (1966).

[Tie67a]   H.T. Tien. Black lipid membranes in aqueous media: interfacial free energy measurements and effect of surfactants on film formation and stability. *Journal of Physical Chemistry* **71**, 3395 (1967).

[Tie67b]   H.T. Tien. Black lipid membranes: Thickness determination and molecular organization by optical methods. *Journal of Theoretical Biology* **16**, 97 (1967).

[Tie68a]   H.T. Tien. Black lipid membranes at bifaces: Formation characteristics, optical and some thermodynamic properties. *The Journal of General Physiology* **52**, 125 (1968).

[Tie68b]   H.T. Tien. The thermodynamics of bimolecular (black) lipid membranes at the water-oil-water biface. *Journal of Physical Chemistry* **72**, 2723 (1968).

[Tie74]   H.T. Tien. *Bilayer Lipid Membranes: Theory and Practice*. Dekker New York (1974).

[TM85]   L.K. Tamm and H.M. McConnell. Supported phospholipid bilayers. *Biophysical Journal* **47**, 105 (1985).

[TO03]   H.T. Tien and A. Ottova. The bilayer lipid membrane (blm) under electric fields. *IEEE Transactions on Dielectrics and Electrical Insulation* **10**, 717 (2003).

[TOH07] T. Tuohimaa, M. Otendal, and H.M. Hertz. Phase-contrast x-ray imaging with a liquid-metal-jet-anode microfocus source. *Applied Physics Letters* **91**, 074104 (2007).

[TOL00] H.T. Tien and A. Ottova-Leitmannova. *Membrane Biophysics*. Elsevier Science B.V. (2000).

[TOL03] H.T. Tien and A. Ottova-Leitmannova. *Planar lipid bilayers (BLMs) and their applications*. Elsevier Science B.V. (2003).

[vdB65] H.J. van den Berg. A new technique for obtaining thin lipid films separating two aqueous media. *Journal of Molecular Biology* **12**, 290 (1965).

[VE71] P.H.J.Th. Ververgaert and P.F. Elbers. Ultrastructural analysis of black lipid membranes. *Journal of Molecular Biology* **58**, 431 (1971).

[VGIB95] O.D. Velev, T.D. Gurkov, I.B. Ivanov, and R.P. Borwankar. Abnormal thickness and stability of nonequilibrium liquid films. *Physical Review Letters* **75**, 264 (1995).

[VM82] V. Vodyanoy and R.B. Murphy. Solvent-free lipid bimolecular membranes of large surface area. *Biochimica et Biophysica Acta* **687**, 189 (1982).

[VMFS00] M. Vogel, C. Münster, W. Fenzl, and T. Salditt. Thermal unbinding of highly oriented phospholipid membranes. *Physical Review Letters* **84**, 390 (2000).

[VO48] E.J.W. Verwey and J.T.G. Overbeek. *Theory of the stability of lyophobic colloids*. Elsevier, Amsterdam (1948).

[Vri64] A. Vrij. Light scattering by soap films. *Journal of Colloid Science* **19**, 1 (1964).

[VST+66] A. Vrij, H. Sonntag, B. Teak, J. A. Kitchener, E. Matijevi, K. J. Mysels, J. T. G. Overbeek, J. M. Corkill, J. F. Goodman, F. M. Fowkes, J. Lyklema, P. F. Mijnlieff, D. Rosen, D. A. Haydon, J. Taylor, and D. H. Napper. General discussion. *Discussions of the Faraday Society* **42**, 60 (1966).

[WAP+06] S.J. Wilk, S. Aboud, L. Petrossian, M. Goryll, J.M. Tang, R.S. Eisenberg, M. Saraniti, S.M. Goodnick, and T.J. Thornton. Ion channel

conductance measurements on a silicon-based platform. *Journal of Physics: Conference Series* **38**, 21 (2006).

[WaSSY76] S.H. White, D.C. Petersen ans S. Simon, and M. Yafuso. Formation of planar bilayer membranes from lipid monolayers: A critique. *Biophysical Journal* **16**, 481 (1976).

[WBK$^+$84] T.H. Watts, A.A. Brian, J.W. Kappler, P. Marrack, and H.M. Mc-Connell. Antigen presentation by supported planar membranes containing affinity-purified i-a. *Proceedings of the National Academy of Sciences* **81**, 7564 (1984).

[WC81] S.H. White and W. Chang. Voltage dependence of the capacitance and area of black lipid membranes. *Biophysical Journal* **36**, 449 (1981).

[WE04a] S.J. Wilk and R.S. Eisenberg. Teflon-coated silicon apertures for supported lipid bilayer membranes. *Applied Physics Letters* **85**, 3307 (2004).

[WE04b] J. Wohlert and O. Edholm. The range and shielding of dipole-dipole interactions in phospholipid bilayers. *Biophysical Journal* **87**, 2433 (2004).

[Wei02] T. Weitkamp. *Imaging and Tomography with High Resolution using Coherent Hard Synchrotron Radiation*. PhD thesis, University of Hamburg (2002).

[WGG$^+$96] S.W. Wilkins, T.E. Gureyev, D. Gao, A. Pogany, and A.W. Stevenson. Phase contrast imaging using polychromatic hard x-rays. *Nature* **384**, 335 (1996).

[WH99] D. Weaire and S. Hutzler. *The physics of foams*. Oxford University Press (1999).

[Whi70] S.H. White. A study of lipid bilayer membrane stability using precise measurements of specific capacitance. *Biophysical Journal* **10**, 1127 (1970).

[Whi72] S.H. White. Analysis of the torus surrounding planar lipid bilayer membranes. *Biophysical Journal* **12**, 432 (1972).

[Whi78] S.H. White. Formation of solvent free black lipid bilayer membranes from glyceryl monooleate dispersed in sqalene. *Biophysical Journal* **23**, 337 (1978).

[Whi80]   S.H. White. How electric fields modify alkane solubility in lipid bilayers. *Science* **207**, 1075 (1980).

[Whi86]   S.H. White. *Ion channel reconstitution: The physical nature of planar bilayer membranes.* Plenum Press, New York (1986).

[WHLH95]   Y. Wu, K. He, S.J. Ludtke, and H.W. Huang. X-ray diffraction study of lipid bilayer membranes interacting with amphiphilic helical peptides: diphytanoyl phosphatidylcholine with alamethicin at low concentrations. *Biophysical Journal* **68**, 2361 (1995).

[Wie01]   A. Wiese. *Charakterisierung von Peptid-/Protein-induzierten Permeabilitätsänderungen mit rekonstituierten bakteriellen Membranen.* Habilitationsschrift, Forschungszentrum Borstel (2001).

[Wil89]   A.J. Wilson, editor. *Foams: Physics, Chemistry and Structure.* Springer Series in Apllied Biology (1989).

[WMM$^+$09] E.B. Watkins, C.E. Miller, D.J. Mulder, T.L. Kuhl, and J. Majewski. Structure and orientational texture of self-organizing lipid bilayers. *Physical Review Letters* **102**, 238101 (2009).

[Wob72]   D. Wobschall. Voltage dependence of bilayer membrane capacitance. *Journal of Colloid and Interface Science* **40**, 417 (1972).

[WSN89]   M.C. Wiener, R.M. Suter, and J.F. Nagel. Structure of the fully hydrated gel phase of DPPC. *Biophysical Journal* **55**, 315 (1989).

[WT73]   S.H. White and T.E. Thompson. Capacitance, area and thickness variations in thin lipid films. *Biochimica et Biophysica Acta* **323**, 7 (1973).

[WW91]   M.C. Wiener and S.H. White. Fluid bilayer structure determination by the combined use of x-ray and neutron diffraction. *Biophysical Journal* **59**, 162 (1991).

[Zer42]   F. Zernike. Phase contrast, a new method for the microscopic observation of transparent objects. *Physica* **9**, 686 (1942).

[ZV92]   C. Zheng and G. Vanderkooi. Molecular origin of the internal dipole potential in lipid bilayers: calculation of the electrostatic potential. *Biophysical Journal* **63**, 935 (1992).

Danksagung

Ich möchte mich zu Beginn dieser Danksagung ganz herzlich bei Prof. Dr. Tim Salditt bedanken, der es mir ermöglicht hat diese Arbeit im Institut für Röntgenphysik zu verfassen. Er hat mich im Laufe meiner Promotion, und bereits in der vorausgehenden Diplomarbeit, immer wieder mit sehr viel Enthusiasmus an die Fragestellungen in der Biophysik und insbesondere die der Biomembranforschung herangeführt. Ich danke ihm für die Zeit, die er sich für die zahlreichen Diskussionen und gemeinsamen Überlegungen genommen hat, und dafür, dass seine Tür immer offen war. Ich weiß, das große Vertrauen, das mir entgegengebracht wurde, sehr zu schätzen. Die damit verbundene Freiheit in der Gestaltung meiner Arbeit hat mir eine unschätzbar wertvolle, experimentelle Weiterbildung, insbesondere im Bereich der biophysikalischen Analysemethoden, ermöglicht. Ich bedanke mich darüberhinaus für die Finanzierung in den drei Jahren zunächst im Rahmen des SFB 755 und schließlich des SFB 803. Ich hoffe, dass wir auch nach meiner Promotion noch die ein oder andere Synchrotronmesszeit, die ich in Zukunft sicher sehr vermissen werde, zusammen erleben werden.

Ich möchte mich weiterhin ganz herzlich bei Prof. Dr. Claudia Steinem bedanken, die, wie schon bei meiner Diplomarbeit, sich bereit erklärt hat das Koreferat für die Arbeit zu übernehmen. Desweiteren danke ich ihr für die anregenden Diskussionen und Ratschläge während der Prüfungskommitteesitzungen. Ich habe mich sehr gefreut so viele neue Ideen zu Präparation- und Untersuchungsmethoden von freistehenden Lipidmembranen aus den Gesprächen mit ihr und ihren Mitarbeitern mitnehmen zu können.

Ich freue mich und danke Prof. Dr. Helmut Grubmüller dafür, dass ich ihn als drittes Mitglied mit in die Prüfungskommission aufnehmen durfte. Die ausgiebigen und intensiven Gespräche über meine Arbeit während der einzelnen Treffen haben mir neue Denkanstöße aufgezeigt und mir so manche neue Sicht der Dinge verschafft.

Desweiteren möchte ich mich bei Prof. Dr. Sarah Köster, Prof. Dr. Dr. Detlev Schild und Prof. Dr. Thomas Pfohl bedanken, die sich bereit erklärt haben an der Verteidigung im Rahmen meiner Promotion teilzunehmen. Ein spezieller Dank gilt Prof. Dr. Sarah Köster, die sich für ihre Ratschläge und unsere Gespräche, insbesondere in der stressigen Endphase meiner Promotion, immer sehr viel Zeit genommen hat und immer eine offene Tür und ein offenes Ohr hatte.

Ich bin Michael Mell zu großem Dank verpflichtet, der mit mir während der Zeit seiner Diplomarbeit an der Phasenkontrastanalyse von BLMs zusammengearbeitet hat. Die Zusammenarbeit mit ihm hat immer sehr viel Spaß gemacht und ich bin mir sicher, dass genau das zum Erfolg und den tollen Ergebnissen unserer Arbeiten beigetragen hat. Ich wünsche ihm viel Erfolg für die Arbeit

List of publications

[1] André Beerlink, P.-J. Wilbrandt, E. Ziegler, D. Carbone, T. H. Metzger and Tim Salditt, X-ray Structure Analysis of Free-Standing Lipid Membranes Facilitated by Micromachined Apertures, *Langmuir* **24**, 4952-4958 (2008).

[2] André Beerlink, M. Mell, M. Tolkiehn and T. Salditt, Hard x-ray phase contrast imaging of black lipid membranes, *Applied Physics Letters* **95**, 203703 (2009).

[3] Philipp E. Schneggenburger, André Beerlink, Brigitte Worbs, Tim Salditt and Ulf Diederichsen, A Novel Heavy-Atom Label for Side-Specific Peptide Iodination: Synthesis, Membrane Incorporation and X-ray Reflectivity, *ChemPhysChem* **10**, 1567-1576 (2009).

[4] Klaus Giewekemeyer, P. Thibault, S. Kalbfleisch, André Beerlink, C.M. Kewish, M. Dierolf, F. Pfeiffer, and Tim Salditt, Quantitative biological imaging by ptychographic x-ray diffraction microscopy, *PNAS* **107**, 529-534 (2010).

[5] Philipp E. Schneggenburger, André Beerlink, Britta Weinhausen, Ulf Diederichsen and Tim Salditt, Peptide Model Helices in Lipid Membranes - Insertion, Positioning and Lipid Response on Aggregation Studied by X-ray Scattering Methods, *European Biophysics Journal*, **in press** (2010).

Curriculum vitae

André Beerlink
born: May, 14th 1982 in Nordhorn (Germany)
nationality: German

Course of University education	
04/2007 - 05/2010	PhD thesis at the Institut für Röntgenphysik under the supervision of Prof. Dr. Tim Salditt, Georg-August-Universität Göttingen. Title of thesis: "Black lipid membranes studied by x-ray phase contrast imaging". since 01/2009: Project staff of the Collaborative Research Centre 803: "Functionality Controlled by Organization in and between Membranes". since 04/2008: Member of the IMPRS-PBC of the Göttingen Graduate School for Neurosciences and Molecular Biosciences (GGNB). 07-09/2007: Guest researcher at the University of Missouri, Columbia, in the Group of Prof. Dr. Maikel Rheinstädter. since 07/2007: Project staff of the Collaborative Research Centre 755: "Nanoscale photonic imaging".
10/2005 - 03/2007	Diploma thesis at the Institut für Röntgenphysik under the supervision of Prof. Dr. Tim Salditt. Title of thesis: "Planare, freistehende Lipidmembranen für die Röntgenstrukturanalyse".
10/2002 - 09/2005	Studies of physics at the Georg-August-Universität Göttingen.

Membranes fulfill many different functions inside a cell and have consequently been in the focus of biophysical studies for several decades. High resolution structure analysis of model membrane systems by x-ray reflectivity is typically performed using stabilizing solid supports, which have shown to strongly interact with the membranes and can severly affect the membrane`s functionality. To circumvent these restrictions free-standing lipid model membranes, also called Black Lipid Membranes (BLMs), have been used in this work towards a novel type of structural assay based on x-ray phase contrast imaging. Bulged lipid bilayers fully immersed in buffer solution have been visualized by a transmitted plane or spherical x-ray wave front in the Fresnel regime after free space propagation. The development of the experimental system and the image analysis enables a quantitative investigation of the membrane`s structural properties in a localized membrane patch. In future this technique can be used to study the structure of membranes and more generally ultrathin films in functional and physiological environments and under out-of-equilibrium conditions.

GEORG-AUGUST-UNIVERSITÄT
GÖTTINGEN

Universitätsverlag Göttingen